

CRYOGENIC MICROWAVE ANISOTROPIC ARTIFICIAL
MATERIALS

by

FRANK TRANG

B.S., University of California - Santa Cruz, 2001

M.S., University of California - San Diego, 2004

A thesis submitted to the
Faculty of the Graduate School of the
University of Colorado in partial fulfillment
of the requirements for the degree of
Doctor of Philosophy
Department of Electrical, Computer, and Energy Engineering

2013

This thesis entitled:

Cryogenic Microwave Anisotropic Artificial Materials

written by [Frank Trang](#)

has been approved for the Department of Electrical, Computer, and Energy Engineering

[Zoya Popović](#)

[Horst Rogalla](#)

Date _____

The final copy of this thesis has been examined by the signatories, and we
Find that both the content and the form meet acceptable presentation standards
Of scholarly work in the above mentioned discipline.

Trang, Frank (Ph.D., Electrical Engineering)

Cryogenic Microwave Anisotropic Artificial Materials

Thesis directed by Professor Zoya Popović and Professor Horst Rogalla

This thesis addresses analysis and design of a cryogenic microwave anisotropic wave guiding structure that isolates an antenna from external incident fields from specific directions. The focus of this research is to design and optimize the radome's constituent material parameters for maximizing the isolation between an interior receiver antenna and an exterior transmitter without significantly disturbing the transmitter antenna far field characteristics.

The design, characterization, and optimization of high-temperature superconducting metamaterials constitutive parameters are developed in this work at X-band frequencies. A calibrated characterization method for testing arrays of split-ring resonators at cryogenic temperature inside a TE_{10} waveguide was developed and used to back-out anisotropic equivalent material parameters. The artificial material elements (YBCO split-ring resonators on MgO substrate) are optimized to improve the narrowband performance of the metamaterial radome with respect to maximizing isolation and minimizing shadowing, defined as a reduction of the transmitted power external to the radome. The optimized radome is fabricated and characterized in a parallel plate waveguide in a cryogenic environment to demonstrate the degree of isolation and shadowing resulting from its presence. At 11.12 GHz, measurements show that the HTS metamaterial radome achieved an isolation of 10.5 dB and the external power at 100 mm behind the radome is reduced by 1.9 dB. This work demonstrates the feasibility of fabricating a structure that provides good isolation between two antennas and low disturbance of the transmitter's fields.

DEDICATION

This thesis is dedicated to my wife Elizabeth and son Ian. To Elizabeth for the support and patience. To Ian for the many laughs.

ACKNOWLEDGMENTS

I have been fortunate to have met many wonderful individuals who have helped me along the way to the completion of this work.

First, I would like to thank my two advisors Professor Zoya Popović and Professor Horst Rogalla for their invaluable technical guidance and support during these past three plus years, and the opportunity to study in this exciting research area. I would also like to thank Professor Edward Kuester for the many helpful discussion on metamaterials. I also thank Ms. Jarka Hladisova for her administrative helps.

I would like to thank the United States Air Force Office of Scientific Research for the funding support under grant FA9550-10-1-0413.

There are many individuals from NIST that I would like to thank: Dr. Sam Benz has been very grateful for allowing me to use the lab space to conduct my cryogenic experiments and for helpful discussions; Dr. Paul Dresselhaus for making the contact masks; and Ms. Leila Vale for instructions on dicing the superconducting samples.

To the past and current members in the microwave research group, a sincere thank to everyone who have made the lab a very enjoyable work environment, both socially and technically: Dr. Robert Scheeler, Dr. Jonathan Chisum, Dr. Asmita Dani, Scott Schafer, Dr. Erez Falkenstein, Dr. Brad Lindseth, Dr. Michael Roberg, Jennifer Imperial, Andrew Zai, Michael Litchfield, Sean Korhummel, Ignacio Ramo, Xavier Palomer, Dr. Leonardo Ranzani, Dr. David Sardin, Dr. Tibult Reveyrand, Dr. Dan Kuester, Parisa Roodaki, and Mike Coffey.

Finally, I would like to thank my family for their support and encouragement.

CONTENTS

1	INTRODUCTION	1
1.1	Motivation	3
1.2	History	5
1.3	Metamaterial	8
1.4	Thesis Outline	12
2	CONSTITUTIVE PARAMETER TRANSFORMATIONS	16
2.1	Introduction	16
2.2	Constitutive Tensor Transformation	17
2.3	Transformation for a Cylindrical Cloak	21
2.4	Realizable Parameter Set	25
3	RESONANT RESPONSE OF HTS SRR	29
3.1	Introduction	29
3.2	HTS SRR Fabrication and Measurement Setup	30
3.3	Measurement Results	31
3.4	Temperature Dependent f_r	36
3.5	Effective Constitutive Parameter Extraction	40
3.6	Conclusion	40
4	EFFECTIVE CONSTITUTIVE PARAMETERS OF HTS SRR	43
4.1	Introduction	43
4.2	Extraction Method	45

4.3	Validation of Extraction Method	50
4.4	HTS SRR Specifications and Measurement Setup	54
4.5	Experimental Results	58
4.6	Comparison to Simulations	63
4.7	Discussion	66
5	RADOME MEASUREMENT	68
5.1	Introduction	68
5.2	Room Temperature Measurement Setup	69
5.3	Radome Measurements and Simulations	73
5.4	SRR Optimization	77
5.5	Cryogenic Measurement Setup	89
5.6	Cryogenic Measurements	91
6	CONCLUSIONS AND FUTURE WORK	98
6.1	Summary and Contributions	98
6.2	Future Work	101
6.2.1	Unusual high Q -factor Resonances	101
6.2.2	Antenna Measurements	102
6.2.3	Radome and Metamaterial Geometries	103
A	FREQUENCY RESPONSE OF DOUBLE-SIDED SRR ARRAYS TO FABRICATION TOLERANCES	104
A.1	Introduction	104
A.2	Measurements and Simulations	106
A.3	Tolerance Studies	107
A.4	Conclusion	113
B	EFFECTIVE PARAMETER EXTRACTION FROM S-PARAMETERS	114
B.1	Extraction Method For Isotropic, Homogeneous Materials	114

C	COORDINATE TRANSFORMATION BACKGROUND	118
C.1	Coordinate Transformation Background Mathematics	118
D	MATLAB CODE (SPACE TRANSFORMATIONS)	122
D.1	Matlab Code (Space Transformations)	122
	Bibliography	126

LIST OF TABLES

- 1.1 Common metamaterial shapes found in literature and their effective electromagnetic properties. NIR stands for negative index of refraction. **9**

- 5.1 Optimized copper and YBCO SRR dimensions for the radomes. The unit for dimension is mm. **80**

- A.1 Fabrication imperfections and their effects on the resonant frequency. (V–vertical offset, H–horizontal offset) **109**

- A.2 Resonant frequencies with varied groove dimensions **112**

LIST OF FIGURES

- 1.1 A superconducting receiver antenna is located inside the isolation metamaterial radome in the path of a pair of antennas and is receiving radiation in the zenith direction undisturbed by the other two antennas. The communication link between the pair of dipole antennas (left and right) is unaffected by the radome **2**
- 1.2 (a) and (b) show the direction of the Poynting vector field lines. In (a) no object is placed in its path. In (b) a cylindrical electromagnetic cloak is placed in the path of the power flow. The interior is completely isolated from the exterior. In addition, the lines are undisturbed outside of the structure. **3**
- 1.3 Electric field plot of (a) an empty parallel plate waveguide and (b) a parallel plate waveguide with a copper cylinder placed some distance away. The E-field is greatly distorted by the presence of the copper cylinder. The inset figure shows the scale. **6**
- 1.4 Relative permittivity and permeability values for a cylindrical guiding structure with inner radius $a=20$ cm and outer radius $b=40$ cm. **6**
- 1.5 Realizable values of the relative permittivity and permeability for a cylindrical cloak with inner radius $a = 22.9$ mm and outer radius $b = 34.9$ mm. **7**
- 1.6 All materials can be mapped into one of the four quadrants described by their electric permittivity and magnetic permeability. **10**
- 1.7 (a) The unit cell of the wire metamaterial has dimensions of $2.5\text{mm}\times 2.5\text{mm}\times 2.5\text{mm}$, with wire length = 2.5mm and wire width = 0.14mm . (b) The extracted effective relative permittivity where the blue and green curves represent ϵ' and ϵ'' , respectively. **11**

- 1.8 (a) The unit cell of the SRR metamaterial has dimensions of $2.5\text{mm} \times 2.5\text{mm} \times 2.5\text{mm}$, with the outer SRR width = 2.2mm , line width = 0.2mm , gap = 0.3mm , and separation between the two rings = 0.15mm . (b) The extracted effective relative permeability where the blue and green curves represent μ' and μ'' , respectively. **12**
- 1.9 (a) shows the unit cell of the SRR-wire metamaterial, where the dimensions were specified in Figures 1.7a and 1.8a. (b), (c), and (d) show the effective relative permeability, permittivity, and refractive index, respectively. The blue and green curves represent the μ' and μ'' values. **13**
- 2.1 Integration path for $\mathbf{E} \cdot d\mathbf{l}$. **19**
- 2.2 Transformation from the original space (a) to the transformed space (b), in which the space inside a volume of radius b is compressed into a cylindrical shell of inner radius a and outer radius b . **22**
- 2.3 Relative permittivity and permeability values for a cylindrical cloak with inner radius $a = 22.9\text{ mm}$ and outer radius $b = 34.9\text{ mm}$. The plot shows the values from a/a to b/a . **26**
- 2.4 Realizable values of the relative permittivity and permeability values for a cylindrical cloak with inner radius $a = 22.9\text{ mm}$ and outer radius $b = 34.9\text{ mm}$. The plot shows the values from a/a to b/a . **28**
- 3.1 A close-up photograph of the SRR unit cell with labeled dimensions, where $a=10\text{ mm}$, $b=7\text{ mm}$, $c=4.4\text{ mm}$, $d=1.5\text{ mm}$, $e=0.5\text{ mm}$, $g=1.6\text{ mm}$, $w=0.8\text{ mm}$. **30**
- 3.2 (a) A sketch of the cryostat with waveguide components. (b) A photograph of the waveguide setup that fits inside the cryostat. **32**
- 3.3 A photograph of the measurement setup, showing the flow-type cryostat on top of a liquid helium filled dewar. To the right of the dewar are the network analyzer, flow control unit, and temperature controller, shown from top down. **33**

- 3.4 Placement of the HTS SRR array inside a WR-90 waveguide. The single element is placed in the same way. See Figure 3.1 for ring dimensions. **34**
- 3.5 Measured and simulated transmission (S_{21}) coefficients of an array of seven HTS SRR placed inside a WR-90 waveguide. The measurements were taken at 77 K (solid blue) and at room temperature (dashed green). **34**
- 3.6 Measurement of the transmission resonance (S_{21}) at 85 K. **35**
- 3.7 The circled points show the measured transmission resonance at 81 K. The solid line is the Lorentzian curve fitted to the data. **36**
- 3.8 Quality factor versus temperature (K) for the measured HTS SRR inside a WR-90 waveguide. It peaks around 42000 at 87 K and saturates around 5200. **37**
- 3.9 Equivalent circuit model of the SRR, where the kinetic inductance L_K is temperature dependent. **37**
- 3.10 Resonant frequency vs temperature. The red circle line and solid blue line represent measured and fitted resonant frequency, respectively. The green solid line is the calculated kinetic inductance extracted from the fitting process. **39**
- 3.11 The extracted relative permittivity and permeability at (a) 89 K and (b) 88 K. **41**
- 4.1 (a) The slab of anisotropic material is placed inside a rectangular waveguide for characterizing the effective permittivity and permeability. (b)-(d) The orientations (I, II, III, and IV, respectively) of how the material is inserted into the waveguide. **46**
- 4.2 The material under test (MUT) placed inside a rectangular waveguide with (a) orientation I and (b) orientation II, for retrieval of μ_1 , μ_3 , and ϵ_2 . **46**
- 4.3 The material under test placed inside a rectangular waveguide with (a) orientation III and (b) orientation IV, for the retrieval of ϵ_1 , ϵ_3 , and μ_2 . **49**

- 4.4 The retrieved effective material parameters, from the simulated S parameters, for the homogeneous slab with properties defined by Equations (4.27) and (4.28). The solid and dashed blue lines represent the real (') and imaginary (") parts, respectively, of the analytical values for (a) ϵ_2 , (b) μ_1 , and (c) μ_3 . The red 'O' and 'X' symbols represent the extracted values from the waveguide simulations. **51**
- 4.5 Photograph of a copper SRR on Rogers 3010 substrate with $a=2.5$ mm, $b=1.9$ mm, $c=0.2$ mm, $d=0.65$ mm, and $e=0.2$ mm. **51**
- 4.6 SRR arrays placed inside a WR-90 rectangular waveguide with orientation (a) I and (b) II. **52**
- 4.7 Extracted effective parameters for the copper on Rogers 3010 SRR arrays. The red, blue, and green curves represent results from waveguide simulations, free space simulations, and waveguide measurements, respectively. The solid and dashed curves represent the real (') and imaginary (") parts of the parameters. **52**
- 4.8 Free space models of the SRR for orientations (a) I and (b) II. The period a is 2.5 mm **53**
- 4.9 Fabricated SRR on a Rogers 3010 substrate aligned inside a WR-90 waveguide with orientations (a) I and (b) II for measurements. Refer to Figure 4.6 for a clearer image of orientation I placement. **54**
- 4.10 Simulated and measured magnitude of the transmission and reflection coefficients of the copper SRR arrays. The red and blue curves are the S_{11} and S_{21} , respectively. (a) and (b) are the simulations for orientations I and II, respectively. (c) and (d) are the measurements for orientations I and II, respectively. **55**
- 4.11 Sketch of an experimental X-band YBCO SRR array deposited on a MgO substrate with $a=2.5$ mm, $b=2$ mm, $c=0.2$ mm, $d=0.2$ mm, and $t=0.5$ mm. The material axes 1, 2, and 3 correspond with the tensor elements $\bar{\bar{\epsilon}}$ and $\bar{\bar{\mu}}$. **56**
- 4.12 50×50 mm² YBCO on MgO wafer layout of the 4×1 and 4×9 SRR arrays. $25 \mu\text{m}$ wide dicing markers were included to assist with the dicing process. **57**

- 4.13 Measurement setup showing the calibrated reference planes (CRPs) and the material under test (MUT) reference planes (MRPs). The portion inside the hashed box is cooled to ≈ 76 K. The arrows indicate the locations for the calibration and material reference planes. **57**
- 4.14 The phase of S_{21} of the TRL LINE standard: the dotted blue curve for the case where no vacuum grease was used; the dashed green curve for the case where vacuum grease was used; and the solid red curve for the case of indirect cooling. **58**
- 4.15 The effective relative permeability μ_3 extracted from poor calibrations and measurements, caused by liquid nitrogen seeping into the waveguide components. The solid red and dashed blue curves represent the real ($'$) and imaginary ($''$) parts, respectively. In (a), the waveguide parts with SRR were submerged directly into a bath of LN_2 . In (b), vacuum grease was applied to the seams of the waveguide connections. **59**
- 4.16 Photographs of diced 4×1 and 4×9 YBCO SRR arrays on MgO substrate aligned inside a WR-90 waveguide with orientations (a) I and (b) II, respectively, for measurements. The gray bars in (a) are included to clearly mark the locations of the 4×1 strips. The material axes corresponding to the Cartesian axes are shown for orientations (c) I and (d) II. **60**
- 4.17 Measured reflection (S_{11} , blue curve) and transmission (S_{21} , red curve) coefficient magnitudes of (a) the nine 4×1 SRR strips and (b) 4×9 SRR array, respectively, placed inside the waveguide section with the whole structure cooled to ≈ 76 K. The markers in (b) indicate the locations of the sharp resonances. **61**
- 4.18 Effective parameters extracted from waveguide measurements of the two oriented samples, with (a) zoomed in μ_1 , (b) μ_3 , (c) $\epsilon_{2(\text{I})}$, and (d) $\epsilon_{2(\text{II})}$. The blue and red curves are measurements and waveguide simulations, respectively. The solid and dashed curves represent the real ($'$) and imaginary ($''$) parts, respectively. The inset plot in (a) shows the full μ_1 from the measurement. **62**

- 4.19 Effective permeability (μ_1) extracted from room temperature measurement of the copper SRR arrays on a Rogers 3010 substrate, plotted on the same scale as Figure 4.18a for comparison. The solid and dashed blue curves represent the real (') and imaginary (") parts, respectively. The same measurement and calibration approach was used as in the cryogenic case. **63**
- 4.20 Reflection (S_{11} , blue curve) and transmission (S_{21} , red curve) coefficients of the (a) 4×1 and (b) 4×9 SRR array sample from full-wave waveguide simulations. The markers indicate the locations of the sharp Fano-like resonances. **64**
- 4.21 Effective parameters extracted from the free space and waveguide simulations of the two SRR arrays, with (a) μ_1 and (c) $\epsilon_{2(I)}$ from orientation I, and (b) μ_3 and (d) $\epsilon_{2(II)}$ from orientation II. The red and blue curves represent the waveguide and free space solutions, respectively. The solid and dashed curves are the real (') and imaginary (") parts, respectively. **65**
- 5.1 Cross section sketch of the parallel plate waveguide for characterizing the metamaterial radome. The FR-4 copper cladding thickness is $35 \mu\text{m}$, respectively. LS-24 absorber wedges were placed along the boundaries of the parallel plate waveguide to minimize reflection and provide a constant spacing between the two plates. **69**
- 5.2 Complex relative permittivity versus frequency of a material modeled in HFSS of the LS-24 absorber. The solid blue and dashed red curves are the real (') and imaginary (") parts, respectively. **70**
- 5.3 The shapes and orientations for the (a) horizontally tapered absorber and (b) vertically tapered absorber. The size of the parallel plate waveguide is $400 \times 400 \text{ mm}^2$. The height of the waveguide is 10 mm. **71**
- 5.4 Simulated S_{21} for an empty PPW with different absorber shapes and orientations. The two coaxial probes spaced 200 mm apart, for (a) no absorber, (b) flat absorber, (c) horizontal taper absorber, and (d) vertical taper absorber. **72**

- 5.5 Simulated S_{21} results of an empty PPW where the waveguide boundaries are terminated by perfectly matched layers (blue curve) and vertically tapered absorber wedges (red curve). The two curves are within 1 dB in the frequency band. **72**
- 5.6 (a) Sketch of the coaxial probes inserted into the parallel plate waveguide, showing the Line-Reflect-Line calibration planes. (b) A photograph of the coaxial probe used in the measurements. **73**
- 5.7 Measurement of an empty $300 \times 240 \text{ mm}^2$ PPW, described in Figure 5.1, with the two probes distanced 153 mm apart. **73**
- 5.8 (a) Photograph of the single layer radome made of 18 copper SRR arrays. (b) The radius corresponding to Equation (5.1). The radius r for this radome is 7.29 mm **74**
- 5.9 A photograph showing the relative placements of the coaxial probes during a measurement. This $300 \times 230 \text{ mm}^2$ parallel plate waveguide size is convenience for initial testings and validations with the simulations. **75**
- 5.10 Measured transmission coefficient with the receiver probe placed at the center of the radome from Figure 5.8. The measurement setup is shown in Figure 5.9. The solid blue and dashed red curves are measurements with and without the radome, respectively. **76**
- 5.11 Measured transmission coefficient with the receiver probe placed 70 mm behind the radome from Figure 5.8. The measurement setup is shown in Figure 5.9. The solid blue and dashed red curves are measurements with and without the radome, respectively. **76**
- 5.12 Three layer radome with uniform SRR dimensions in all the layers. **77**
- 5.13 Measured transmission coefficient with the receiver probe placed at the center (red curve) and 70 mm behind the three layer radome (blue curve) from Figure 5.12. The measurement setup is shown in Figure 5.9. The black and green curves are the respective measurements of an empty $300 \times 240 \text{ mm}^2$ PPW. **78**

- 5.14 Simulated transmission coefficient with the receiver probe placed at the center (red curve) and 70 mm behind the three layer radome (blue curve) from Figure 5.12. The measurement setup is shown in Figure 5.9. The black and green curves are the respective simulation of an empty $300 \times 240 \text{ mm}^2$ PPW. **78**
- 5.15 Measured transmission coefficient with the receiver probe placed at the center (red curve) and 100 mm behind the three layer radome (blue curve) from Figure 5.12. The measurement setup is similar to that in Figure 5.9. The black and green curves are the respective measurements of an empty $600 \times 600 \text{ mm}^2$ PPW. **79**
- 5.16 Each layer of the radome is made of SRR structures like the one shown here. Different layer have different SRR dimensions. In the optimization, the leg and gap of the SRR for each layer are optimized in the simulation. **79**
- 5.17 The relative positions (top view) of the probes and radome inside a 10 mm tall parallel plate waveguide for the optimization process. The goal is maximizing the difference in S_{21} and minimizing the difference in S_{31} with respect to the empty waveguide simulations. **80**
- 5.18 Simulated results of the optimized copper SRR radome placed inside a $300 \times 240 \text{ mm}^2$ PPW. The SRR dimensions are given in the Copper columns of Table 5.1. The dashed red and blue curves are the S_{21} and S_{31} for the empty PPW simulation, respectively. The solid red and blue curves are the S_{21} and S_{31} for the empty radome simulation, respectively. **81**
- 5.19 Simulated results of the optimized copper SRR radome placed inside a $400 \times 400 \text{ mm}^2$ PPW. The SRR dimensions are given in the Copper columns of Table 5.1. The dashed red and blue curves are the S_{21} and S_{31} for the empty PPW simulation, respectively. The solid red and blue curves are the S_{21} and S_{31} for the empty radome simulation, respectively. **81**
- 5.20 Simulated results of the optimized YBCO SRR radome placed inside a $400 \times 400 \text{ mm}^2$ PPW. The SRR dimensions are given in the YBCO column of Table 5.1. The dashed red and blue curves are the S_{21} and S_{31} for the empty PPW simulation, respectively. The solid red and blue curves are the S_{21} and S_{31} for the empty radome simulation, respectively. **82**

- 5.21 The setup for calculating the delivered power in the path between the exciting and receiving probes. The power density is integrated over each rectangle to determine the time-averaged power. **82**
- 5.22 The transmitted power at 10.8 GHz (red curve) along the line of sight from the transmitter ($x = 100$ mm) to the receiver ($x = -100$ mm) with the copper SRR radome centered at $x = 0$ mm. The blue curve is the case of an empty PPW characterization. The bar shows the radome cross section. **84**
- 5.23 The transmitted power at 10.9 GHz (red curve) along the line of sight from the transmitter ($x = 100$ mm) to the receiver ($x = -100$ mm) with the copper SRR radome centered at $x = 0$ mm. The blue curve is the case of an empty PPW characterization. The bar shows the radome cross section. **84**
- 5.24 The transmitted power at 11 GHz (red curve) along the line of sight from the transmitter ($x = 100$ mm) to the receiver ($x = -100$ mm) with the copper SRR radome centered at $x = 0$ mm. The blue curve is the case of an empty PPW characterization. The bar shows the radome cross section. **85**
- 5.25 The transmitted power at 10.8 GHz (red curve) along the line of sight from the transmitter ($x = 100$ mm) to the receiver ($x = -100$ mm) with the copper cylindrical shell centered at $x = 0$ mm. The blue curve is the case of an empty PPW characterization. **85**
- 5.26 The transmitted power at 10.8 GHz (red curve) along the line of sight from the transmitter ($x = 100$ mm) to the receiver ($x = -100$ mm) with the HTS SRR radome centered at $x = 0$ mm. The blue curve is the case of an empty PPW characterization. The bar shows the radome cross section. **86**
- 5.27 The transmitted power at 10.9 GHz (red curve) along the line of sight from the transmitter ($x = 100$ mm) to the receiver ($x = -100$ mm) with the HTS SRR radome centered at $x = 0$ mm. The blue curve is the case of an empty PPW characterization. The bar shows the radome cross section. **86**

- 5.28 The transmitted power at 11 GHz (red curve) along the line of sight from the transmitter ($x = 100$ mm) to the receiver ($x = -100$ mm) with the HTS SRR radome centered at $x = 0$ mm. The blue curve is the case of an empty PPW characterization. The bar shows the radome cross section. **87**
- 5.29 A comparison in performance between the copper and YBCO SRR radome at 11 GHz. The YBCO radome has ≈ 2 dB better in regards to the reduction of power versus the copper SRR radome. **87**
- 5.30 Magnitude of the Poynting vector in the parallel plate waveguide for (a) an empty PPW, at 11 GHz (b) a copper cylindrical shell at 10.8 GHz, (c) a copper SRR radome at 11 GHz, and (d) a YBCO SRR radome at 11 GHz. The color scale shows the magnitude level between 1 W/m^2 (blue) to 500 W/m^2 (red). **88**
- 5.31 Cross section sketch of the cryogenic measurement setup. The parallel plate is enclosed inside a steel box and is cooled by a SunPower Cryotel GT cryocooler from the base of the box. **90**
- 5.32 Cryogenic setup photographs of (a) the full setup, (b) the setup without the top FR-4 sheet, (c) the setup with the full PPW, and (d) the setup with the enclosing stainless steel lid. **92**
- 5.33 The fabricated three layer YBCO SRR on MgO radome with the optimized SRR dimensions. **93**
- 5.34 Room and cold temperature measurements of a $400 \times 400 \text{ mm}^2$ parallel plate waveguide without the radome. The black and green curves are the room temperature measurements with the transmitter and receiver probes spaced 100 mm and 200 mm apart, respectively. The red and blue curves are the corresponding cold measurements. **94**
- 5.35 Room temperature transmission measurements of the YBCO SRR radome. The red and blue curves are the cases when the receiver probe is placed at the center of and 100 mm behind the radome, respectively. **94**

- 5.36 Cold temperature measurements of the YBCO SRR radome for isolation (receiver probe placed at the radome center). The dashed red curve shows the empty PPW measurement. **95**
- 5.37 Cold temperature measurements of the YBCO SRR radome for shadowing (receiver probe placed 100 mm behind the radome). The dashed red curve shows the empty PPW measurement. **95**
- 5.38 Cold temperature measurements of the YBCO SRR radome for isolation (receiver probe placed at the radome center). The dashed red curve shows the empty PPW measurement. **96**
- 5.39 Cold temperature measurements of the YBCO SRR radome for shadowing (receiver probe placed 100 mm behind the radome). The dashed red curve shows the empty PPW measurement. **96**
- 5.40 Cold temperature measurements of the YBCO SRR radome for characterizing the (a) isolation and (b) shadowing. The red and blue curves are for the empty and radome cases. **97**
- 6.1 Quality factor versus temperature (K) for the measured HTS SRR inside a WR-90 waveguide. It peaks around 42000 at 87 K and saturates around 5200. **101**
- 6.2 Measured reflection (S_{11} , blue curve) and transmission (S_{21} , red curve) coefficient magnitudes of the 4×9 SRR array, respectively, placed inside the waveguide section with the whole structure cooled to ≈ 76 K. The markers in (b) indicate the locations of the sharp resonances. **102**
- 6.3 An open-top radome measurement setup for characterizing the performance of the radome for communication applications. The pair of monopole antennas and patch antennas can ideally communicate with their respective party without interference from the other pair. **103**
- A.1 A DSRR array inside a WR-90 waveguide section. **105**

- A.2 Photo of unit cell with labeled dimensions. **106**
- A.3 Side view of a unit cell (not drawn to scale). **107**
- A.4 Simulated and measured reflection (a) and transmission (b) coefficient magnitudes of the DSRR1 array inside the waveguide. The solid blue and dashed red curves are from the simulations and measurements, respectively. **108**
- A.5 Measured transmission coefficients for DSRR1–DSRR5 (with minima ordered left to right). **108**
- A.6 Microstrip lines for measuring the relative permittivity of the substrate. **110**
- A.7 Microscope photographs showing the width ($w \approx 254 \mu\text{m}$) and depth ($g \approx 105 \mu\text{m}$) of a groove from the top (a) and side (b). The sketch in (c) shows a cross-section with relevant dimensions (not to scale). **111**
- A.8 The measured transmission (dashed blue) and reflection (dashed red) coefficients shown together with the simulation (solid lines) for DSRR1, which includes identical grooves on both sides with a groove width $w=254 \mu\text{m}$ and depth $g=107 \mu\text{m}$. The ring dimensions are as specified in section **A.1** with $a=5.08 \text{ mm}$, $b=5.715 \text{ mm}$, $c=4 \text{ mm}$, $d=1.4 \text{ mm}$, $r=0.8 \text{ mm}$, $s=0.5 \text{ mm}$. **112**
- A.9 Simulated reflection (a) and transmission (b) coefficient magnitudes of a single-sided SRR array with (dashed red) and without (solid blue) the grooves adjacent to the copper traces inside the waveguide. **113**
- B.1 Transmission line model of an isotropic, homogeneous slab of dielectric. **115**
- C.1 (a) Transformed Cartesian (b) Original curvilinear **119**

CHAPTER 1

INTRODUCTION

CONTENTS

1.1	Motivation	3
1.2	History	5
1.3	Metamaterial	8
1.4	Thesis Outline	12

This thesis presents a microwave cryogenic wave guiding structure that provides isolation between an interior receiver and an exterior transmitter without significantly distorting the transmitter antenna far field pattern. A sketch illustrating the problem and approach is shown in Figure 1.1. An arbitrarily-polarized transmitting antenna polarized is able to communicate with an intended receiver some distance away from the isolation structure, minimally affected by its presence. In the figure, the antenna at the center is shown as cross-polarized with respect to the transmitting antenna, which means there is already isolation between the two. However, some power could be coupled into the center antenna. In our measurements and simulations, these two antennas are co-polarized to simulate the worst case. We will show that isolation can be achieved even in the co-polarized scenario. Small antennas can be made in superconducting technology for improved gain and low noise amplifiers can be cooled for improving the noise figure. This means that the wave guiding radome can also be implemented in superconducting technology, resulting in low loss. It will be shown that a radome that meets the operating requirements has electromagnetic properties that are not found in

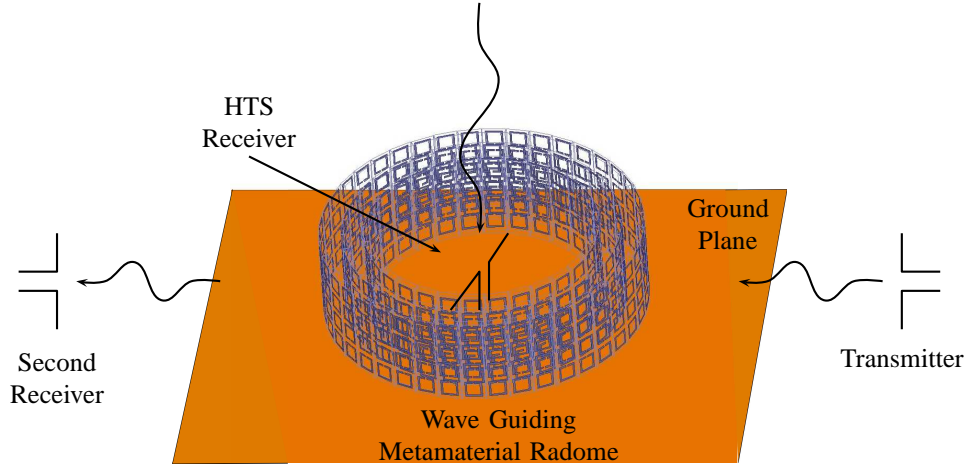


Figure 1.1: A superconducting receiver antenna is located inside the isolation metamaterial radome in the path of a pair of antennas and is receiving radiation in the zenith direction undisturbed by the other two antennas. The communication link between the pair of dipole antennas (left and right) is unaffected by the radome

natural materials. Thus, it will be constructed of metamaterial elements, such as split-ring resonators. The structure is multi-layered and cylindrical in shape, with each layer constructed from arrays of high-temperature superconducting split-ring resonator metamaterials, artificial materials that have properties that are not found in regular materials. To understand the functionality of the structure, imagine a plane wave propagating in free space with no object in its path, Figure 1.2a, where the gray region shows the placement location of the structure. The straight arrows show the direction of the Poynting vector field lines. When the isolation radome is placed in the path of propagation (gray region in Figure 1.2b), the structure isolates its interior from the outside fields, while outside of the radome the fields are not altered. Such structures have been demonstrated in simulations [1–3] and similar “metamaterial cloaking” structures have been constructed and measured using normal conducting resonant elements [4, 5]. The structure in [4] has properties such that the permeability is radially varying and is measured inside a parallel plate waveguide. The structure in [5] has a radially varying permittivity and is measured in free space (anechoic chamber). In both cases, the amount of isolation in the interior of the cloak and field distortion exterior to the cloak are not quantified. Thus, one can only visually judge the performance of the cloaking ability of the structure. In this thesis, a probe measures the received power of the measurement environment with and without the wave guiding radome. This gives us the information to quantify the isolation and shadowing characteristics of the structure. Shadowing is defined

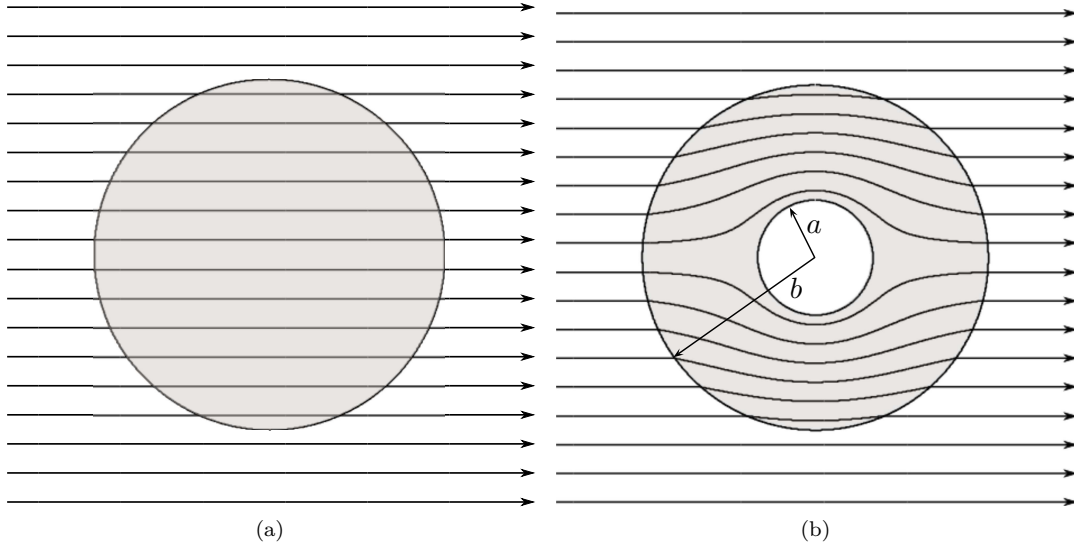


Figure 1.2: (a) and (b) show the direction of the Poynting vector field lines. In (a) no object is placed in its path. In (b) a cylindrical electromagnetic cloak is placed in the path of the power flow. The interior is completely isolated from the exterior. In addition, the lines are undisturbed outside of the structure.

as a reduction of external transmitted power in the presence of the radome with respect to the no-radome case. Using a cylindrical shape has the advantage that it can be opened on the ends to allow an antenna to be placed in its interior to receive and transmit radiation in the perpendicular direction. For our work, only the guiding structure has to operate at the same frequency as the transmitter. The receiver can operate at any frequency. The rest of this introductory chapter will present motivation for the work, a brief history of electromagnetic cloaks, a discussion of metamaterials and how they are relevant to this research, and finally an outline of the thesis.

1.1 MOTIVATION

For small antennas, the loss resistance, R_L , in the conductor and substrate can dominate the radiation impedance, since the real resistance R_r is small. The radiation efficiency given by

$$\eta = \frac{R_r}{R_r + R_L} \quad (1.1)$$

will therefore be small. To demonstrate the impact loss has on the radiation efficiency, consider an electrically small single copper loop antenna, with diameter $d=10$ mm and wire radius $b=0.5$ mm. Generally, an antenna

is considered electrically small if its largest dimension is less than or equal to one-tenth of the operating wavelength ($\leq \lambda/10$). For example, the largest dimensions for a dipole, a loop, and a microstrip patch antenna are the length, diameter, and diagonal, respectively [6]. The radiation resistance R_r and loss resistance R_L for a loop antenna at 1 GHz are given by [7]

$$R_r = 20\pi^2 \left(\frac{\pi d}{\lambda} \right)^4 = 0.0237 \Omega \quad (1.2)$$

$$R_L = \frac{l}{P} R_S = \frac{\pi d}{2\pi b} \sqrt{\frac{\omega\mu_0}{2\sigma}} = 0.0825 \Omega \quad (1.3)$$

The term R_L represents the loss resistance due to the conductor and dielectric loss, which is almost four times greater than R_r . The antenna radiation efficiency for this antenna is 22.3%. However, if the normal conducting part is replaced with superconductor, e.g. yttrium barium copper oxide (YBCO) with surface resistance (R_S)= 500 $\mu\Omega$, [8] the loss resistance can be brought down due to the much lower surface resistance of the superconductor relative to the normal conductor. Chalupka *et al.* [9] experimentally demonstrated a large increase in radiation efficiency by comparing a miniature copper patch antenna (6 mm by 6 mm on a 1 mm thick substrate) to a high-temperature superconducting (HTS) YBCO version at 2.45 GHz. At 77 K the measured efficiency was 3% for the copper patch and 45% for the YBCO patch. The increase in radiation efficiency from copper to HTS antennas has also been reported in [10] and [11].

A disadvantage of superconducting antennas is the need to cool them. In 1986, Bednorz and Müller discovered that lanthanum barium copper oxide (LBCO) has a critical temperature (T_C) in the 30 K range [12]. In 1987, Wu *et al.* [13] discovered the high-temperature superconductor (HTS) YBCO that has a $T_C \approx 92$ K, which is the first superconductor to have a T_C greater than the boiling temperature of liquid nitrogen. Thus antennas made of high- T_C superconductors can easily be cooled to below T_C with liquid nitrogen (LN₂) (with a boiling temperature ≈ 77 K) or small cryocoolers, e.g. those from SunPower, Inc. [14] Another problem superconducting antennas face is nonlinearity when a strong microwave field creates a surface current density that is comparable to the superconductor critical current density (J_C) (≈ 2 MA/cm² at 77 K). Using the HTS antenna as a transmitter, Chalupka [9] measured a drop in $|S_{21}|/|S_{21}^{\max}|$, from unity at -20 dBm input power into the feed to ≈ 0.4 at 0 dBm input power. Such an antenna would be rendered unusable as a receiver in the presence of a strong transmitter.

One method for isolating the receiver from a transmitter is by shielding them with a copper cylinder. The isolation in this case will be nearly perfect. However, this will greatly alter the transmitter’s field characteristics. Figure 1.3a shows a snapshot in time of the electric field inside an empty parallel plate waveguide at 9.5 GHz. The field plots are generated in the Ansys HFSS full-wave simulation where the source is a waveport excitation (center bottom). The four sides of the waveguide are assigned radiation boundaries to reduce reflection. To illustrate the field distortion in the presence of the copper cylinder, a 1 mm thick cylindrical copper shell is placed in the radiation path, Figure 1.3b. The electric field amplitude is greatly reduced behind the copper shell, in addition to reflection on the transmitter side. An improved approach is to utilize a structure constructed of artificial materials to help guide the EM waves around the receiver. This is discussed in the next section, with the derivation of the material properties presented in Chapter 2.

1.2 HISTORY

A popular method for deriving the electromagnetic properties of the radome medium that redirect the Poynting vector field lines, as defined by Figure 1.2b, is a coordinate transformation method presented by Ward, *et al.* [15]. Similar methods are also presented in [2, 16, 17] and Chapter 2, from which one can derive the inhomogeneous and anisotropic electric permittivity and magnetic permeability for a structure that guides the electromagnetic waves around itself. The presence of the structure does not alter the transmitter’s far field pattern exterior to the structure. Thus, this structure is sometimes referred to as an electromagnetic or metamaterial cloak [1, 3, 4]. The ideal permittivity and permeability tensors for a cylindrical and spherical cloak as given by [2, 4] are

$$\frac{\boldsymbol{\mu}}{\mu_0} = \frac{\boldsymbol{\epsilon}}{\epsilon_0} = \text{diag} \left[\frac{r-a}{r}, \frac{r}{r-a}, \left(\frac{b}{b-a} \right)^2 \frac{r-a}{r} \right] \quad (\text{Cylindrical}) \quad (1.4)$$

$$\frac{\boldsymbol{\mu}}{\mu_0} = \frac{\boldsymbol{\epsilon}}{\epsilon_0} = \text{diag} \left[\frac{b}{b-a} \left(\frac{r-a}{r} \right)^2, \frac{b}{b-a}, \frac{b}{b-a} \right] \quad (\text{Spherical}) \quad (1.5)$$

where each structure is hollow in the interior with an inner radius a and outer radius b , as shown in Figure 1.2b. The variable r is the radial distance from the center. The formula for the cylindrical geometry (Equation (1.4)) is derived in Chapter 2. As an example, a plot of the permittivity and permeability values are shown in

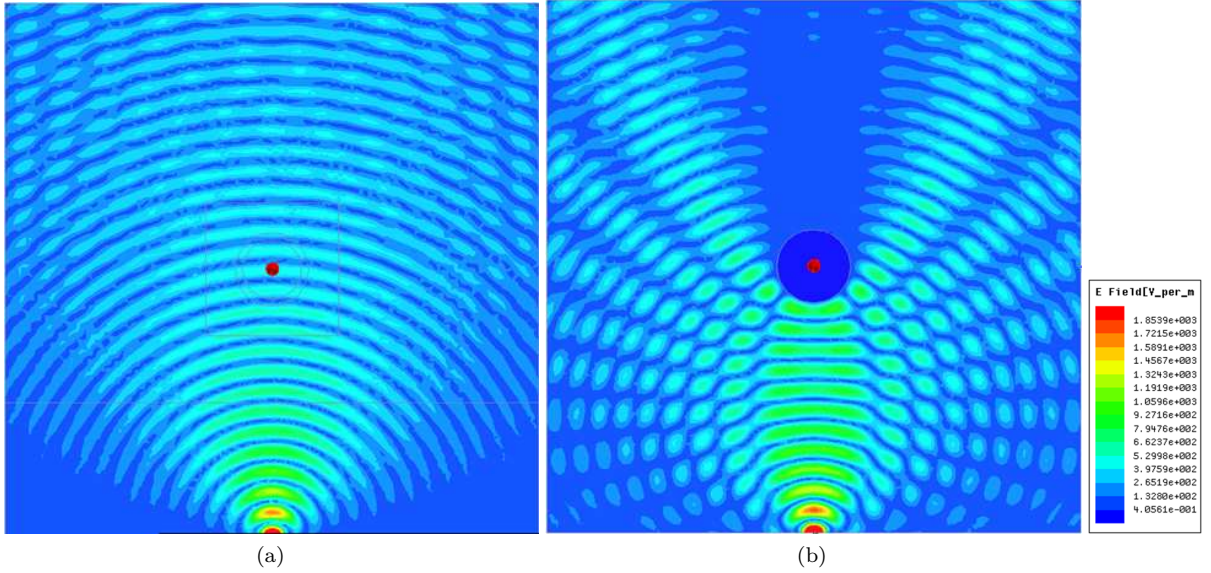


Figure 1.3: Electric field plot of (a) an empty parallel plate waveguide and (b) a parallel plate waveguide with a copper cylinder placed some distance away. The E-field is greatly distorted by the presence of the copper cylinder. The inset figure shows the scale.

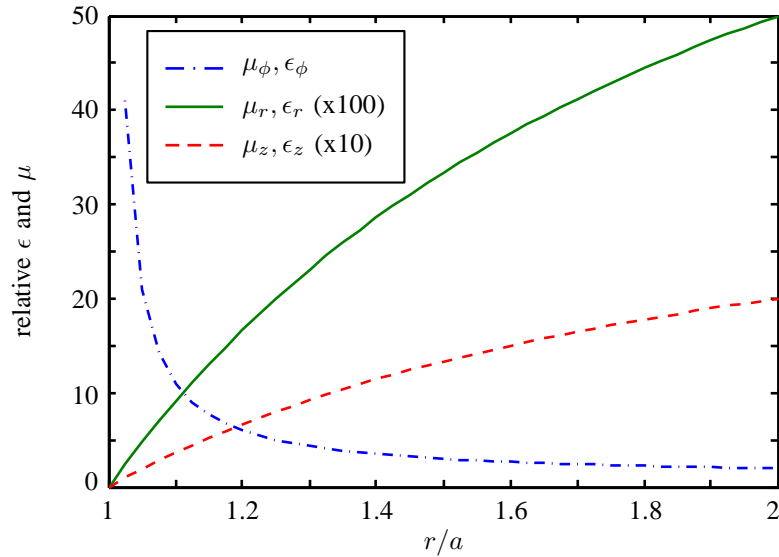


Figure 1.4: Relative permittivity and permeability values for a cylindrical guiding structure with inner radius $a=20$ cm and outer radius $b=40$ cm.

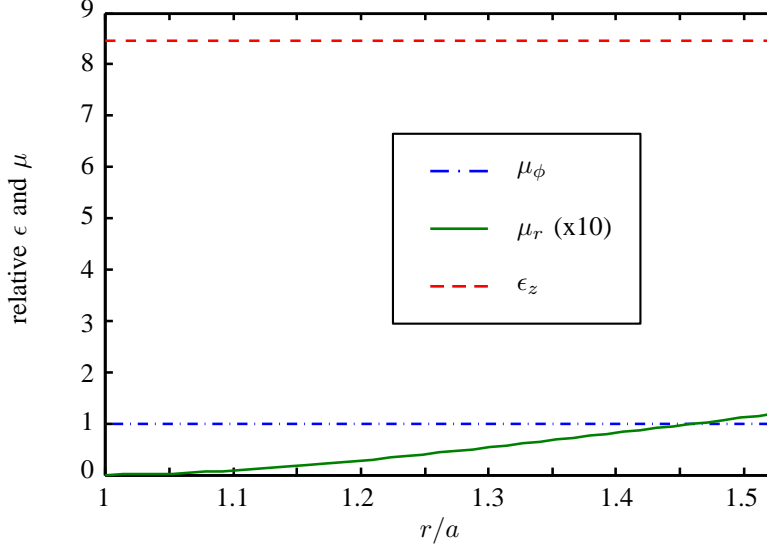


Figure 1.5: Realizable values of the relative permittivity and permeability for a cylindrical cloak with inner radius $a = 22.9$ mm and outer radius $b = 34.9$ mm.

Figure 1.4, which illustrates the inhomogeneity and anisotropy of the material. With knowledge of the testing environment, the number of relevant parameters may be reduced, e.g. only ϵ_z , μ_r , and μ_ϕ are needed when measuring inside a parallel plate waveguide, as discussed in Chapter 2. In addition, with a trade-off of a non-zero reflection, the number of spatial varying terms can be reduced to one, with

$$\epsilon_z = \left(\frac{b}{b-a} \right)^2 = \text{Constant}, \quad \mu_r = \frac{r-a}{a}, \quad \mu_\phi = 1 \quad (1.6)$$

Figure 1.5 shows the values for $a=22.9$ mm and $b=34.9$ mm.

Cummer *et al* [1] in 2006 were the first to demonstrate in simulations that a cloaking structure with the electromagnetic properties specified in Equation (1.4) can indeed isolate the inner region from the external fields without perturbing the fields. The material properties are plotted in Figure 1.4. In Equation (1.4), we notice that loss are not included in the derived permittivity and permeability tensors. In his paper, Cummer also showed that the performance will degrade if the cloak is lossy. The cloak can be realized with artificial materials composed of conducting resonant elements printed on microwave substrates [4]. The conductor loss can be reduced by using a superconductor and at the low operating temperature of superconductors, the loss in the substrate is also reduced.

1.3 METAMATERIAL

The metamaterial radome has very specific frequency dependent electromagnetic properties that are not found in homogeneous natural materials. Metamaterials, as defined by Ramakrishna and Grzegorzcyk [18], are “composite materials consisting of structural units much smaller than the wavelength of the incident radiation and displaying properties not found in natural materials.” In the limit when the dimension of the structural unit is $< \lambda/10$ of the incident radiation, the composite material can be treated as having effective homogeneous material parameters [19]. All materials can be mapped into one of the four quadrants described by their electric permittivity, $\epsilon = \epsilon' - j\epsilon''$, and magnetic permeability, $\mu = \mu' - j\mu''$, shown in Figure 1.6. Materials in quadrant I have both positive permittivity and permeability, which include most dielectrics. Quadrant II are materials such as metals that exhibit a negative permittivity below the plasma frequency [20]. Quadrant IV are materials with a negative permeability, such as Ni-Zn ferrite [21]. Materials in quadrant III have simultaneous negative permittivity and permeability, a property that is not found in natural materials. Examples of metamaterials are engineered materials having a negative permittivity, negative permeability, and/or negative refractive index within a frequency band. There are many proposed designs for metamaterials. Table 1.1 presents a few of the popular shapes and their effective electromagnetic properties. The fishnet, omega, and S-shaped metamaterials have been experimentally shown to exhibit a negative index [22–24]. The wire and concentric SRR structures are studied in the simulations and presented later in this section. A single ring SRR structure is studied in both the simulations and measurements, and is presented in Chapter 4.

There have been several proposed methods for characterizing the effective constitutive parameters of composite materials such as wire and split-ring resonator arrays, with a purpose of demonstrating the existence of an effective negative permittivity and permeability over some frequency band. For example, in [19, 26–29], the plane wave normal incidence approach was discussed for retrieving the effective parameters; [30] presented an optimization technique; and in [31] a waveguide approach for retrieving the anisotropic parameters was presented. With the exception of [30], these methods involve retrieving the effective parameters from the measured or simulated scattering parameters. Appendix B presents the retrieval method for a homogeneous, isotropic medium. In Chapter 4, the analysis of the waveguide retrieval method for a homogeneous, anisotropic medium is presented in detail.


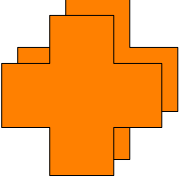


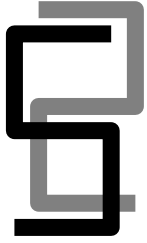
Metamaterial Designs	$\epsilon < 0$	$\mu < 0$	NIR	References
 Wire	✓			[20]
 Fishnet	✓	✓	✓	[22]
 Split-Ring Resonator	✓	✓		[25]
 Omega	✓	✓	✓	[23]
 S-shaped	✓	✓	✓	[24]

Table 1.1: Common metamaterial shapes found in literature and their effective electromagnetic properties. NIR stands for negative index of refraction.

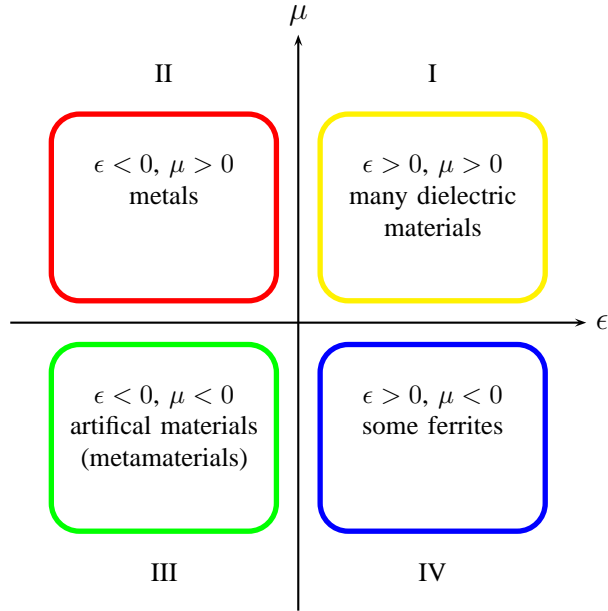


Figure 1.6: All materials can be mapped into one of the four quadrants described by their electric permittivity and magnetic permeability.

The plane wave normal incidence approach generally involves measurements of the metamaterial sample placed in the far field of two antennas. This method requires a large sample to avoid diffraction. The volume needed for such a measurement makes cooling an impractical task and thus it is not suitable for measuring samples made of superconductors. On the other hand, the waveguide approach is confined to a small volume, which makes cooling of our high-temperature superconducting metamaterial a much simpler task. Cooling of the samples with liquid helium and liquid nitrogen are demonstrated in Chapters 3 to 5.

In 1996, Pendry *et al.* [20] showed that an artificial material made of an infinite array of wires has a negative real permittivity over some frequency bandwidth. In Figure 1.7a, an HFSS simulation of a plane wave incident on an array of copper strip unit cells is shown, where the electric field is parallel to the copper trace. The electric and magnetic walls define the directions of the electric and magnetic fields, and mirror this unit cell into an infinite array. The two-port scattering parameters are recorded and used for retrieving the effective material properties using the method discussed in Appendix B. If the wire array is assumed to be a homogeneous, isotropic medium of thickness L in the propagating direction, the extracted relative permittivity, Figure 1.7b, shows a negative real part in the X-band region.

A split-ring resonator structure was later shown by Pendry *et al.* [25] to exhibit a negative real permeability

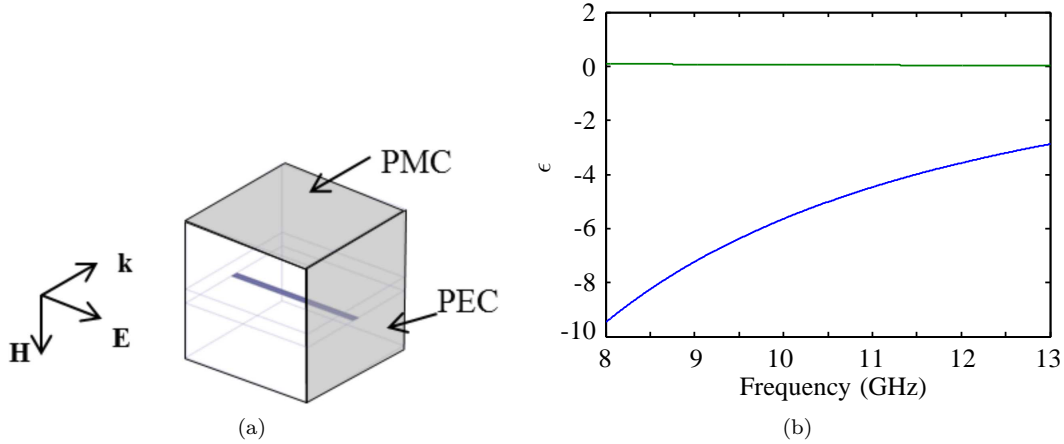


Figure 1.7: (a) The unit cell of the wire metamaterial has dimensions of $2.5\text{mm} \times 2.5\text{mm} \times 2.5\text{mm}$, with wire length = 2.5mm and wire width = 0.14mm . (b) The extracted effective relative permittivity where the blue and green curves represent ϵ' and ϵ'' , respectively.

over a frequency bandwidth. This structure was used in many interesting designs and applications, including negative index materials [19,27,32,33], electromagnetic cloaks [1,4], and filters [34]. SRRs have also been shown to exhibit negative permittivity [35,36]. This property is further investigated with HTS SRR in Chapter 3. Many of the demonstrated circuits exhibit significant loss, which can be reduced by using superconductors. Ricci *et al.* [37–39] investigated superconducting metamaterials made of Niobium (Nb) SRRs deposited on single crystal quartz substrates and Nb wires. Nb has a critical temperature (T_c) of $\approx 9.2\text{K}$ and requires, e.g., the use of liquid Helium for cooling. Chen *et al.* [40] studied the resonant properties of terahertz HTS Jerusalem cross metamaterial, made of $\text{YBa}_2\text{Cu}_3\text{O}_{7-\delta}$ (YBCO) with $\delta=0.05$ and has a T_c of 90K . The use of HTS in metamaterial designs is of interest since experiments can be carried out with liquid nitrogen or low cost, low power cryocoolers.

To demonstrate the negative permeability, a plane wave incident on an array of SRRs was modeled in HFSS, with the magnetic field component normal to the plane of the split-ring resonator, as shown in Figure 1.8. Electric and magnetic walls mirror the SRR into an infinite array. As with the wire effective medium, the SRR is assumed to make up an effective homogeneous, isotropic medium of thickness L in the propagating direction. The extracted relative permeability, Figure 1.8b, shows a negative real part between 9.97GHz and 11.69GHz . The figure also shows a near-zero relative permeability at frequencies above 11.69GHz . This is of particular interest because the values of μ_r required for the metamaterial radome range from 0 to 0.5 for the

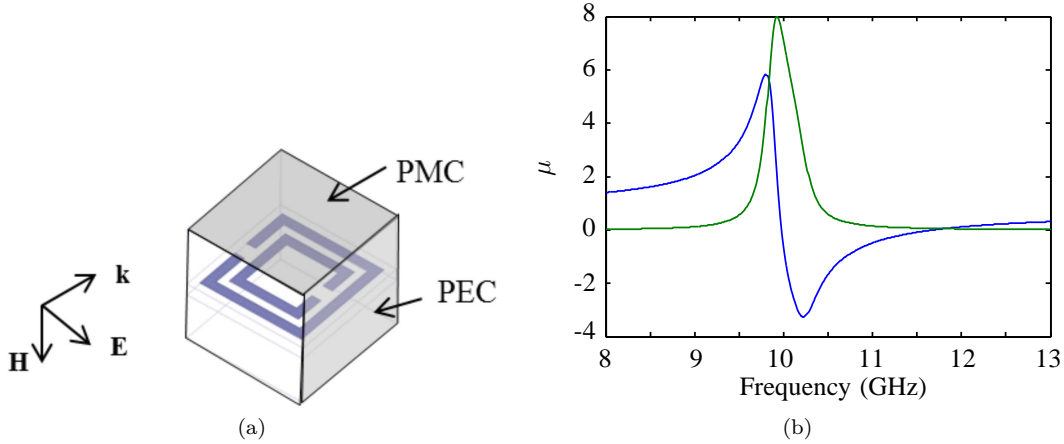


Figure 1.8: (a) The unit cell of the SRR metamaterial has dimensions of $2.5\text{mm} \times 2.5\text{mm} \times 2.5\text{mm}$, with the outer SRR width = 2.2mm , line width = 0.2mm , gap = 0.3mm , and separation between the two rings = 0.15mm . (b) The extracted effective relative permeability where the blue and green curves represent μ' and μ'' , respectively.

example in Figure 1.4.

A composite material that combines the SRR and wire arrays can simultaneously have effective negative permeability, negative permittivity, and negative refraction index in a frequency band. To demonstrate this, a SRR-wire unit cell was modeled in HFSS, as shown in Figure 1.9a, which also includes the polarization of the incident plane wave. Again, the electric and magnetic walls mirror the unit cell into an infinite array. By assuming a homogeneous, isotropic medium for this structure, the effective relative permeability and permittivity are obtained from the S -parameters. The negative permeability and permittivity are still present, seen in Figures 1.9b and 1.9c. In addition, Figure 1.9d also shows a frequency bandwidth with a negative refractive index n' . A similar structure had been constructed and tested by Shelby *et al.* [32]. In his experiment, a wave with an 18° incident angle at the metamaterial/air boundary refracts at -61° , corresponding to a refractive index of -2.7 at 10.5GHz .

1.4 THESIS OUTLINE

The following presents a summary for each of the thesis chapter. Each chapter will contain a summary of previous work, followed by work related to the thesis.

Chapter 2 presents a derivation of the spatial dependent permeability and permittivity for the cylindrical

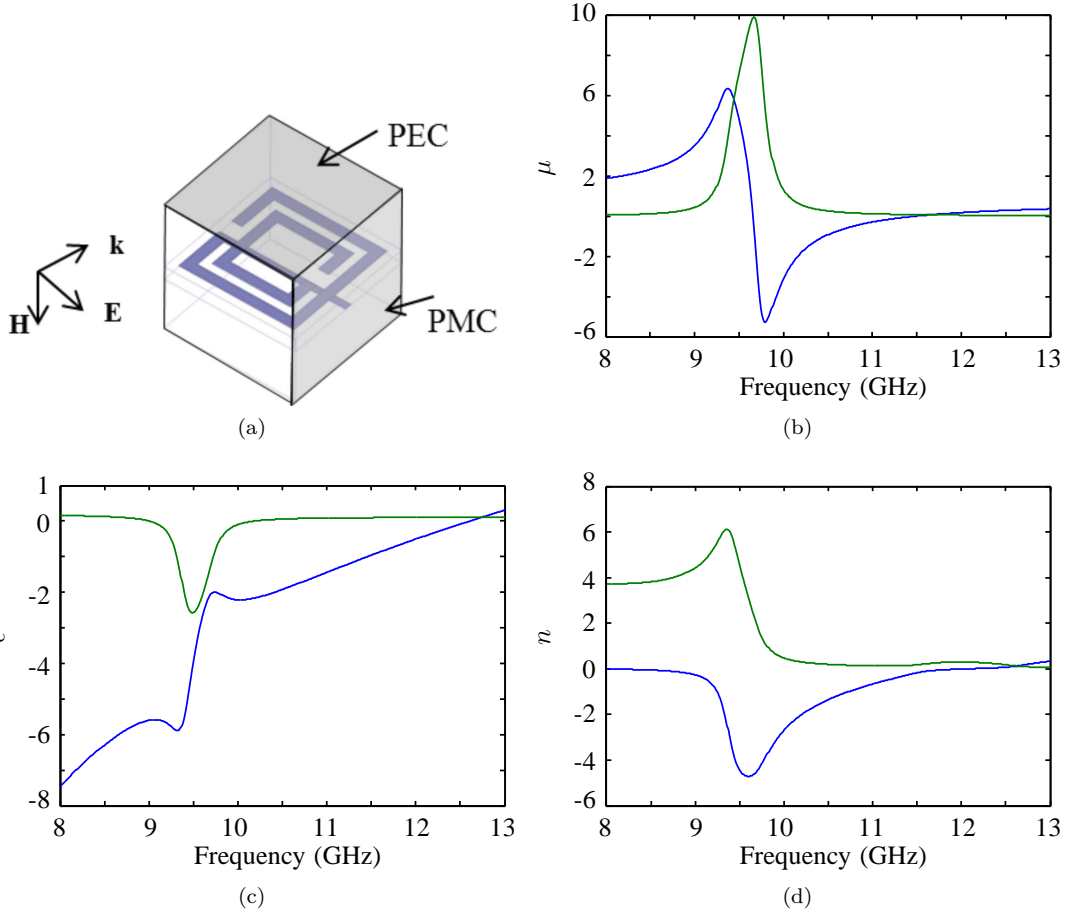


Figure 1.9: (a) shows the unit cell of the SRR-wire metamaterial, where the dimensions were specified in Figures 1.7a and 1.8a. (b), (c), and (d) show the effective relative permeability, permittivity, and refractive index, respectively. The blue and green curves represent the $'$ and $''$ values.

metamaterial radome discussed earlier. It also provides a discussion of the pros and cons of using an ideal versus a realizable set of material properties for the radome. The constitutive parameters of the ideal set take on values defined by Equation (1.4), where all the terms are spatially varying. The realizable set consists of only the ϵ_z , μ_r , and μ_ϕ in the cylindrical coordinates, with μ_r being the only spatial varying term. However, a non-zero reflection coefficient arises if the radome properties are those of the realizable set.

Chapter 3 presents a study of the resonant response of an HTS YBCO SRR structure measured inside a WR-90 X-band rectangular waveguide, of which portions were presented at the 2012 Applied Superconductivity Conference in Portland, Oregon [41] and published in [42]. A cryogenic measurement setup for precise temperature control and the ability to study the SRR resonances from room temperature down to 40 Kelvin is discussed. With this setup, the temperature dependent quality factor of a single SRR at sub- T_C temperature

was studied. The temperature dependent resonance frequency of a single SRR is then fitted to a theoretical model to study the kinetic inductance and London penetration depth. From model fitting, the T_C of YBCO and geometric resonance frequency were also inferred. Finally, the effective permittivity and permeability of the SRR structure at 89 K and 90 K were extracted from the measured S -parameters and compared.

Chapter 4 discusses the extracted effective relative permittivity and permeability of YBCO SRR arrays deposited on a magnesium oxide substrate from waveguide measurements at liquid nitrogen temperature. Portions of this work have been submitted to the IEEE Transactions on Applied Superconductivity and the manuscript is under review. A discussion of the waveguide extraction method is presented. The method is validated through simulations and extraction of the effective parameter of a homogeneous anisotropic medium. Copper and YBCO SRR arrays are then fabricated, measured, and their extracted results are compared. Here, the SRR array is treated as a homogeneous medium described by the biaxial permittivity and permeability (diagonal) tensor. The goals from this study are to:

- Demonstrate a negative effective real permeability in the X-band frequency.
- Show that the imaginary part of the effective permeability quickly drops to near zero at frequencies where the real part $\mu' < 0$, a property not observed in the copper SRR arrays on the Rogers 3010 substrate.
- Show that the retrieved parameters agree with the values extracted from the plane wave approach.

Chapter 5 presents the design, simulations, and measurements of the metamaterial radome discussed in this chapter and Chapter 2. We will begin by defining the measurement environment, which is a parallel plate waveguide, and the criteria for evaluating the performance of the radome. Prior to fabricating the HTS SRR arrays for the radome, we measured a radome constructed of copper SRR arrays to validate the HFSS full-wave simulations. This then allows us to optimize the HTS SRR dimensions in the simulations and be confident that the measurements will agree with the simulation. Next, the cryogenic measurement setup for the HTS radome characterization is discussed. Finally, the measured results will be presented and discussed.

Chapter 6 provides a summary of the completed work and the contributions. Suggestions for future work are also discussed.

From the research work, the following papers and conference presentations are produced:

- Publications

- * [43] F. Trang, H. Rogalla, and Z. Popović, “Effective Constitutive Parameters of High-Temperature Superconducting Split-Ring Resonator Arrays,” *IEEE Transactions on Applied Superconductivity*, (Submitted, under review).
- * [42] F. Trang, H. Rogalla, and Z. Popović, “Resonant Response of High-Temperature Superconducting Split-Ring Resonators,” *IEEE Transactions on Applied Superconductivity*, vol. 23, no. 3, pp. 1300405, Jun. 2013.
- * [44] F. Trang, E. F. Kuester, H. Rogalla, and Z. Popović, “Sensitivity of Double-Sided Split Ring Resonator Arrays to Fabrication Tolerances,” *arXiv e-prints*, 1207.4211, Jul. 2012.

- Conference Presentations

- * [41] F. Trang, H. Rogalla, and Z. Popović, “Resonant Response of High Temperature Superconducting Split-Ring Resonators,” *Applied Superconductivity Conference*, Portland, OR., Oct. 2012.
- * [45] F. Trang, E. F. Kuester, H. Rogalla, and Z. Popović, “Fabrication Sensitivity of Double-Sided Split-Ring Resonator Arrays,” *USNC-URSI*, Boulder, CO., Jan. 2012.

CHAPTER 2

CONSTITUTIVE PARAMETER TRANSFORMATIONS

CONTENTS

- 2.1 Introduction 16
- 2.2 Constitutive Tensor Transformation 17
- 2.3 Transformation for a Cylindrical Cloak 21
- 2.4 Realizable Parameter Set 25

2.1 INTRODUCTION

In the introductory chapter, an electromagnetic guiding structure (metamaterial cloak) was discussed, which has material properties that depend on its geometry and dimensions. It was stated that in order to guide the EM wave around a cylindrical cloak, thus fully isolating the interior and not disturbing the exterior field pattern, the structure must ideally have the following permeability and permittivity properties

$$\frac{\boldsymbol{\mu}}{\mu_0} = \frac{\boldsymbol{\epsilon}}{\epsilon_0} = \text{diag} \left[\frac{r-a}{r}, \frac{r}{r-a}, \left(\frac{b}{b-a} \right)^2 \frac{r-a}{r} \right] \quad (\text{Cylindrical}) \quad (2.1)$$

where a and b are the inner and outer radii, respectively. The variable r is the radial distance from the center of the structure. A popular method for deriving the electromagnetic properties of such a medium is by the coordinate transformation method presented by Ward and Pendry [15]. This chapter presents a derivation for Equation (2.1). The derivation for the constitutive parameters is adapted from the approach presented in Pu Zhang’s Ph.D. dissertation [17]. Zhang derived the transformed parameters by studying the form invariance of Ampère’s law. Here, it will be shown that the same transformed results can be obtained by studying the form invariance of Faraday’s law. Schurig *et al.* [16] also provide a similar transformation approach making use of the form invariance of Maxwell’s equations. The mathematics of tensors used here are explained in Appendix C; no background on the subject is required. For the interested reader, the topic is well presented in Synge and Schild [46] and Dalarsson and Dalarsson [47].

For this chapter, the transformation mathematics for deriving the material properties of an EM guiding structure is presented. Appendix C provides the supplemental tensor mathematics. Next, the relative permittivity and permeability tensors for a cylindrical radome of inner radius a and outer radius b are obtained. It can be seen from Equation (2.1) that all the quantities are spatially varying and the ϕ components are infinite at $r = a$. Thus, designing a material with these properties is difficult, if not impossible. Because the radome is measured inside a parallel plate waveguide, the only relevant parameters are μ_r , μ_ϕ , and ϵ_z . Finally, we will discuss the realizable parameter set for the radome. The drawbacks for using the realizable material properties will also be discussed.

2.2 CONSTITUTIVE TENSOR TRANSFORMATION

It will be shown that Faraday’s law is form invariant, i.e. it retains its form regardless of coordinate systems, from which the transformed material parameters are obtained. The form invariance of Ampère’s law can be shown by similar arguments, as presented in [17]. For our discussion here, Maxwell’s equations and the constitutive parameters are initially assumed to be written in functions in the original space. The constitutive parameters are also assumed to be linear. Our goal is to express them in terms of the transformed space

Cartesian quantities. Recall that the differential form of Faraday's law is

$$\nabla \times \mathbf{E} = -\frac{\partial \mathbf{B}}{\partial t} \quad (2.2)$$

Each of the field components can be written in the curvilinear or Cartesian coordinate systems, e.g.,

$$\mathbf{E} = e_i \mathbf{a}^i = e^i \mathbf{a}_i = E^i \mathbf{x}_i \quad (2.3)$$

$$\mathbf{H} = h_i \mathbf{a}^i = h^i \mathbf{a}_i = H^i \mathbf{x}_i \quad (2.4)$$

$$\mathbf{D} = d_i \mathbf{a}^i = d^i \mathbf{a}_i = D^i \mathbf{x}_i \quad (2.5)$$

$$\mathbf{B} = b_i \mathbf{a}^i = b^i \mathbf{a}_i = B^i \mathbf{x}_i \quad (2.6)$$

where the lower case letters represent curvilinear components and uppercase letters represent Cartesian components. The superscript and subscript combination of the index indicate summation over all possible values, written with the Einstein summation notation, e.g.

$$E^i \mathbf{x}_i = \sum_{i=1}^3 E_i \mathbf{x}_i \quad (2.7)$$

We now take the surface integral of the curl of \mathbf{E} over a differential area and apply Stoke's theorem along path of the area, with the integration path as shown in Figure 2.1. Thus we have,

$$\begin{aligned} \int_S (\nabla \times \mathbf{E}) \cdot d\mathbf{S} &= \oint_C \mathbf{E} \cdot d\mathbf{l} \\ &= \mathbf{E} \cdot \mathbf{a}_1 dp^{1'} + \left[\mathbf{E} \cdot \mathbf{a}_2 dp^{2'} + \frac{\partial(\mathbf{E} \cdot \mathbf{a}_2 dp^{2'})}{\partial p^{1'}} dp^{1'} \right] \\ &\quad - \left[\mathbf{E} \cdot \mathbf{a}_1 dp^{1'} + \frac{\partial(\mathbf{E} \cdot \mathbf{a}_1 dp^{1'})}{\partial p^{2'}} dp^{2'} \right] - \mathbf{E} \cdot \mathbf{a}_2 dp^{2'} \\ &= \frac{\partial(\mathbf{E} \cdot \mathbf{a}_2 dp^{2'})}{\partial p^{1'}} dp^{1'} - \frac{\partial(\mathbf{E} \cdot \mathbf{a}_1 dp^{1'})}{\partial p^{2'}} dp^{2'} \\ &= \left[\frac{\partial e_2}{\partial dp^{1'}} - \frac{\partial e_1}{\partial dp^{2'}} \right] dp^{1'} dp^{2'} \end{aligned} \quad (2.8)$$

where

$$\mathbf{E} \cdot \mathbf{a}_1 = (e_1 \mathbf{a}^1 + e_2 \mathbf{a}^2 + e_3 \mathbf{a}^3) \cdot \mathbf{a}_1 = e_1$$

The partial derivative terms, e.g. $\frac{\partial(\mathbf{E} \cdot \mathbf{a}_2 dp^{2'})}{\partial p^{1'}} dp^{1'}$, account for the differential change in displacement, e.g. from 0 to $dp^{1'}$. Noting that

$$e_i = \Lambda_{i'}^j E_j = \Lambda_{i'}^j \Lambda_j^{i'} E_i = E_i \quad (2.9)$$

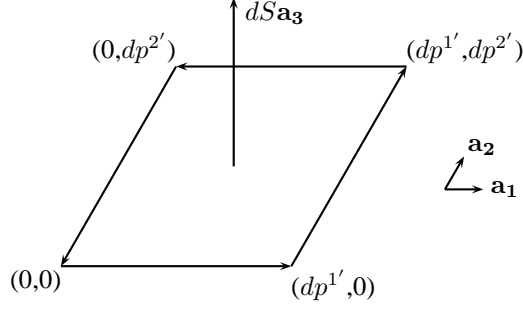


Figure 2.1: Integration path for $\mathbf{E} \cdot d\mathbf{l}$.

Equation (2.8) then becomes

$$\int (\nabla \times \mathbf{E}) \cdot d\mathbf{S} = \left[\frac{\partial E'_1}{\partial dp^{2'}} - \frac{\partial E'_2}{\partial dp^{1'}} \right] dp^{1'} dp^{2'} \quad (2.10)$$

$$= (\nabla \times \mathbf{E}) \cdot (\mathbf{a}_1 \times \mathbf{a}_2) dp^{1'} dp^{2'} \quad (2.11)$$

We now have

$$(\nabla \times \mathbf{E}) \cdot (\mathbf{a}_1 \times \mathbf{a}_2) = \left[\frac{\partial E'_2}{\partial dp^{1'}} - \frac{\partial E'_1}{\partial dp^{2'}} \right] \quad (2.12)$$

$$= (\nabla' \times \mathbf{E}')^3 \quad (2.13)$$

where the superscript 3 represents the third component of the Cartesian coordinates.

The right hand side of Equation (2.2) can also be expressed in the prime coordinates. We assume time-invariant constitutive parameters. Again, taking the surface integral of the right hand side of Equation (2.2), we have

$$- \int \frac{\partial \mathbf{B}}{\partial t} \cdot d\mathbf{S} = - \int \frac{\partial \mathbf{B}}{\partial t} \cdot (\mathbf{a}_1 \times \mathbf{a}_2) dp^{1'} dp^{2'} \quad (2.14)$$

The term inside the integral is thus

$$\frac{\partial \mathbf{B}}{\partial t} \cdot (\mathbf{a}_1 \times \mathbf{a}_2) = - \frac{\partial b^i}{\partial t} \mathbf{a}_i \cdot (\mathbf{a}_1 \times \mathbf{a}_2) \quad (2.15)$$

$$= - \frac{\partial b^3}{\partial t} \mathbf{a}_3 \cdot (\mathbf{a}_1 \times \mathbf{a}_2) \quad (2.16)$$

$$= - \Lambda_i^{3'} \mu_j^i \Lambda_{k'}^j g^{kl} \det(\mathbf{\Lambda}^{-1}) \frac{\partial H'_l}{\partial t} \quad (2.17)$$

where

$$\begin{aligned}
b^3 &= \Lambda_i^{3'} B^i = \Lambda_i^{3'} \mu_j^i H^j = \Lambda_i^{3'} \mu_j^i \Lambda_{k'}^j h^k \\
&= \Lambda_i^{3'} \mu_j^i \Lambda_{k'}^j g^{kl} h_l \\
&= \Lambda_i^{3'} \mu_j^i \Lambda_{k'}^j g^{kl} H_l'
\end{aligned} \tag{2.18}$$

and

$$\mathbf{a}_3 \cdot (\mathbf{a}_1 \times \mathbf{a}_2) = (\Lambda_{3'}^k \mathbf{x}_k) \cdot (\Lambda_{1'}^i \mathbf{x}_i \times \Lambda_{2'}^j \mathbf{x}_j) \tag{2.19}$$

$$= \Lambda_{1'}^i \Lambda_{2'}^j \Lambda_{3'}^k \mathbf{x}_k \cdot (\mathbf{x}_i \times \mathbf{x}_j) \tag{2.20}$$

$$= \det(\mathbf{\Lambda}^{-1}) \tag{2.21}$$

The vectors \mathbf{x}_i are simply unit vectors since the metric tensors in the Cartesian coordinate system are just δ_{ij} and δ^{ij} . In other words,

$$\frac{\mathbf{x}_i}{\sqrt{\mathbf{x}_i \cdot \mathbf{x}_i}} = \frac{\mathbf{x}_i}{\sqrt{\delta_{ii}}} = \mathbf{x}_i \quad \text{and} \quad \frac{\mathbf{x}^i}{\sqrt{\mathbf{x}^i \cdot \mathbf{x}^i}} = \frac{\mathbf{x}^i}{\sqrt{\delta^{ii}}} = \mathbf{x}^i \tag{2.22}$$

The relationship between the metric tensors in the curvilinear and Cartesian coordinates, from Equations (C.7) and (C.10), is as followed

$$g_{ij} = \Lambda_{i'}^k \Lambda_{j'}^l \delta_{kl} \quad \text{and} \quad g^{ij} = \Lambda_k^{i'} \Lambda_l^{j'} \delta^{kl} \tag{2.23}$$

Note that

$$g_{11} = \left(\frac{\partial p^1}{\partial p^{1'}} \right)^2 + \left(\frac{\partial p^2}{\partial p^{1'}} \right)^2 + \left(\frac{\partial p^3}{\partial p^{1'}} \right)^2 \quad \text{and} \quad g^{11} = \left(\frac{\partial p^{1'}}{\partial p^1} \right)^2 + \left(\frac{\partial p^{1'}}{\partial p^2} \right)^2 + \left(\frac{\partial p^{1'}}{\partial p^3} \right)^2 \tag{2.24}$$

Then in matrix form, Equation (2.23) can be written as

$$\mathbf{g} = (g_{ij}) = (\mathbf{\Lambda}^{-1})^T \mathbf{\Lambda}^{-1} \quad \text{and} \quad \mathbf{g}^{-1} = (g^{ij}) = \mathbf{\Lambda} \mathbf{\Lambda}^T \tag{2.25}$$

Equations (2.13) and (2.17) can be substituted by into Equation (2.2) resulting in

$$(\nabla' \times \mathbf{E}')^3 = -\Lambda_i^{3'} \mu_j^i \Lambda_{k'}^j g^{kl} \det(\mathbf{\Lambda}^{-1}) \frac{\partial H_l'}{\partial t} \tag{2.26}$$

or more generally

$$(\nabla' \times \mathbf{E}')^m = -\Lambda_i^{m'} \mu_j^i \Lambda_{k'}^j g^{kl} \det(\mathbf{\Lambda}^{-1}) \frac{\partial H_l'}{\partial t} \tag{2.27}$$

and in matrix form

$$\begin{aligned} (\nabla' \times \mathbf{E}') &= -\mathbf{\Lambda} \boldsymbol{\mu} \mathbf{\Lambda}^{-1} \mathbf{g}^{-1} \det(\mathbf{\Lambda}^{-1}) \frac{\partial \mathbf{H}'}{\partial t} \\ &= -\boldsymbol{\mu}' \frac{\partial \mathbf{H}'}{\partial t} \end{aligned} \quad (2.28)$$

Thus we have shown the form invariance of Faraday's law for coordinate transformations. The equation in the original and transformed spaces have the same form. The difference is a different definition of the material property in the two spaces. With the help of Equation (2.25), we get

$$\boldsymbol{\mu}' = \mathbf{\Lambda} \boldsymbol{\mu} \mathbf{\Lambda}^T \det(\mathbf{\Lambda}^{-1}) \quad (2.29)$$

By following a similar argument and starting with Ampère's law, we can show the permittivity transformation

$$\boldsymbol{\epsilon}' = \mathbf{\Lambda} \boldsymbol{\epsilon} \mathbf{\Lambda}^T \det(\mathbf{\Lambda}^{-1}) \quad (2.30)$$

2.3 TRANSFORMATION FOR A CYLINDRICAL CLOAK

Next, the result from Equation (2.29) is used to solve for the constitutive parameters of a cylindrical cloak in the transformed polar coordinate system. Let us now define a transformed space, in which the space inside a cylindrical volume of radius b is compressed into a cylindrical shell of inner radius a and outer radius b , as shown in Figure 2.2. Mathematically, the transformation equations are

$$r' = \frac{b-a}{b}r + a \quad \phi' = \phi \quad z' = z \quad (2.31)$$

To transform into such a space, we will break up the Jacobian matrix from equation (C.5) into three steps, such that

$$\begin{aligned} \mathbf{\Lambda} = \left(\Lambda_i^{j'} \right) &= \left(\frac{\partial p^{j'}}{\partial p^i} \right) = \left(\frac{\partial p^{j'}}{\partial q^{k'}} \right) \left(\frac{\partial q^{k'}}{\partial q^l} \right) \left(\frac{\partial q^l}{\partial p^i} \right) \\ &= \left(T_{j'}^{k'} \right)^{-1} \left(Q_i^{j'} \right) \left(T_i^l \right) \\ &= \left(\mathbf{T}' \right)^{-1} \mathbf{Q} \mathbf{T} \end{aligned} \quad (2.32)$$

In the above equation, p^i , q^i , $p^{i'}$, and $q^{i'}$ represent components in the original Cartesian, original orthogonal curvilinear, transformed Cartesian, and transformed orthogonal curvilinear coordinate systems, respectively.

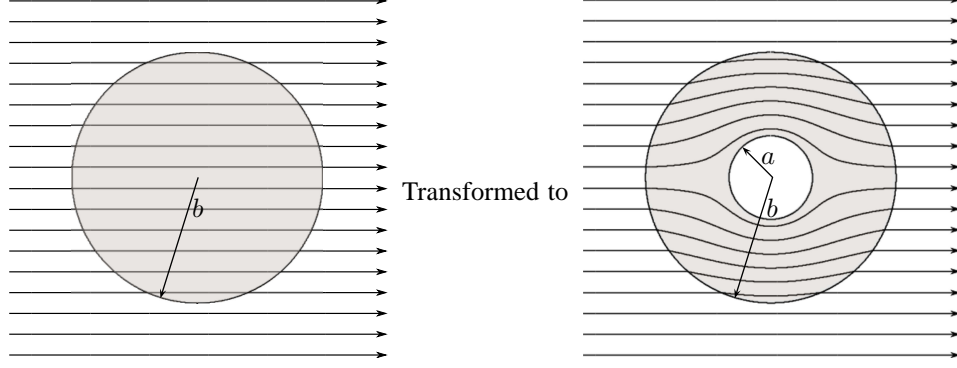


Figure 2.2: Transformation from the original space (a) to the transformed space (b), in which the space inside a volume of radius b is compressed into a cylindrical shell of inner radius a and outer radius b .

Notice that Equations (2.29) and (2.30) transform the permeability and permittivity tensors from the original Cartesian space to the transformed Cartesian space. By injecting the transformations involving the polar coordinates in between, we can obtain quantities in the transformed space in the following sense.

Original		Original		Transformed		Transformed
Cartesian	→	Curvilinear	→	Curvilinear	→	Cartesian
(p^i)		(q^i)		$(q^{i'})$		$(p^{i'})$

Similar to Equation (2.25), we can also write the metric tensor in the orthogonal curvilinear coordinate system as

$$\hat{\mathbf{g}} = (\mathbf{T}^{-1})^T \mathbf{T}^{-1} \quad \text{and} \quad \hat{\mathbf{g}}^{-1} = \mathbf{T} \mathbf{T}^T \quad (2.33)$$

with

$$\hat{g}_{ij} = \mathbf{b}_i \cdot \mathbf{b}_j = h_i^2 \delta_{ij} \quad (2.34)$$

where h_i is the scale factor and \mathbf{b}_i are the basis vectors of this system. Quantities of the orthogonal curvilinear system are represented with a hat over them. The magnetic flux density and magnetic field are related by

$$\hat{b}^i = \hat{\mu}_j^i \hat{h}^j \quad (2.35)$$

or in matrix form

$$\hat{\mathbf{b}} = \hat{\boldsymbol{\mu}} \hat{\mathbf{h}} \quad (2.36)$$

Using the transformation rules from Equations (C.4) and (C.10), but extending them for the second order mixed tensor case, the permeability in the Cartesian system and curvilinear system are related by

$$\mu_i^j = \frac{\partial p^j}{\partial q^k} \frac{\partial q^l}{\partial p^i} \hat{\mu}_l^k \quad (2.37)$$

Note that the Cartesian permeability component is represented without a hat. In matrix form, the permeability in original and transformed spaces are

$$\boldsymbol{\mu} = \mathbf{T}^{-1} \hat{\boldsymbol{\mu}} \mathbf{T} \quad (2.38)$$

$$\boldsymbol{\mu}' = \mathbf{T}'^{-1} \hat{\boldsymbol{\mu}}' \mathbf{T}' \quad (2.39)$$

We can rewrite Equation (2.29) in terms of the new quantities as

$$\begin{aligned} \hat{\boldsymbol{\mu}}' &= \mathbf{T}' \boldsymbol{\mu}' \mathbf{T}'^{-1} \\ &= \mathbf{T}' \mathbf{T}'^{-1} \mathbf{Q} \mathbf{T} \mathbf{T}^{-1} \hat{\boldsymbol{\mu}} \mathbf{T} \mathbf{T}^T \mathbf{Q}^T (\mathbf{T}'^{-1})^T \det(\boldsymbol{\Lambda}^{-1}) \mathbf{T}'^{-1} \\ &= \mathbf{Q} \hat{\boldsymbol{\mu}} \hat{\boldsymbol{\mathbf{g}}}^{-1} \mathbf{Q}^T \hat{\boldsymbol{\mathbf{g}}}' \det(\boldsymbol{\Lambda}^{-1}) \end{aligned} \quad (2.40)$$

The resulting permeability had been computed based on the definition of the basis vectors, which in general do not have unit length. Therefore, we need to scale it to use the unit vectors of the coordinate systems. Let \mathbf{v}_i be the unit vectors. Then, \mathbf{B} and \mathbf{H} can be written as

$$\mathbf{B} = \hat{B}^i \mathbf{v}_i = \hat{b}^i \mathbf{b}_i \quad \text{and} \quad \mathbf{H} = \hat{H}^i \mathbf{v}_i = \hat{h}^i \mathbf{b}_i \quad (2.41)$$

where \hat{B}^i and \hat{H}^i are the scaled components of \hat{b}^i and \hat{h}^i , with the relationship being

$$\hat{B}^i = h_i \hat{b}^i \quad \text{and} \quad \hat{H}^i = h_i \hat{h}^i \quad (2.42)$$

or

$$\hat{\mathbf{B}} = \hat{\mathbf{g}}^{1/2} \hat{\mathbf{b}} \quad \text{and} \quad \hat{\mathbf{H}} = \hat{\mathbf{g}}^{1/2} \hat{\mathbf{h}} \quad (2.43)$$

In Equation (2.42), h_i without a hat is the scale factor. The unit vector \mathbf{v}_i is just

$$\mathbf{v}_i = \frac{\mathbf{b}_i}{\sqrt{\mathbf{b}_i \cdot \mathbf{b}_i}} = \frac{\mathbf{b}_i}{h_i} \quad (2.44)$$

We will now define a new permeability tensor, $\hat{\boldsymbol{\mu}}$, that operates in the space defined by the unit vectors rather than the basis vectors.

$$\hat{\mathbf{B}} = \hat{\boldsymbol{\mu}}\hat{\mathbf{H}} \quad (2.45)$$

$$\hat{\mathbf{g}}^{1/2}\hat{\mathbf{b}} = \hat{\boldsymbol{\mu}}\hat{\mathbf{g}}^{1/2}\hat{\mathbf{h}} \quad (2.46)$$

By substituting $\hat{\mathbf{b}}$ from Equation (2.36), we have

$$\hat{\boldsymbol{\mu}} = \hat{\mathbf{g}}^{1/2}\hat{\boldsymbol{\mu}}\hat{\mathbf{g}}^{-1/2} \quad (2.47)$$

Finally, we need to transform the quantities from the original space to the transformed space. As with Equation (2.39), $\hat{\boldsymbol{\mu}}$ in the transformed space is

$$\hat{\boldsymbol{\mu}}' = \hat{\mathbf{g}}'^{1/2}\hat{\boldsymbol{\mu}}'\hat{\mathbf{g}}'^{-1/2} \quad (2.48)$$

Together with Equation (2.40), in the transformed curvilinear coordinates,

$$\begin{aligned} \hat{\boldsymbol{\mu}}' &= \hat{\mathbf{g}}'^{1/2}\mathbf{Q}\hat{\boldsymbol{\mu}}\hat{\mathbf{g}}^{-1}\mathbf{Q}^T\hat{\mathbf{g}}'\det(\boldsymbol{\Lambda}^{-1})\hat{\mathbf{g}}'^{-1/2} \\ &= \hat{\mathbf{g}}'^{1/2}\mathbf{Q}\hat{\mathbf{g}}^{-1/2}\hat{\boldsymbol{\mu}}\hat{\mathbf{g}}^{1/2}\hat{\mathbf{g}}^{-1}\mathbf{Q}^T\hat{\mathbf{g}}'\det(\boldsymbol{\Lambda}^{-1})\hat{\mathbf{g}}'^{-1/2} \\ &= \hat{\mathbf{g}}'^{1/2}\mathbf{Q}\hat{\mathbf{g}}^{-1/2}\hat{\boldsymbol{\mu}}\hat{\mathbf{g}}^{-1/2}\mathbf{Q}^T\hat{\mathbf{g}}'^{1/2}\det(\mathbf{T}'^{-1}\mathbf{Q}\mathbf{T})^{-1} \\ &= \hat{\mathbf{g}}'^{1/2}\mathbf{Q}\hat{\mathbf{g}}^{-1/2}\hat{\boldsymbol{\mu}}\hat{\mathbf{g}}^{-1/2}\mathbf{Q}^T\hat{\mathbf{g}}'^{1/2}/\det(\hat{\mathbf{g}}'^{1/2}\mathbf{Q}\hat{\mathbf{g}}^{-1/2}) \end{aligned} \quad (2.49)$$

where

$$\hat{\mathbf{g}}^{-1/2} = \sqrt{\mathbf{T}\mathbf{T}^T} \quad (2.50)$$

$$\hat{\mathbf{g}}'^{-1/2} = \sqrt{\mathbf{T}'\mathbf{T}'^T} \quad (2.51)$$

For the coordinates transformation defined by Figure 2.2 and Equation (2.31), we have

$$\mathbf{T} = \begin{bmatrix} \frac{\partial r}{\partial x} & \frac{\partial r}{\partial y} & \frac{\partial r}{\partial z} \\ \frac{\partial \phi}{\partial x} & \frac{\partial \phi}{\partial y} & \frac{\partial \phi}{\partial z} \\ \frac{\partial z}{\partial x} & \frac{\partial z}{\partial y} & \frac{\partial z}{\partial z} \end{bmatrix} = \begin{bmatrix} \cos \phi & \sin \phi & 0 \\ -\frac{\sin \phi}{r} & \frac{\cos \phi}{r} & 0 \\ 0 & 0 & 1 \end{bmatrix} \quad (2.52)$$

$$\hat{\mathbf{g}}^{-1/2} = \text{diag} \left[1, \frac{1}{r}, 1 \right] \quad (2.53)$$

$$\hat{\mathbf{g}}'^{-1/2} = \text{diag} \left[1, \frac{1}{r'}, 1 \right] \quad (2.54)$$

$$\mathbf{Q} = \begin{bmatrix} \frac{\partial r'}{\partial r} & \frac{\partial r'}{\partial \phi} & \frac{\partial r'}{\partial z} \\ \frac{\partial \phi'}{\partial r} & \frac{\partial \phi'}{\partial \phi} & \frac{\partial \phi'}{\partial z} \\ \frac{\partial z}{\partial r} & \frac{\partial z}{\partial \phi} & \frac{\partial z}{\partial z} \end{bmatrix} = \text{diag} \left[\frac{b-a}{b}, 1, 1 \right] \quad (2.55)$$

If we assume vacuum for our original space, such that

$$\frac{\hat{\boldsymbol{\mu}}}{\mu_0} = \text{diag} [1, 1, 1] \quad (2.56)$$

then the relative permeability tensor ($\hat{\boldsymbol{\mu}}'/\mu_0$) in the transformed polar coordinate system for the transformation described by Equation (2.31) becomes

$$\frac{\hat{\boldsymbol{\mu}}'}{\mu_0} = \text{diag} \left[\frac{r' - a}{r'}, \frac{r'}{r' - a}, \left(\frac{b}{b - a} \right)^2 \frac{r' - a}{r'} \right] \quad (2.57)$$

By the same argument, we also have

$$\frac{\hat{\boldsymbol{\epsilon}}'}{\epsilon_0} = \text{diag} \left[\frac{r' - a}{r'}, \frac{r'}{r' - a}, \left(\frac{b}{b - a} \right)^2 \frac{r' - a}{r'} \right] \quad (2.58)$$

A plot of $\hat{\boldsymbol{\mu}}'/\mu_0$ and $\hat{\boldsymbol{\epsilon}}'/\epsilon_0$ for $a = 22.9$ mm and $b = 34.9$ mm is shown in Figure 2.3. The ϕ components diverge at the inner region of the cloak. This problem is addressed in the next section.

2.4 REALIZABLE PARAMETER SET

From Equation (2.58) and Figure 2.3, every terms in the material tensors are spatially varying. In addition, μ_ϕ and ϵ_ϕ are infinite at the inner radius $r' = a$. A natural material with these properties does not exist. With the increased interest and understanding of metamaterials, we are now able to engineer composite materials that have the desired effective characteristics, i.e. near zero μ . Even so, designing a material with properties in Figure 2.3 will be a difficult task, if not impossible. Since we know in advanced the experiment

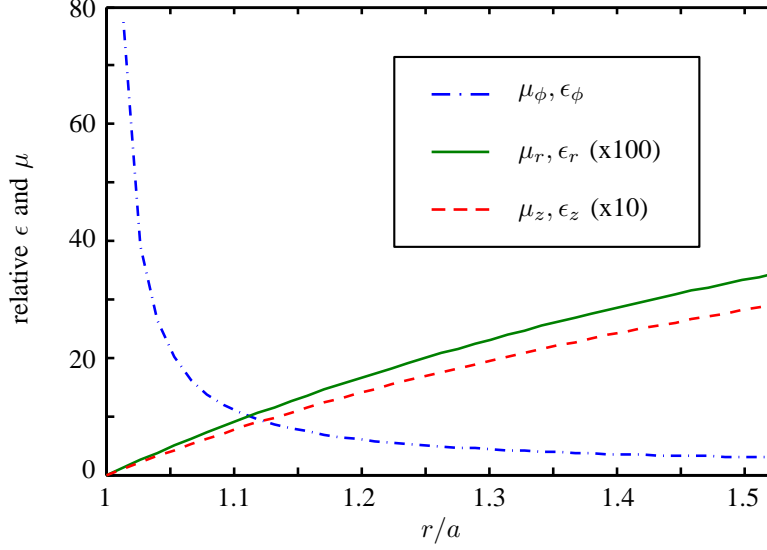


Figure 2.3: Relative permittivity and permeability values for a cylindrical cloak with inner radius $a = 22.9$ mm and outer radius $b = 34.9$ mm. The plot shows the values from a/a to b/a .

environment for characterizing the radome, which will be measured inside a parallel plate waveguide, we can reduce the relevant parameters to just μ_r , μ_ϕ , and ϵ_z in the cylindrical coordinates system.

Consider the case where the fields inside an infinite parallel plate waveguide are $E_r = E_\phi = H_z = 0$ and

$$\mathbf{E} = E_z(r, \phi) \mathbf{u}_z \quad (2.59)$$

$$\mathbf{H} = H_r(r, \phi) \mathbf{u}_r + H_\phi(r, \phi) \mathbf{u}_\phi \quad (2.60)$$

By expanding the Ampère and Faraday's laws in the cylindrical coordinates, the electric and magnetic fields can be reduced to a differential equation

$$j\omega\epsilon_z\epsilon_0 E_z = \frac{1}{r} \left[\frac{\partial(rH_\phi)}{\partial r} - \frac{\partial H_r}{\partial \phi} \right] \quad (2.61)$$

$$j\omega\mu_\phi\mu_0 H_\phi = \frac{\partial E_z}{\partial r} \quad (2.62)$$

$$j\omega\mu_r\mu_0 H_r = -\frac{1}{r} \frac{\partial E_z}{\partial \phi} \quad (2.63)$$

$$E_z = \frac{1}{j\omega\epsilon_z\epsilon_0 r} \left[\frac{\partial(rH_\phi)}{\partial r} - \frac{\partial H_r}{\partial \phi} \right] \quad (2.64)$$

$$= \frac{1}{j\omega\epsilon_z\epsilon_0 r} \left[\frac{\partial}{\partial r} \left(\frac{r}{j\omega\mu_\phi\mu_0} \frac{\partial E_z}{\partial r} \right) + \frac{1}{j\omega\mu_r\mu_0 r} \frac{\partial^2 E_z}{\partial \phi^2} \right] \quad (2.65)$$

Furthermore, if μ_ϕ is assumed to be independent of r , the differential equations becomes

$$\frac{1}{\mu_\phi \epsilon_z} \frac{1}{r} \frac{\partial}{\partial r} \left(r \frac{\partial E_z}{\partial r} \right) + \frac{1}{\mu_r \epsilon_z} \frac{1}{r^2} \frac{\partial^2 E_z}{\partial \phi^2} + k_0^2 E_z = 0 \quad (2.66)$$

where $k_0^2 = \omega^2 \epsilon_0 \mu_0$. This equation depends on the products $\epsilon_z \mu_\phi$ and $\epsilon_z \mu_r$, with the constraint their products must equal

$$\epsilon_z \mu_\phi = \left(\frac{b}{b-a} \right)^2 \quad (2.67)$$

$$\epsilon_z \mu_r = \left(\frac{b}{b-a} \right)^2 \left(\frac{r-a}{r} \right)^2 \quad (2.68)$$

The values of μ and ϵ can be chosen to be

$$\epsilon_z = \left(\frac{b}{b-a} \right)^2 = \text{constant} \quad (2.69)$$

$$\mu_r = \left(\frac{r-a}{r} \right)^2 \quad (2.70)$$

$$\mu_\phi = 1 \quad (2.71)$$

and still have the electric field satisfying Equation (2.66). We now have only a single spatial varying term, μ_r , which is a function of the radius. An effective $\mu_\phi = 1$ can be achieved by using a non-magnetic substrate in the metamaterial. Figure 2.4 shows the realizable parameter set for the inner radius $a = 22.9$ mm and outer radius $b = 34.9$ mm. The value of μ_r is near zero at the inner radius of the cloak. It will be shown in Chapter 4 that a split-ring resonator metamaterial can in fact have an effective near zero relative μ_r . The value of ϵ_z is highly dependent on a and b . The SRR metamaterial can also simultaneously have the desired ϵ_z , over a frequency bandwidth, if the substrate portion of the SRR is chosen correspondingly to the ϵ_z value.

However, a drawback for using the realizable parameter set as properties of the radome is a non-zero reflectance at the outer radius b . The wave impedance, normalized to the free space wave impedance ζ_0 , at the boundary $r = b$ is given by

$$\zeta = \sqrt{\frac{\mu_\phi}{\epsilon_z}} \quad (2.72)$$

For the ideal case, the normalized wave impedance equals 1, resulting in no reflection. For the realizable parameter set, $\zeta = (b-a)/b$ and the reflection coefficient is

$$\Gamma = \frac{-a}{2b-a} \quad (2.73)$$

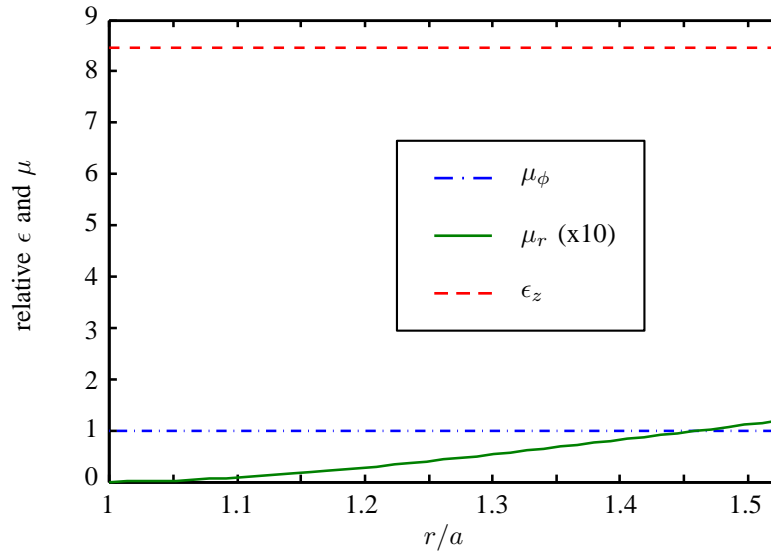


Figure 2.4: Realizable values of the relative permittivity and permeability values for a cylindrical cloak with inner radius $a = 22.9$ mm and outer radius $b = 34.9$ mm. The plot shows the values from a/a to b/a .

To minimize Γ , b should be greater than a .

CHAPTER 3

RESONANT RESPONSE OF HTS SRR

CONTENTS

3.1	Introduction	29
3.2	HTS SRR Fabrication and Measurement Setup	30
3.3	Measurement Results	31
3.4	Temperature Dependent f_r	36
3.5	Effective Constitutive Parameter Extraction	40
3.6	Conclusion	40

3.1 INTRODUCTION

The demonstration of split-ring resonator (SRR) arrays having a negative permeability by Pendry *et al.* [25] has led to many interesting SRR based designs and applications, including negative index materials [19, 27, 32, 33], electromagnetic cloaks [1, 4], and filters [34]. In this chapter, we investigate the resonant response of HTS split-ring resonators made of YBCO thin film deposited on a single crystal magnesium oxide (MgO) substrate. The HTS SRRs are measured inside a WR-90 X-band waveguide over a wide temperature range from 40 K to

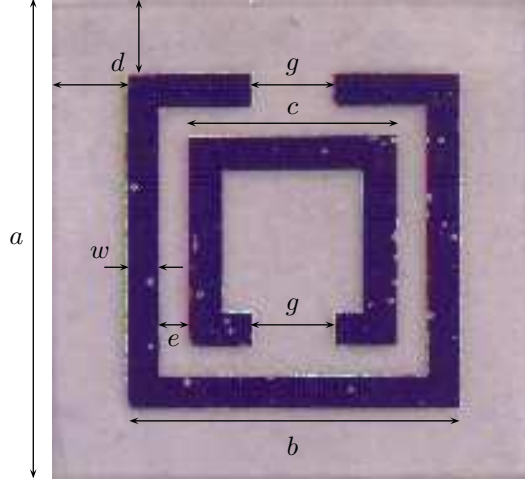


Figure 3.1: A close-up photograph of the SRR unit cell with labeled dimensions, where $a=10$ mm, $b=7$ mm, $c=4.4$ mm, $d=1.5$ mm, $e=0.5$ mm, $g=1.6$ mm, $w=0.8$ mm.

90.5 K. We will begin by briefly discussing the fabrication and geometry of the SRRs. Then, the cryogenic measurement setup, which allows for precise temperature control and the ability to study the resonances as a function of temperature, is discussed. Measurements of an array of seven SRRs inside the waveguide at 77 K and room temperature are compared to the low-loss simulation. Next an individual SRR element is measured over the wide temperature range for investigating the temperature dependence of the resonant frequency and quality factor. The behavior of the measured resonant frequency vs. temperature is fitted to a model to study the kinetic inductance and London penetration depth. Finally, the effective permittivity and permeability are extracted from the measured scattering parameters.

3.2 HTS SRR FABRICATION AND MEASUREMENT SETUP

Each HTS SRR is made up of two 700 nm thick YBCO rings deposited on top of a 500 μm thick, 1 cm^2 MgO substrate that has a nominal relative permittivity of 9.7. Figure 3.1 shows a photograph of a SRR element, with relevant dimensions. A 100 nm coating of cerium oxide (CeO_2) is applied over the YBCO SRRs. A single photoresist contact mask was used in the photolithography process of patterning the SRRs.

The waveguide environment was chosen for measurements because the waveguide components can easily be confined into a cryogenic enclosure and thus can easily be temperature controlled and calibrated. A vacuum sealed cylindrical cryostat is used to confine and cool the waveguide components, which include two aluminum

waveguide to coaxial adapters and a 76.2 mm copper waveguide section for holding the HTS SRRs, as shown in Figure 3.2. The inner diameter of the cryostat is 74 mm and wide enough to hold the waveguide components. Two feedthroughs in the top metal lid allow the rigid copper coaxial cables to connect to a vector network analyzer (VNA). The temperature of the copper waveguide is monitored with an attached temperature sensor. Figure 3.2a is a sketch that shows the placement of the various components inside the cryostat along with the gas flow directions. In the measurement presented here, a variable temperature cryostat is used to investigate a wider range of temperature. Although liquid nitrogen would suffice in cooling our structure to sub- T_C temperature, we were also interested in the responses at temperatures down to 40 K. Figure 3.2b shows a photograph of the waveguide unit that is placed in the flow-type cryostat, where the cold helium gas is supplied from a liquid helium dewar shown in Figure 3.3. The temperature of the waveguide components is regulated by a LakeShore 330 autotuning temperature controller and TRW flow control unit. With this setup, we studied the HTS SRRs from room temperature to 40 K.

An Agilent 8722ES network analyzer was used for the measurements, with the test input power level set to -10 dBm (0.1 mW). The VNA was calibrated to the end of the waveguide adapters with the Thru-Reflect-Line (TRL) method at room temperature, where the reflect standard is a short. The phase error incurred by twisting the coaxial cable in Figure 3.2b is removed through the calibration.

Note that the TE_{10} dominant mode excites an electric field along the sides of the SRR in the x direction (Figure 3.4) and produces an electric resonance, as explained in [35, 36]. What we mean by an electric resonance is the response that is accompanied by an effective negative permittivity. Thus a magnetic resonance corresponds to a region with an effective negative permeability. Because of the metal wall boundary conditions, the single SRR and its images form an infinite array.

3.3 MEASUREMENT RESULTS

An array of seven SRRs, placed inside a WR-90 waveguide with orientation shown in Figure 3.4, was simulated in Ansys HFSS, a full wave finite element method (FEM) solver. In the simulation, the superconductor is modeled with a conductivity of 10^{10} S/m and the MgO substrate with a relative permittivity of 9.7 and a loss tangent of 10^{-6} . The dominant TE_{10} mode was excited in the waveguide, which has an electric field

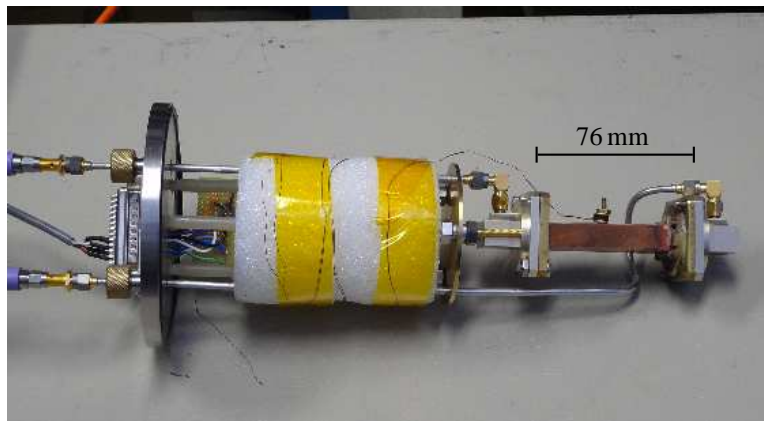
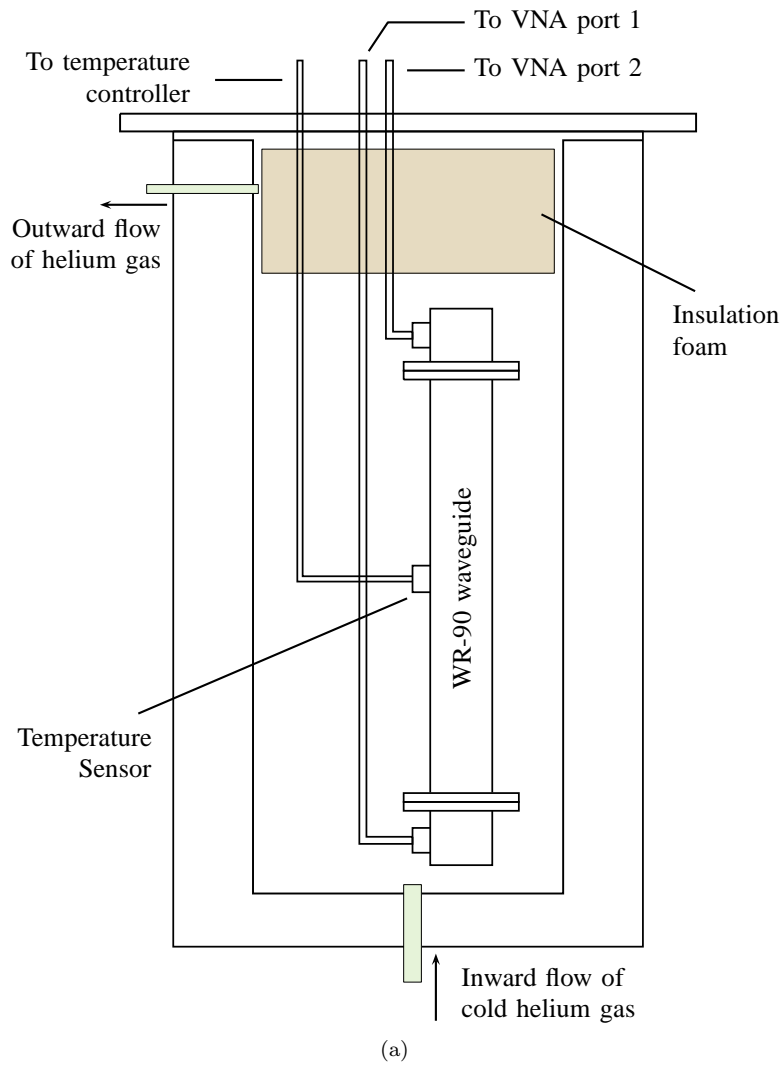


Figure 3.2: (a) A sketch of the cryostat with waveguide components. (b) A photograph of the waveguide setup that fits inside the cryostat.



Figure 3.3: A photograph of the measurement setup, showing the flow-type cryostat on top of a liquid helium filled dewar. To the right of the dewar are the network analyzer, flow control unit, and temperature controller, shown from top down.

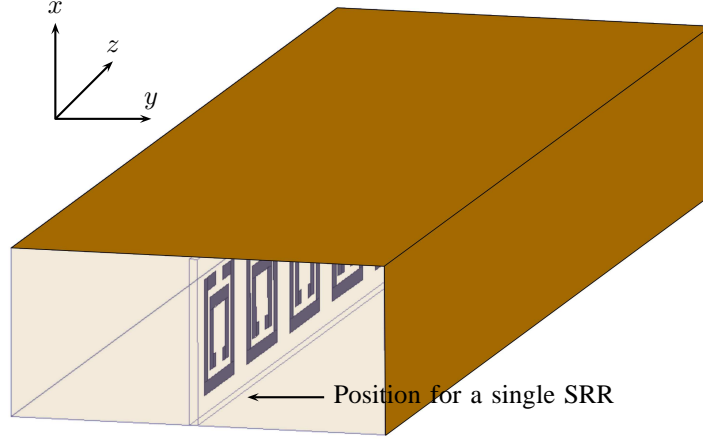


Figure 3.4: Placement of the HTS SRR array inside a WR-90 waveguide. The single element is placed in the same way. See Figure 3.1 for ring dimensions.

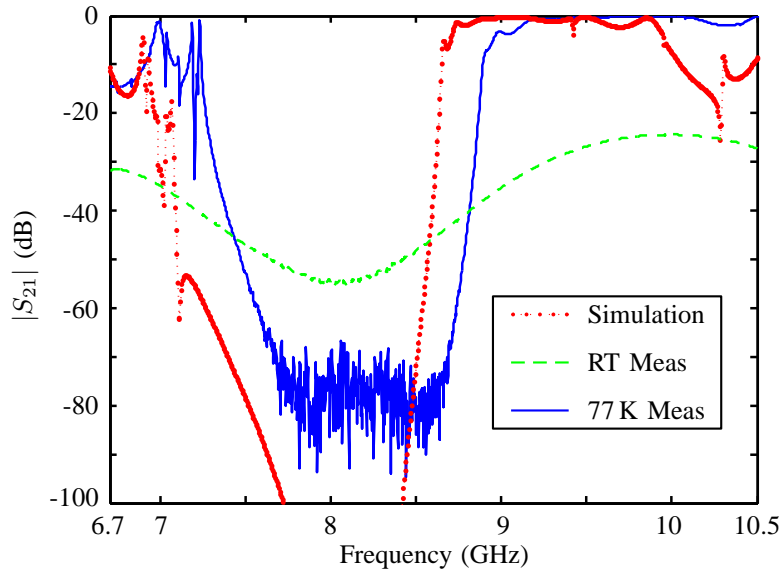


Figure 3.5: Measured and simulated transmission (S_{21}) coefficients of an array of seven HTS SRR placed inside a WR-90 waveguide. The measurements were taken at 77 K (solid blue) and at room temperature (dashed green).

in the x direction (Figure 3.4), with a maximum in the middle and zero on the side walls. The simulated magnitude of the transmission coefficient ($|S_{21}|$) is plotted in Figure 3.5 and shows a pronounced wide stop band centered around 8 GHz. A linear array of seven fabricated HTS SRRs is then placed inside a copper waveguide (Figure 3.4) and measured with a VNA. The measured $|S_{21}|$ at 77 K, plotted together with the simulated result in Figure 3.5, also shows a wide stop band. A room temperature measurement was also taken, shown as the dashed curve in Figure 3.5.

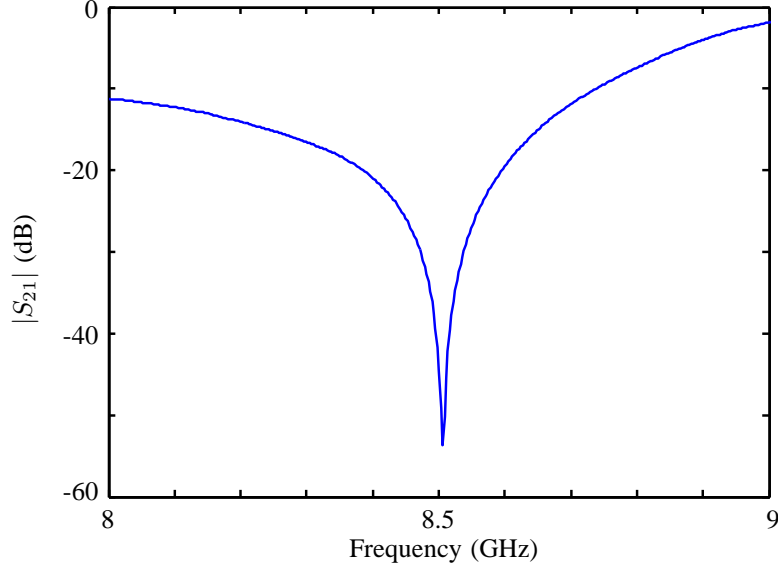


Figure 3.6: Measurement of the transmission resonance (S_{21}) at 85 K.

To study the temperature dependence behavior of the HTS SRR, a single element was placed inside the waveguide and the scattering coefficients were measured as the temperature was varied. At temperature below T_c , the measured transmission resonances are sharp, as seen in Figure 3.6. Due to the limitation of the measurement instrument, it is not possible to fully characterize the exact resonant frequency, minimum $|S_{21}|$, and 3-dB bandwidth directly for each resonance curve. We performed curve fitting to a Lorentzian distribution

$$y(f) = A - \frac{1}{2\pi} \frac{B + C(f - f_0)}{(f - f_0)^2 + D^2} \quad (3.1)$$

where A, B, C, D , and f_0 are the fitting parameters. The term with a C multiple is included to account for the asymmetry of the resonance curves. Figure 3.7 shows the measured $|S_{21}|$ data and the fitted data around the 8.513 GHz resonance at 81 K.

The fitting process was applied to the measured transmission coefficients in the neighborhood of the resonance to give us an expression for the curve, from which the resonant frequency, minimum of $|S_{21}|$, and 3-dB bandwidth can be obtained. The associated Q -factor is defined as $f_r/\Delta f_{3\text{dB}}$, where f_r is the resonant frequency and $\Delta f_{3\text{dB}}$ is the 3-dB bandwidth. Thus, in Figure 3.7, the fitted result (solid curve) gives $f_r=8.5133$ GHz, $\Delta f_{3\text{dB}}=1.36665$ MHz, and $Q=6230$. The process is repeated for measurements at other temperatures. The plot of Q as a function of temperature is shown in Figure 3.8. At 87 K, we observed a

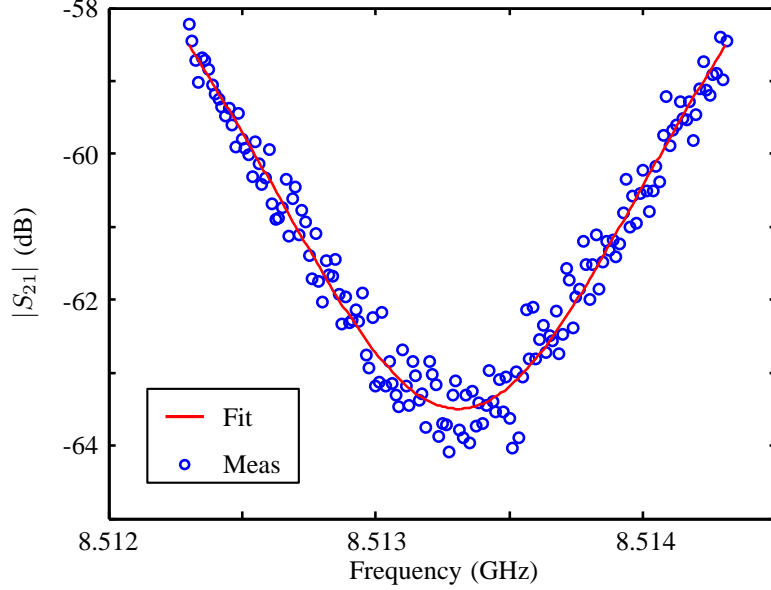


Figure 3.7: The circled points show the measured transmission resonance at 81 K. The solid line is the Lorentzian curve fitted to the data.

peak in Q of around 42000, which has to be estimated from the measured data. This spike in the quality factor is not expected. This unusual frequency response, which is observed on several samples, has not yet been resolved and is proposed as a task for future work. For comparison, a copper SRR on a Rogers TMM10i substrate, which has $\epsilon_r = 9.9$ and $\tan \delta = 0.002$, [49] was fabricated and measured at room temperature. This normal conducting SRR has $Q=220$, which is much lower than that of the HTS SRR when $T < T_c$. It should be mentioned that we are studying the electric resonance rather than the magnetic resonance, which is located at around 3 GHz. Since this is below the waveguide lowest cutoff frequency (6.562 GHz), we machined a planar probe setup for this measurement.

3.4 TEMPERATURE DEPENDENT f_r

The resonant frequency, f_r , of a high temperature superconducting YBCO SRR is dependent on both the ring geometry and temperature when the SRR is cooled below the critical temperature of the superconductor. The split-ring resonator can be modeled by an equivalent LC circuit model, Figure 3.9, where

$$f_r = \frac{1}{2\pi\sqrt{LC}} = \frac{1}{2\pi\sqrt{(L_G + L_K)C}} \quad (3.2)$$

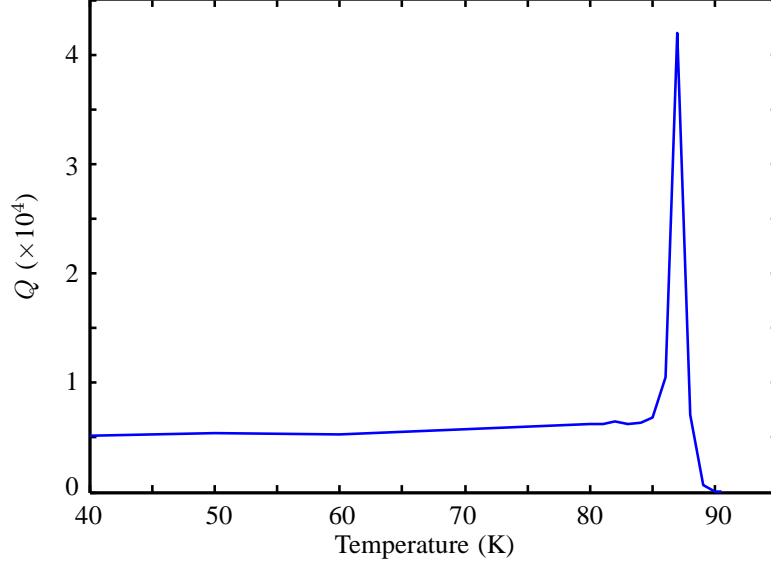


Figure 3.8: Quality factor versus temperature (K) for the measured HTS SRR inside a WR-90 waveguide. It peaks around 42000 at 87 K and saturates around 5200.

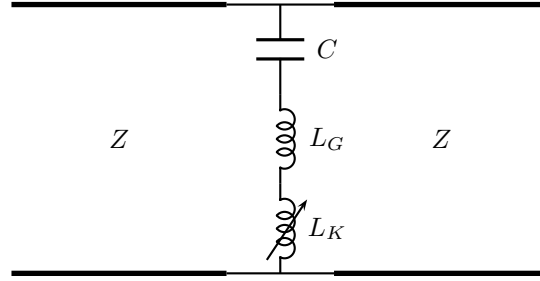


Figure 3.9: Equivalent circuit model of the SRR, where the kinetic inductance L_K is temperature dependent.

The total inductance of a superconducting SRR is a series combination of the geometric inductance (L_G) and the kinetic inductance (L_K). The geometric inductance is temperature independent. Its value can be estimated using the expression from Saha *et al.* [50]

$$L_G = 0.0002l_{av} \left[2.303 \log_{10} \left(\frac{4l_{av}}{w} \right) - 2.853 \right] (\mu\text{H}) \quad (3.3)$$

where, using the dimensions in Figure 3.1, $l_{av} = 4(b - 2w - e) - g$ is the average length of the strip in inches.

We can approximate the SRR with a simple single ring structure that has an effective radius r_m and the same L_G . The inductance of this simplified structure is approximated by [51] as

$$L_G = \frac{12.5\pi r_m}{8 + 11\frac{w}{r_m}} \times 10^{-6} (\text{H}) = \gamma\mu_0 r_m (\text{H}) \quad (3.4)$$

where the effective radius of the ring, r_m , and line width, w , are in meters, and γ is the unit-less transform

multiplier. Equation (3.3) was used to solve for γ and r_m .

The kinetic inductance can be understood by equating the magnetic energy stored in an equivalent inductor, $L_K I^2/2$, to the kinetic energy of the Cooper pairs in a superconductor [52]. The kinetic inductance is a function of the London penetration depth, which depends on temperature, and can be approximated as [53]

$$L_K \approx \mu_0 \frac{l}{w} \lambda \coth \frac{t}{\lambda_L} = \frac{\mu_0 2\pi r_l}{w} \lambda_L \coth \frac{t}{\lambda_L} \quad (3.5)$$

where t is the thickness of the superconducting film, l is the total length of the strip, and λ_L is the temperature dependent penetration depth,

$$\lambda_L(T) = \frac{\lambda_L(0)}{\sqrt{1 - (T/T_c)^2}} \quad (3.6)$$

Brorson *et al.* [54] estimated the absolute penetration depth $\lambda_L(0)=148$ nm and Shi *et al.* [55] found $\lambda(0)=198$ nm for $\text{YBa}_2\text{Cu}_3\text{O}_7$. The value of $\lambda(0)$ depends on the quality and structure of the material and typically lie in the range of 200–400 nm for practical materials. It will be one of the fitting parameters in fitting a theoretical model of the temperature dependence resonant frequency to the measurements.

By assuming the simple LC model in Figure 3.9 for the split-ring resonator, the resonant frequency is given by

$$f_r = \frac{1}{2\pi} \frac{1}{\sqrt{(L_G + L_K)C}} \approx f_G \left\{ 1 + \frac{2\pi r_l \lambda(0)}{\gamma r_m w \sqrt{1 - \left(\frac{T}{T_c}\right)^2}} \coth \left[\frac{t \sqrt{1 - \left(\frac{T}{T_c}\right)^2}}{\lambda(0)} \right] \right\}^{-1/2} \quad (3.7)$$

where f_G is the resonant frequency associated with just the geometric inductance of the SRR. The critical temperature is generally known for the superconductor, but will become a parameter in the fitting process. The absolute penetration depth, $\lambda(0)$, is a second parameter. The resonant frequency f_G is not known exactly and is the third parameter. It should be close to the measured low temperature resonant frequency. This three-parameter function is fitted to the measured data through a nonlinear least square method.

The measured resonant frequency as a function of the temperature for the SRR structure is shown in Figure 3.10 as the red circles. As the temperature drops, the resonant frequency increases until it saturates. The main contribution to this effect is the kinetic inductance of the superconductor, which decreases with

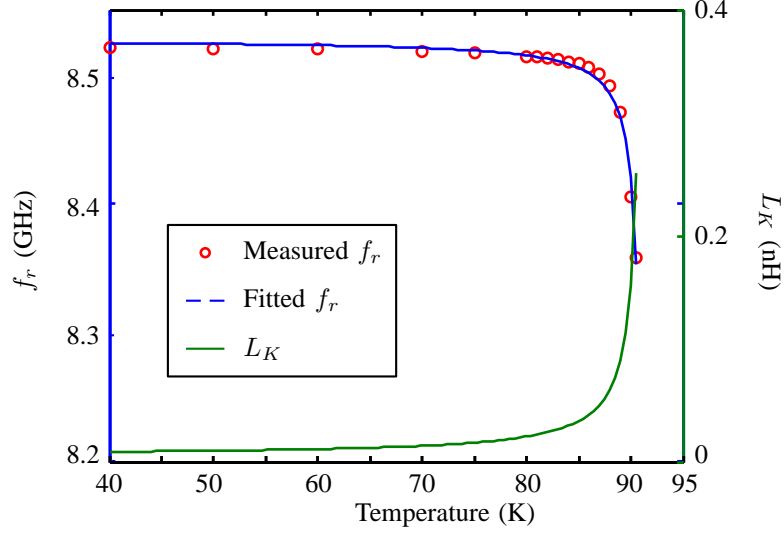


Figure 3.10: Resonant frequency vs temperature. The red circle line and solid blue line represent measured and fitted resonant frequency, respectively. The green solid line is the calculated kinetic inductance extracted from the fitting process.

temperature. The fitting is applied to the measured data and the result is shown as the blue dashed line in Figure 3.10. From the fitted parameters, we can infer the following:

- $T_c=91.3$ K. This value is close to the observed value. Above this temperature, the transmission resonances are not clearly defined.
- $f_G=8.53$ GHz. This is the resonant frequency in the absence of the kinetic inductance. It is in agreement with the measured f_G .
- $\lambda(0)=395$ nm. This is higher than published values of 148 nm [54] and 198 nm [55]. However, it is still within the accepted range. The slight damage of the YBCO film, as can be seen in Figure 3.1, from overexposure in the photolithography process can contribute to this higher value.

Finally, the kinetic inductance versus temperature is shown as the solid green line in Figure 3.10. It shows the expected behavior, that L_K increases with temperature. This also means the total inductance (L_G+L_K) increases and thus lowers the resonant frequency. The kinetic inductance of this structure is very sensitive close to the T_c , and might be used for photon detectors. [56]

3.5 EFFECTIVE CONSTITUTIVE PARAMETER EXTRACTION

Split-ring resonators have been shown to exhibit magnetic resonances accompanied by a negative real permeability. As mentioned earlier, they can also have electric resonances with a negative real permittivity. [35,36] Let us assume that our SRR inside the waveguide can be considered an isotropic and homogeneous material. The effective relative permittivity and permeability are related to the scattering parameters, as discussed by Weir [57], by

$$\Gamma = \frac{S_{11}^2 + 1 - S_{21}^2}{2S_{11}} \pm \sqrt{\left(\frac{S_{11}^2 + 1 - S_{21}^2}{2S_{11}}\right)^2 - 1} \quad (3.8)$$

$$P \equiv e^{-\gamma L} = \frac{S_{21} + S_{11} - \Gamma}{1 - (S_{21} + S_{11})\Gamma} \quad (3.9)$$

$$\frac{1}{\Lambda^2} \equiv \frac{\epsilon_r \mu_r}{\lambda_0^2} - \frac{1}{\lambda_c^2} = - \left[\frac{1}{2\pi L} \ln \left(\frac{1}{P} \right) \right]^2 \quad (3.10)$$

$$\mu_r = \frac{1 + \Gamma}{1 - \Gamma} \frac{1}{\Lambda} \frac{1}{\sqrt{\frac{1}{\lambda_0^2} - \frac{1}{\lambda_c^2}}}, \quad \epsilon_r = \frac{\lambda_0^2}{\mu_r} \left[\frac{1}{\Lambda^2} - \frac{1}{\lambda_c^2} \right] \quad (3.11)$$

where $L = 1$ cm is the effective sample length and λ_c is the waveguide cutoff wavelength of the dominant TE₁₀ mode. The derivations for Γ and P are presented in Appendix B. The retrieved effective μ_r and ϵ_r for the 89 K and 88 K measurements are shown in Figure 3.11. In the neighborhood of the resonance, discussed in Section 3.3, $\text{Re}[\epsilon]$ is negative, which says that these are electric resonances. In addition, although not easily discernible from Figure 3.11, the imaginary parts μ'' and ϵ'' approach zero closer to the resonance as the temperature is lowered. The magnitudes of the imaginary μ and ϵ are also much smaller than those extracted from the room temperature copper SRR on TMM10i measurements.

3.6 CONCLUSION

An array of seven YBCO on MgO split ring resonators was simulated and measured inside a WR-90 waveguide showing a pronounced wide stop band centered around 8 GHz. Furthermore, a single element ring was measured for studying the resonant frequency and quality factor versus temperature. By fitting the behavior of the resonant frequency to an expression that relates it to the London penetration depth, kinetic inductance,

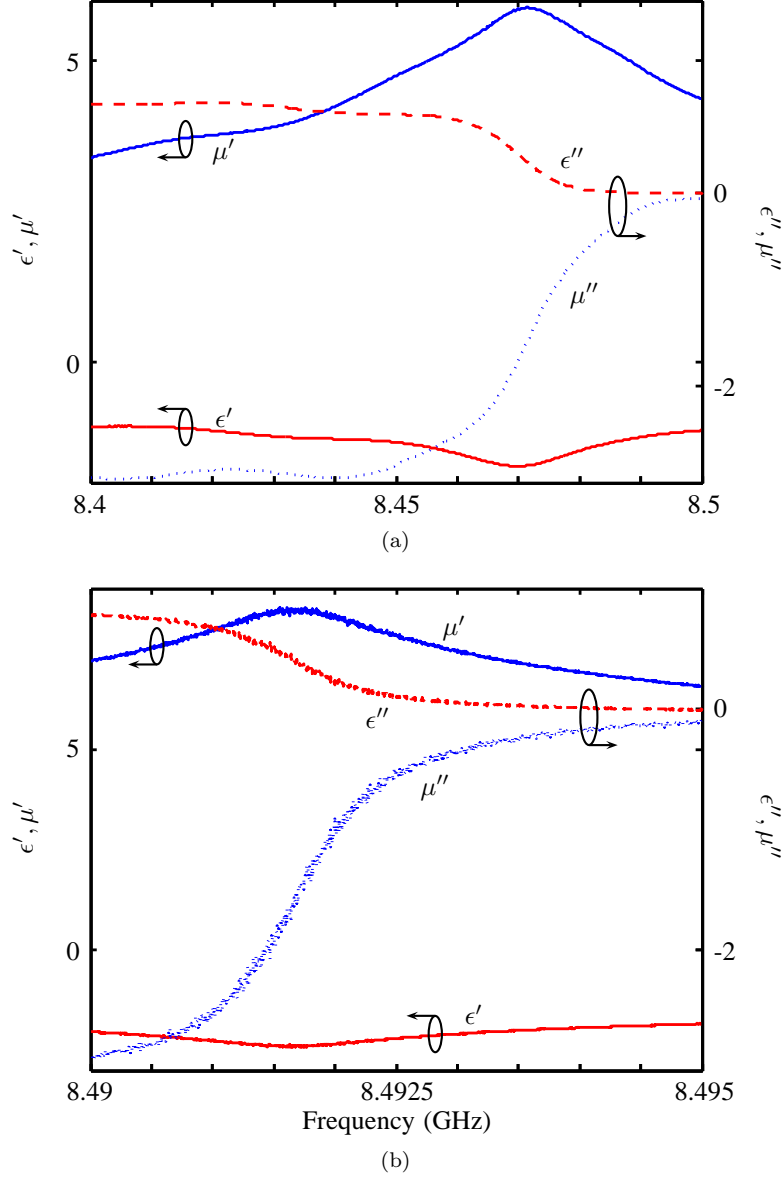


Figure 3.11: The extracted relative permittivity and permeability at (a) 89 K and (b) 88 K.

and critical temperature, we can infer their values. The fitted T_c of 91.3 K and f_r of 8.53 GHz are close to the observed values. The inferred $\lambda(0)$ of 395 nm is higher than the values given by Brorson and Shi, but still within the accepted range. This can be attributed to the slight damaging of the YBCO film due to overexposure during the photolithography process. The kinetic inductance was shown to saturate at low temperature and vary greatly close to the T_c . The quality factor, saturating at >5000 , of these HTS SRRs was shown to be much higher than the normal conductor samples. A peak of $Q \approx 42000$ was observed around 87 K. Finally, we have shown that these HTS SRRs have electric resonances and exhibit a negative effective

permittivity in the neighborhood of the resonance.

CHAPTER 4

EFFECTIVE CONSTITUTIVE PARAMETERS OF HTS SRR

CONTENTS

4.1	Introduction	43
4.2	Extraction Method	45
4.3	Validation of Extraction Method	50
4.4	HTS SRR Specifications and Measurement Setup	54
4.5	Experimental Results	58
4.6	Comparison to Simulations	63
4.7	Discussion	66

4.1 INTRODUCTION

There have been many proposed methods for characterizing the effective constitutive parameters of split-ring resonator arrays, with a purpose of demonstrating the existence of an effective negative permeability over some frequency band. For example, in [19, 26–29], the plane wave normal incidence approach was discussed for retrieving the effective parameters; [30] presented an optimization technique; and in [31] a waveguide

approach for retrieving the anisotropic parameters was presented. Applications that take advantage of the effective near-zero and negative permeability property of SRRs include negative index materials [32, 58] and electromagnetic cloaks. [4, 5] The circuits in these studies use normal metal and exhibit loss that can be reduced by using superconductors. In this chapter, we present the extracted effective relative permittivity and permeability of high-temperature superconducting (HTS) SRR arrays using the waveguide method, which is well suited to our experimental study of the effective permittivity and permeability tensors of HTS SRR arrays. The waveguide setup is confined to a small space, which can be cooled easily to sub- T_C as demonstrated in Chapter 3 and [42]. Other studies on superconducting metamaterials have been presented by Ricci *et al.* [37–39] and Chen *et al.*, [40] but the quantitative effective constitutive parameters were not discussed. In [42] the relative effective permittivity and permeability of HTS YBCO SRRs are extracted by assuming homogeneous and isotropic bulk properties.

This chapter presents the extracted effective relative permittivity and permeability of YBCO split-ring resonator arrays deposited on a magnesium oxide (MgO) substrate. The dimensions of the SRR structure are chosen such that the magnetic plasma frequency, defined as the frequency where the real part of the effective permeability equals zero, falls in the X-band region. The arrays are measured inside a WR-90 X-band rectangular waveguide at liquid nitrogen (LN₂) temperature. YBCO has a critical temperature of ≈ 88 K [59], which is above the boiling temperature of LN₂ (≈ 75.68 K at 1655 m elevation in Boulder, CO). The free space wavelength at 10 GHz is greater than ten times the SRR array spacial period and thus the array can be thought of as having an averaged response and can be characterized by an equivalent homogeneous material with effective relative permittivity and permeability at a macroscopic level. It will be shown that in the frequency band where the real part of the relative permeability μ' is negative, the imaginary part μ'' quickly drops to near zero, a property not observed with room temperature normal conducting SRR arrays. The effective parameters extracted from the scattering (S) parameters treat the SRR array as a homogeneous, anisotropic medium described by the biaxial relative permittivity and permeability diagonal tensors $\bar{\bar{\epsilon}}_r = \text{diag}[\epsilon_1, \epsilon_2, \epsilon_3]$ and $\bar{\bar{\mu}}_r = \text{diag}[\mu_1, \mu_2, \mu_3]$, respectively, with $\epsilon = \epsilon' - j\epsilon''$, $\mu = \mu' - j\mu''$, and $n = n' - jn''$. The time convention followed in this study is $e^{j\omega t}$.

The layout of the chapter is as followed. A derivation of the waveguide extraction formulae used to

calculate the tensor elements from the measured and simulated S parameters will first be presented. For validation, a set of SRR arrays made of copper on Rogers 3010 substrate is placed inside the waveguide with two orthogonal orientations and the respective scattering parameters recorded. Measurements from the two orientations allow for retrieving three of the six tensor elements, μ_1 , ϵ_2 , and μ_3 . The other three elements can be retrieved in a similar manner by measuring the samples with two different orientations, discussed in the next section and [31], but they are not needed for our experiments and were therefore not calculated. The retrieved parameters are then compared with those from the waveguide and free space full-wave simulations of identical SRR arrays. Next a set of HTS SRR arrays were fabricated and measured. The results are compared with those from room temperature copper SRR measurements. Finally, we briefly discuss the additional high Q -factor resonances, accompanying the main resonances, that are only seen in the cryogenic measurement and simulations of low-loss samples.

4.2 EXTRACTION METHOD

Consider the scenario of a homogeneous slab of anisotropic material, defined by the relative permittivity and permeability diagonal tensors

$$\bar{\bar{\epsilon}} = \epsilon_0 \begin{bmatrix} \epsilon_1 & 0 & 0 \\ 0 & \epsilon_2 & 0 \\ 0 & 0 & \epsilon_3 \end{bmatrix} \quad \bar{\bar{\mu}} = \mu_0 \begin{bmatrix} \mu_1 & 0 & 0 \\ 0 & \mu_2 & 0 \\ 0 & 0 & \mu_3 \end{bmatrix} \quad (4.1)$$

Four measurements inside a rectangular waveguide are needed to determine all the diagonal terms. Figure 4.1 shows how the sample needs to be arranged inside the waveguide for the four measurements, referred to as orientations I, II, III, and IV. For determining μ_1 , μ_3 , and ϵ_2 , which are the terms we are interested in for the metamaterial radome, the sample is inserted into a rectangular waveguide with two different orientations as shown in Figures 4.2a and 4.2b. The first case in which the material axes 1, 2, and 3 are in the x , y , and z axes, respectively, will be referred to as orientation I. The second case in which the material axes 1, 2, and 3 point along the z , y , and x axes will be referred to as orientation II.

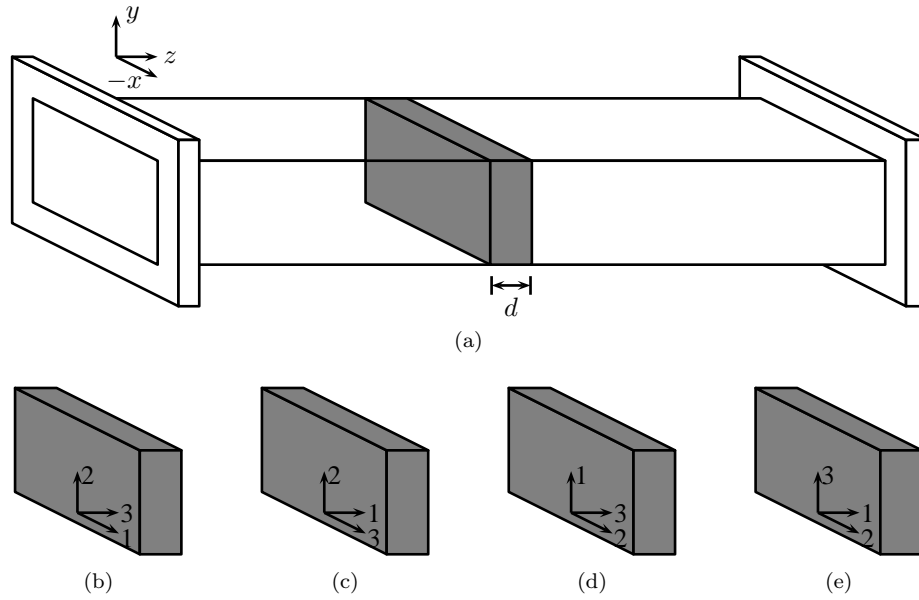


Figure 4.1: (a) The slab of anisotropic material is placed inside a rectangular waveguide for characterizing the effective permittivity and permeability. (b)-(d) The orientations (I, II, III, and IV, respectively) of how the material is inserted into the waveguide.

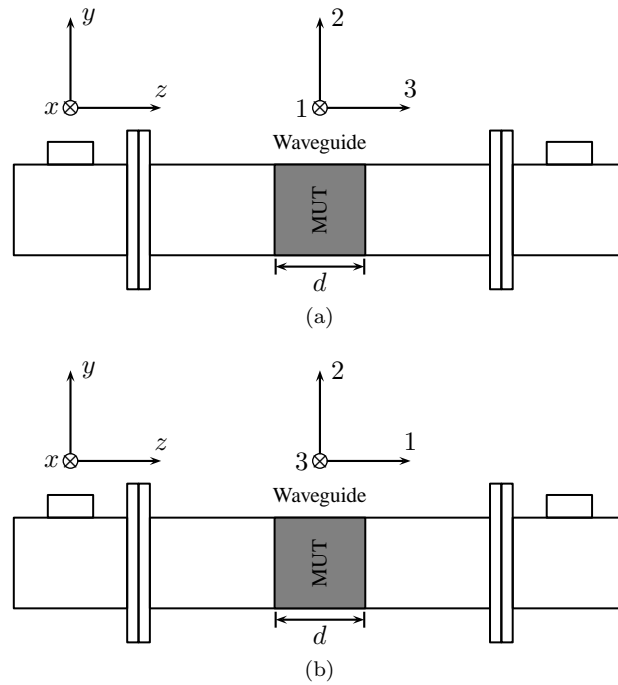


Figure 4.2: The material under test (MUT) placed inside a rectangular waveguide with (a) orientation I and (b) orientation II, for retrieval of μ_1 , μ_3 , and ϵ_2 .

We begin the extraction analysis from Maxwell's equation

$$\nabla \times \mathbf{H} = j\omega\bar{\epsilon} \cdot \mathbf{E} \quad (4.2)$$

$$\nabla \times \mathbf{E} = -j\omega\bar{\mu} \cdot \mathbf{H} \quad (4.3)$$

First consider the case where the material under test (MUT) is placed with orientation I into the rectangular waveguide with a dominant TE₁₀ excitation. The only non-zero field components are thus E_y , H_x , and H_z .

Expanding Equations (4.2) and (4.3) and keeping only these terms results in

$$\begin{aligned} \nabla \times \mathbf{H} &= \frac{\partial H_z}{\partial y} \mathbf{u}_x + \left(\frac{\partial H_x}{\partial z} - \frac{\partial H_z}{\partial x} \right) \mathbf{u}_y - \frac{\partial H_x}{\partial y} \mathbf{u}_z \\ &= j\omega\epsilon_2\epsilon_0 E_y \mathbf{u}_y \end{aligned} \quad (4.4)$$

$$\begin{aligned} \nabla \times \mathbf{E} &= -\frac{\partial E_y}{\partial z} \mathbf{u}_x + \frac{\partial E_y}{\partial x} \mathbf{u}_z \\ &= -j\omega\mu_1\mu_0 H_x \mathbf{u}_x - j\omega\mu_3\mu_0 H_z \mathbf{u}_z \end{aligned} \quad (4.5)$$

$$\begin{aligned} E_y &= \frac{1}{j\omega\epsilon_2\epsilon_0} \left(\frac{\partial H_x}{\partial z} - \frac{\partial H_z}{\partial x} \right) \\ &= \frac{1}{j\omega\epsilon_2\epsilon_0} \left(\frac{1}{j\omega\mu_1\mu_0} \frac{\partial^2 E_y}{\partial z^2} + \frac{1}{j\omega\mu_3\mu_0} \frac{\partial^2 E_y}{\partial x^2} \right) \\ &= \frac{-1}{k_0^2} \left(\frac{1}{\mu_1\epsilon_2} \frac{\partial^2 E_y}{\partial z^2} + \frac{1}{\mu_3\epsilon_2} \frac{\partial^2 E_y}{\partial x^2} \right) \end{aligned} \quad (4.6)$$

where $k_0 = \omega\sqrt{\mu_0\epsilon_0}$ is the free-space wavenumber. For $E(x, y, z) = E(x, y)e^{-jk_z z}$, Equation (4.6) becomes

$$\frac{\partial^2 E_y}{\partial x^2} + \frac{\mu_3}{\mu_1} (k_0^2 \mu_1 \epsilon_2 - k_z^2) E_y = 0 \quad (4.7)$$

Solving the differential equation and applying the boundary conditions gives us

$$E_y = E_0 \sin(k_x x) e^{-jk_z z} \quad (4.8)$$

where

$$k_x^2 = \left(\frac{\pi}{a} \right)^2 = \frac{\mu_3}{\mu_1} (k_0^2 \mu_1 \epsilon_2 - k_z^2) \quad (4.9)$$

is the square of the waveguide cutoff wave number of the dominant TE₁₀ mode and a is the width of the waveguide. The refractive index is obtained from k_z by

$$n_I = \frac{k_z}{k_{0z}} = \frac{\sqrt{k_0^2 \mu_1 \epsilon_2 - k_x^2 \frac{\mu_1}{\mu_3}}}{\sqrt{k_0^2 - k_x^2}} \quad (4.10)$$

where k_{0z} is the wave number along the propagation direction inside a empty waveguide and the subscript I denoting the results from orientation I of the sample. The wave impedance for the TE modes is given by

$$\zeta_{TE} = -\frac{E_y}{H_x} = \frac{\omega\mu_1\mu_0}{k_z} = \frac{\omega\mu_0}{k_{0z}} \frac{\mu_1}{n_I} = \zeta_0 \frac{\mu_1}{n_I} \quad (4.11)$$

where ζ_0 is the TE wave impedance for an empty rectangular waveguide. When normalizing to ζ_0 , we have

$$\zeta_I = \frac{\mu_1}{n_I} = \mu_1 \frac{\sqrt{k_0^2 - k_x^2}}{\sqrt{k_0^2\mu_1\epsilon_2 - k_x^2\frac{\mu_1}{\mu_3}}} \quad (4.12)$$

where ζ_I is the normalized wave impedance for orientation I.

Next, n_{II} and ζ_{II} are solved for the case shown in Figure 4.2b, where the placement of the biaxial sample inside the waveguide is rotated such that 1, 2, and 3 now each points along the z , y , and x axis, respectively.

Following the same procedure, we obtain

$$n_{II} = \frac{k_z}{k_{0z}} = \frac{\sqrt{k_0^2\mu_3\epsilon_2 - k_x^2\frac{\mu_3}{\mu_1}}}{\sqrt{k_0^2 - k_x^2}} \quad (4.13)$$

$$\zeta_{II} = \frac{\mu_3}{n_{II}} = \mu_3 \frac{\sqrt{k_0^2 - k_x^2}}{\sqrt{k_0^2\mu_3\epsilon_2 - k_x^2\frac{\mu_3}{\mu_1}}} \quad (4.14)$$

where ζ_{II} is the normalized wave impedance for orientation II.

By taking two sets of measurements from two different orientations (I and II) in which the biaxial material is placed inside the waveguide, the tensor elements μ_1 , ϵ_2 , and μ_3 can be retrieved using the following equations

$$\mu_1 = n_I \zeta_I \quad (4.15)$$

$$\mu_3 = n_{II} \zeta_{II} \quad (4.16)$$

$$\epsilon_{2(I)} = \frac{n_I^2 k_{0z}^2 + k_x^2 \frac{\mu_1}{\mu_3}}{k_0^2 \mu_1} \quad (4.17)$$

$$\epsilon_{2(II)} = \frac{n_{II}^2 k_{0z}^2 + k_x^2 \frac{\mu_3}{\mu_1}}{k_0^2 \mu_3} \quad (4.18)$$

For completeness, the extraction of ϵ_1 , μ_2 , and ϵ_3 is briefly discussed. They require the sample to be inserted into the waveguide with orientations shown in Figure 4.3. Following the procedure discussed gives us

$$n_{III} = \frac{k_z}{k_{0z}} = \frac{\sqrt{k_0^2\mu_2\epsilon_1 - k_x^2\frac{\mu_2}{\mu_3}}}{\sqrt{k_0^2 - k_x^2}} \quad \text{and} \quad n_{IV} = \frac{k_z}{k_{0z}} = \frac{\sqrt{k_0^2\mu_2\epsilon_3 - k_x^2\frac{\mu_2}{\mu_1}}}{\sqrt{k_0^2 - k_x^2}} \quad (4.19)$$

$$\zeta_{III} = \mu_2 \frac{\sqrt{k_0^2 - k_x^2}}{\sqrt{k_0^2\mu_2\epsilon_1 - k_x^2\frac{\mu_2}{\mu_3}}} \quad \text{and} \quad \zeta_{IV} = \mu_2 \frac{\sqrt{k_0^2 - k_x^2}}{\sqrt{k_0^2\mu_2\epsilon_3 - k_x^2\frac{\mu_2}{\mu_1}}} \quad (4.20)$$

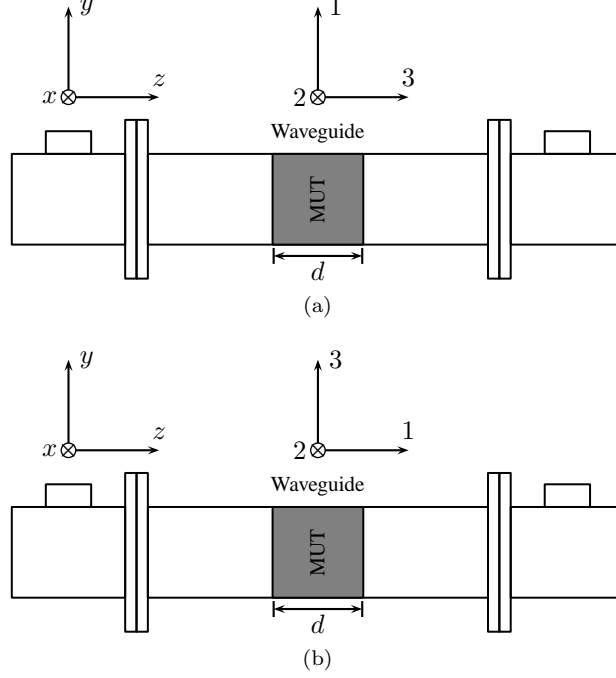


Figure 4.3: The material under test placed inside a rectangular waveguide with (a) orientation III and (b) orientation IV, for the retrieval of ϵ_1 , ϵ_3 , and μ_2 .

$$\mu_{2(\text{III})} = n_{\text{III}}\zeta_{\text{III}} \quad \text{or} \quad \mu_{2(\text{IV})} = n_{\text{IV}}\zeta_{\text{IV}} \quad (4.21)$$

$$\epsilon_1 = \frac{n_{\text{III}}^2 k_{0z}^2 + k_x^2 \frac{\mu_2}{\mu_3}}{k_0^2 \mu_2} \quad \text{and} \quad \epsilon_3 = \frac{n_{\text{IV}}^2 k_{0z}^2 + k_x^2 \frac{\mu_2}{\mu_1}}{k_0^2 \mu_2} \quad (4.22)$$

Finally, the index of refraction, n , and wave impedance ζ , normalized to $\zeta_0 = \omega\mu_0/k_{0z}$, are related to the scattering parameters, as derived in Appendix B, by the expressions

$$\Gamma = \frac{S_{11}^2 + 1 - S_{21}^2}{2S_{11}} \pm \sqrt{\left(\frac{S_{11}^2 + 1 - S_{21}^2}{2S_{11}}\right)^2 - 1} \quad (4.23)$$

$$P \equiv e^{-jk_{0z}nd} = \frac{S_{21} + S_{11} - \Gamma}{1 - (S_{21} + S_{11})\Gamma} \quad (4.24)$$

$$\zeta = \left(\frac{1 + \Gamma}{1 - \Gamma}\right) \quad (4.25)$$

$$n = \frac{1}{k_{0z}d} \left(\text{Im} \left[\ln \frac{1}{P} \right] + 2\pi m \right) - \frac{j}{k_{0z}d} \text{Re} \left[\ln \frac{1}{P} \right] \quad (4.26)$$

where d is the length of the sample. Note that Γ is the reflection coefficient at the air-sample boundary if the sample extends semi-infinitely in the propagation direction. The sign in Equation (4.23) is chosen such that $|\Gamma| \leq 1$. The real part of n has an ambiguity of $2\pi m$, where m is chosen so that n is a continuous function.

4.3 VALIDATION OF EXTRACTION METHOD

To validate the extraction method, a homogeneous, anisotropic slab of material with the following relative permittivity and permeability is placed inside a WR-90 waveguide in the HFSS simulation:

$$\epsilon_1 = 1, \quad \epsilon_2 = 1 - \frac{1.1}{(f/10.6)^2 - j0.003f - 1}, \quad \epsilon_3 = 1 \quad (4.27)$$

$$\mu_1 = 1 - \frac{1}{(f/11.5)^2 - j0.009f - 1}, \quad \mu_2 = 1, \quad \mu_3 = 1 - \frac{1}{(f/9.2)^2 - j0.009f - 1} \quad (4.28)$$

where f is the frequency. These values were chosen to demonstrate that the method works for dispersive materials and also because they resemble values that are seen for wire and SRR metamaterials. The waveguide is excited with a dominant TE₁₀ mode. For this test, only orientations I and II are studied for extracting ϵ_2 , μ_1 , and μ_3 . The retrieved parameters are plotted together with the analytical values in Figure 4.4, which show the two sets of values are in agreement with each other for both the real and imaginary parts. This method was also applied to a simple sapphire model: $\epsilon_1 = \epsilon_2 = 9.4$, $\epsilon_3 = 11.6$, and $\mu_1 = \mu_2 = \mu_3 = 1$. The extracted results agree with the modeled values.

Before fabricating the HTS SRRs and extracting their effective material parameters, a set of SRR arrays made of copper on Rogers 3010 substrate was etched for testing. Each SRR made of a 35- μm thick copper split-ring on a 635- μm thick Rogers 3010 substrate. The datasheet from Rogers [60] specified $\epsilon_r = 10.2 \pm 0.3$ with a loss tangent of 0.0022. From simulations with several ϵ_r values, it was seen that using $\epsilon_r = 10.5$ results in the best fit between the simulations and measurements. The relevant dimensions are shown in Figure 4.5. At 10 GHz, the free space wavelength, $\lambda_0=30$ mm, is greater than ten times the unit cell dimension, 2.5 mm.

First, arrays of the SRRs are placed inside a WR-90 rectangular waveguide in the HFSS simulations, with orientations I and II shown in Figures 4.6a and 4.6b. In orientation I, the elements are placed such that the distance from center of one array element is 2.5 mm from the neighboring array element. Perfect electric walls are used for the waveguide walls. The simulated S -parameters are then deembedded to the material reference planes and used to extract the ϵ_2 , μ_1 , and μ_3 . Their values are shown as the solid and dashed red curves in Figure 4.7.

Free-space models of the SRR with orientations I and II were also created in separate HFSS simulations, shown in Figure 4.8. Perfect electric (PEC) and magnetic (PMC) walls are assigned at the transverse

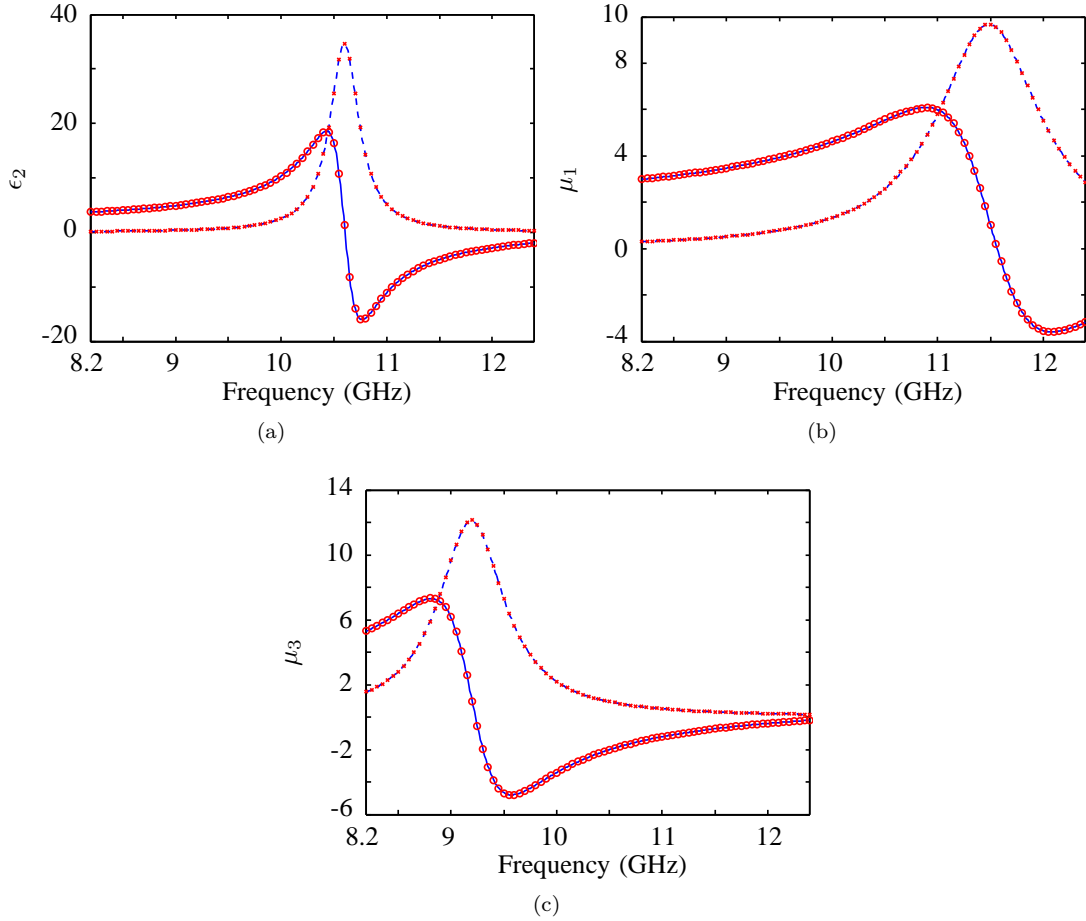


Figure 4.4: The retrieved effective material parameters, from the simulated S parameters, for the homogeneous slab with properties defined by Equations (4.27) and (4.28). The solid and dashed blue lines represent the real ('') and imaginary ('') parts, respectively, of the analytical values for (a) ϵ_2 , (b) μ_1 , and (c) μ_3 . The red 'O' and 'X' symbols represent the extracted values from the waveguide simulations.

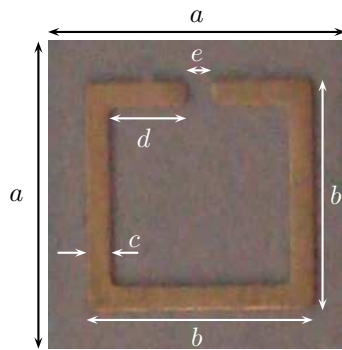


Figure 4.5: Photograph of a copper SRR on Rogers 3010 substrate with $a=2.5$ mm, $b=1.9$ mm, $c=0.2$ mm, $d=0.65$ mm, and $e=0.2$ mm.

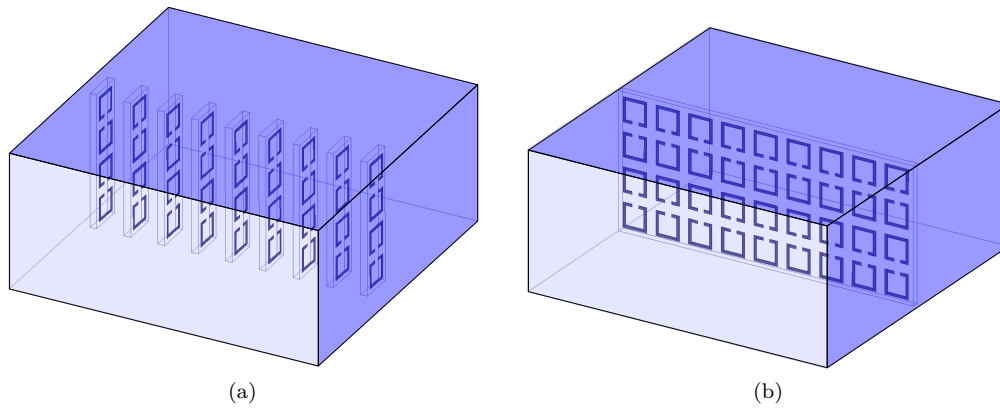


Figure 4.6: SRR arrays placed inside a WR-90 rectangular waveguide with orientation (a) I and (b) II.

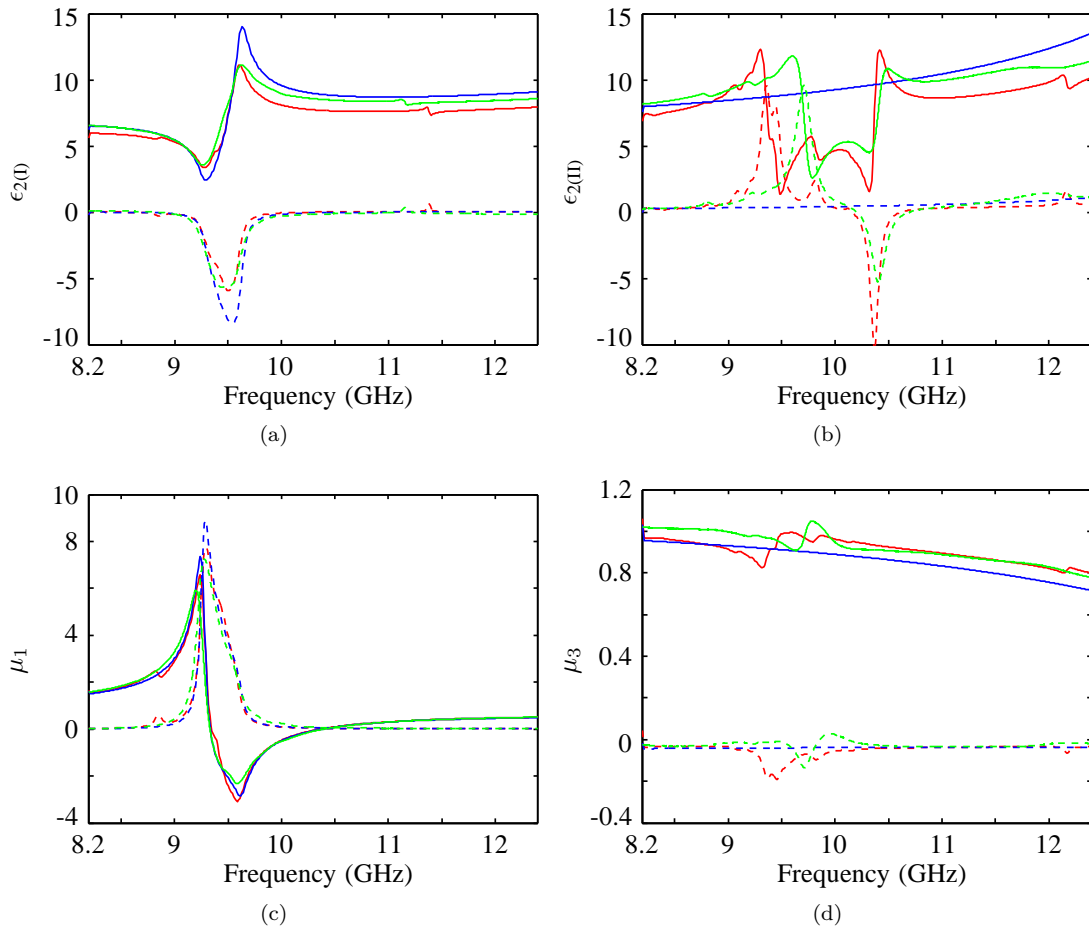


Figure 4.7: Extracted effective parameters for the copper on Rogers 3010 SRR arrays. The red, blue, and green curves represent results from waveguide simulations, free space simulations, and waveguide measurements, respectively. The solid and dashed curves represent the real ($'$) and imaginary ($''$) parts of the parameters.

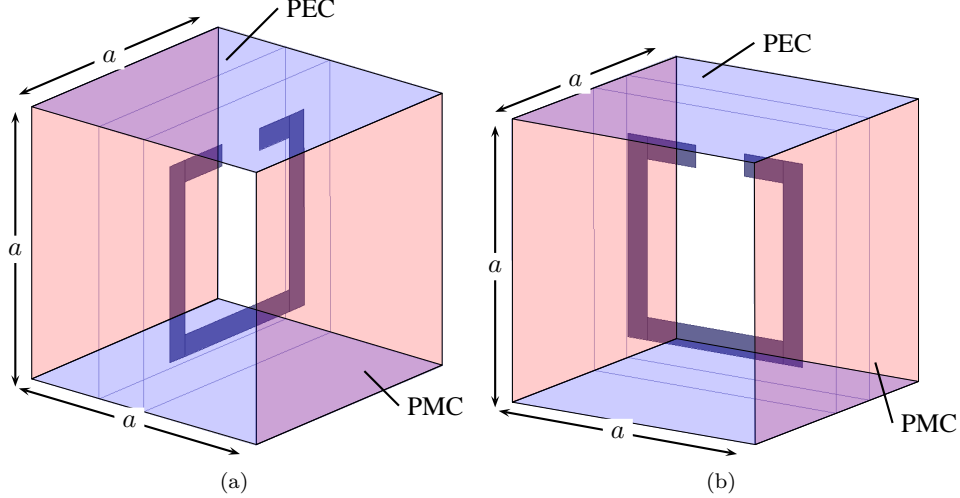


Figure 4.8: Free space models of the SRR for orientations (a) I and (b) II. The period a is 2.5 mm

boundaries to define the directions of the electric and magnetic fields and to emulate a uniform plane wave incident on the SRR sample. For the free space orientation I, the E- and H-field vectors are parallel to material axes 2 and 1, respectively. For the free space orientation II, the E- and H-field vectors are parallel to material axes 2 and 3, respectively. In addition, the electric walls mirror the SRRs in the vertical direction to match the alternating arrangement of the SRR arrays.

A set of scattering parameters is obtained for each of the orientations, from which the effective constitutive parameters are retrieved using the free space extraction method discussed in [57, 61] and Appendix B. The model with which the SRR array is aligned with orientation I allows for the extraction of μ_1 and $\epsilon_{2(I)}$, whereas orientation II allows for the extraction of $\epsilon_{2(II)}$ and μ_3 . These results are shown in Figure 4.7, as blue solid and dashed curves.

The copper SRR arrays are fabricated by chemical etching, and individual arrays were cut with a laser for precision. The surface of the conductor was finished with a 48 nm thick gold film layer. Using an in-house PCB milling machine (ProtoMat S62), deep grooves were milled on a Rohacell 51 IG foam to be used as sample holders for the $2.5 \text{ mm} \times 10 \text{ mm}$ structures, ensuring equal separation between the samples. The Rohacell foam has a relative permittivity of 1.07 and a loss tangent of 0.0021 at 10 GHz, which is very close to the electromagnetic properties of air ($\epsilon_r = 1$). The SRR samples with the foam (orientation I) and without the foam (orientation II) are then placed inside a WR-90 waveguide for measurement, Figures 4.9a and 4.9b,

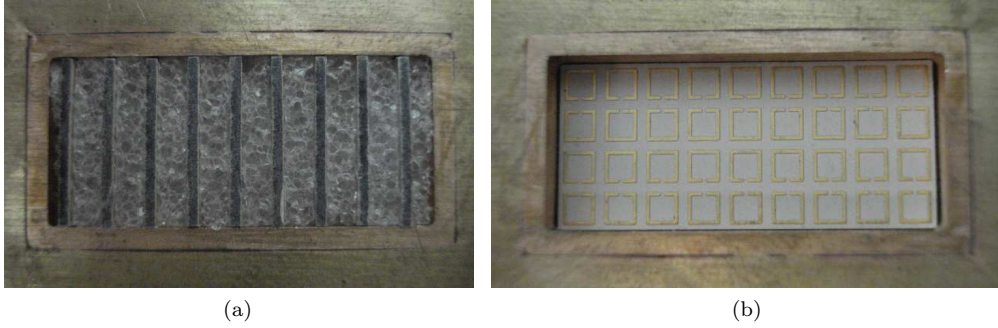


Figure 4.9: Fabricated SRR on a Rogers 3010 substrate aligned inside a WR-90 waveguide with orientations (a) I and (b) II for measurements. Refer to Figure 4.6 for a clearer image of orientation I placement.

respectively.

In the measurement, the waveguide Thru-Reflect-Line (TRL) calibration was performed up to the end of the coaxial-to-waveguide adapters, where the Reflect standard is a “Short.” Software deembedding was performed as a post-processing of the data. The simulated and corrected S -parameters are shown in Figure 4.10 for comparison. The corrected measured S -parameters are used to extract the effective parameters, which are plotted together with the simulations as the green solid and dashed curves in Figure 4.7. The results agree with the waveguide simulations. The obvious disagreements from the free space results can be seen in the μ_3 and $\epsilon_{2(\text{II})}$ curves. A reason for this is that the magnetic fields are present in both transverse and longitudinal directions inside the waveguide. They result in resonant behavior in both orientations and give rise to the resonant feature seen in the waveguide μ_3 and $\epsilon_{2(\text{II})}$, but not in the free space μ_3 and $\epsilon_{2(\text{II})}$. The anti-resonant behavior in $\epsilon_{2(\text{II})}$ around 10.5 GHz is a result from dividing by a near-zero μ_1 in Equation (4.18).

4.4 HTS SRR SPECIFICATIONS AND MEASUREMENT SETUP

Next, a set of YBCO SRR arrays were fabricated for the cryogenic characterization of the effective parameters. Each SRR is made of a 700-nm thick YBCO split-ring resonator deposited on a 500- μm thick MgO substrate, which has a nominal relative permittivity of 9.7 and a 77 K electric loss tangent of 5×10^{-6} at 10.48 GHz. [62] The relevant dimensions are shown in Figure 4.11. A single contact mask was used for patterning the SRR arrays on a square YBCO on MgO wafer shown in Figure 4.12. After etching, the wafer was diced along the cutting markers into 4×1 and 4×9 samples, of dimensions $10 \times 2.5 \text{ mm}^2$ and $10 \times 22.5 \text{ mm}^2$, respectively.

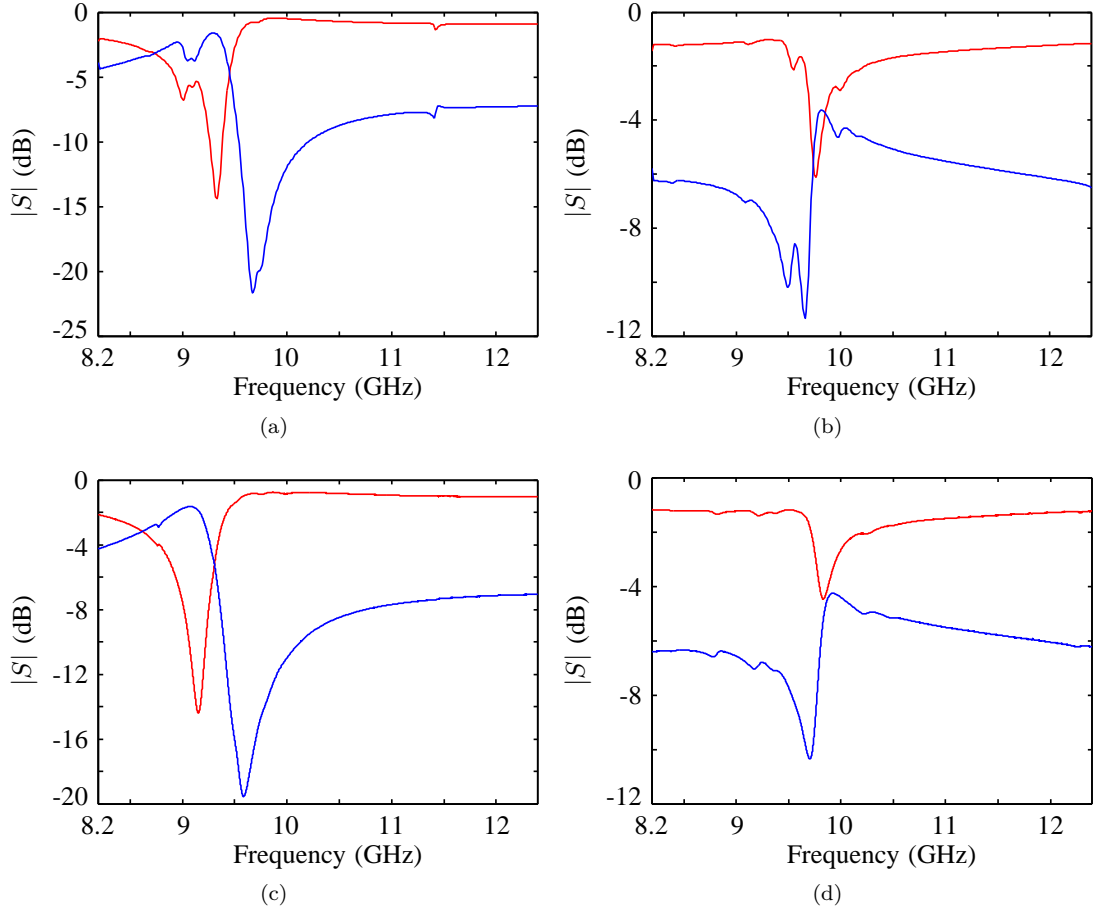


Figure 4.10: Simulated and measured magnitude of the transmission and reflection coefficients of the copper SRR arrays. The red and blue curves are the S_{11} and S_{21} , respectively. (a) and (b) are the simulations for orientations I and II, respectively. (c) and (d) are the measurements for orientations I and II, respectively.

However, the smallest available blade for cutting MgO is an 8 mils ($\approx 200 \mu\text{m}$) resinoid blade. Thus, the diced 4×1 and 4×9 samples are slightly smaller and have averaged dimensions $9.95 \times 2.35 \text{ mm}^2$ and $22.35 \times 10 \text{ mm}^2$, respectively. This slight deviation in dimensions has negligible effect on our results, the S_{21} resonance shifted by less than 1%.

A waveguide Thru-Reflect-Line (TRL) calibration was performed on an Agilent 8722ES vector network analyzer (VNA) at LN_2 temperature ($\approx 76 \text{ K}$) to set the calibrated reference planes to the end of the waveguide adapters. A flat aluminum plate was used for the reflect standard, while a 13.86 mm waveguide section was the LINE standard. The THRU standard refers to a zero length section, which means a direct connection of the two waveguide adapters. By performing the calibration at low temperature, we take into account the enhanced electrical conductivity of the metallic waveguide structures. Figure 4.13 shows a sketch of the

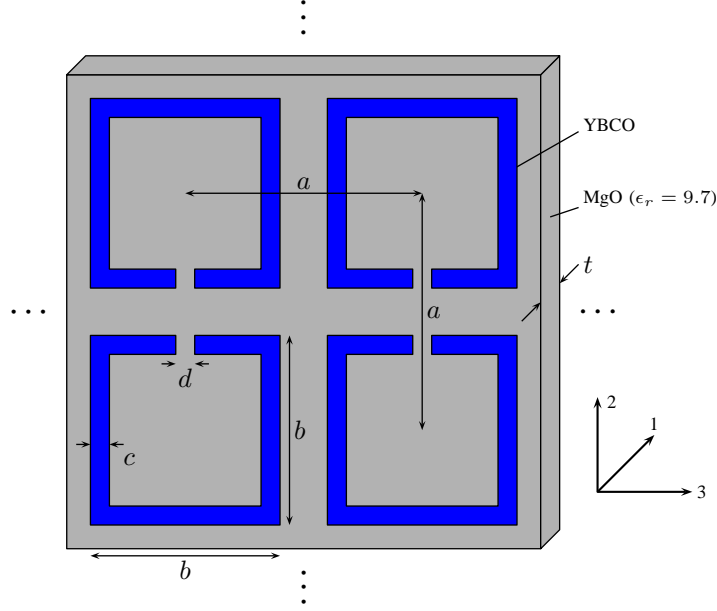


Figure 4.11: Sketch of an experimental X-band YBCO SRR array deposited on a MgO substrate with $a=2.5$ mm, $b=2$ mm, $c=0.2$ mm, $d=0.2$ mm, and $t=0.5$ mm. The material axes 1, 2, and 3 correspond with the tensor elements $\bar{\epsilon}$ and $\bar{\mu}$.

measurement setup. We note that the calibration reference planes and material reference planes are different. Thus, the measured S parameters of the samples have to be further deembedded by post-processing the measured calibrated data.

For the cold calibration, the waveguide parts (adapters and TRL standards) were submerged into a LN_2 bath. A short period of time is allowed to elapse to ensure the whole structure is cooled uniformly to 76 K before the standard is measured. An indication of this is when the liquid nitrogen around the structure stops boiling. A problem with this method of cooling is during the cooling process, a small amount of liquid nitrogen seeps into the waveguide parts and alters the measured phase of the THRU and LINE standards, relative to the empty standards. This is because LN_2 has a higher permittivity (1.538 [63]) than air. The measured phase of the LINE standard is shown as the dotted blue curve in Figure 4.14. As a first attempt to keep the LN_2 out of the waveguide parts, vacuum grease was applied to the seams where the waveguide parts come together, since the grease would freeze and work as a barrier. A second attempt was placing indium foils between the waveguide parts. Indium is a soft metal and, when pressed between two waveguide parts, would seal the small gaps resulting from the surface roughness of the waveguide parts. However, in both attempts, some liquid nitrogen managed to leak in. The measured phase of the LINE standard for the vacuum grease

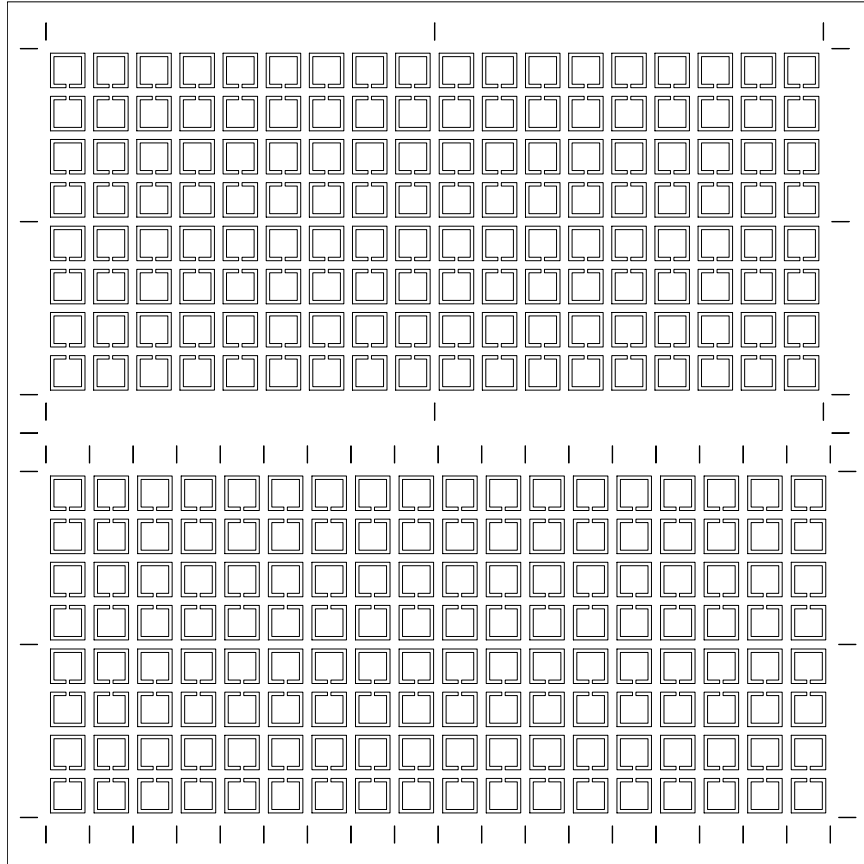


Figure 4.12: $50 \times 50 \text{ mm}^2$ YBCO on MgO wafer layout of the 4×1 and 4×9 SRR arrays. $25 \mu\text{m}$ wide dicing markers were included to assist with the dicing process.

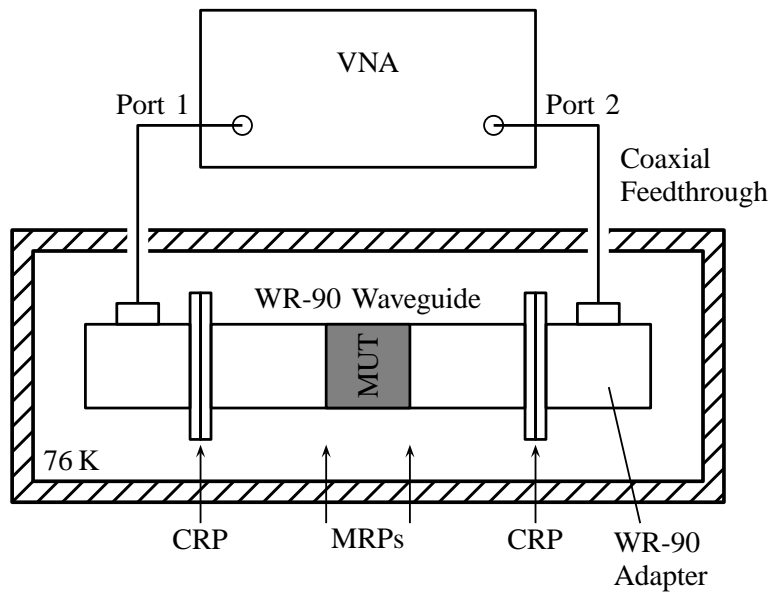


Figure 4.13: Measurement setup showing the calibrated reference planes (CRPs) and the material under test (MUT) reference planes (MRPs). The portion inside the hashed box is cooled to $\approx 76 \text{ K}$. The arrows indicate the locations for the calibration and material reference planes.

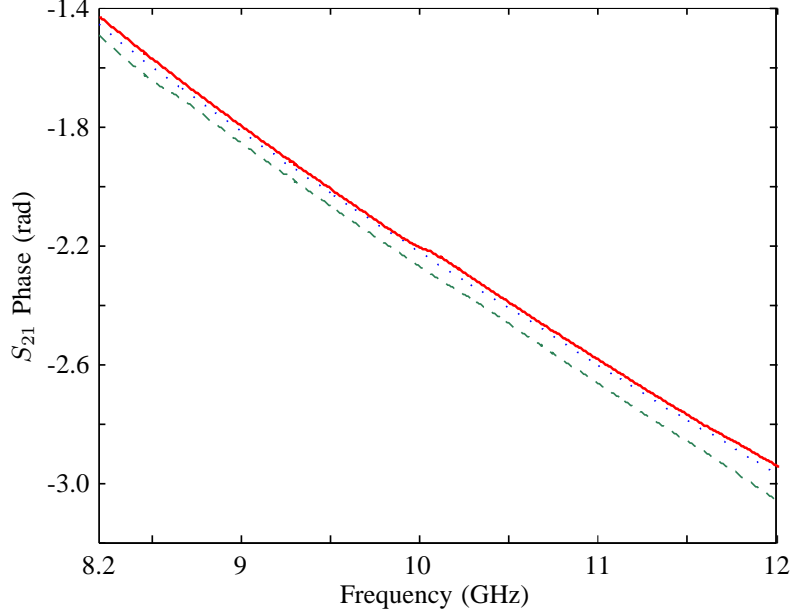


Figure 4.14: The phase of S_{21} of the TRL LINE standard: the dotted blue curve for the case where no vacuum grease was used; the dashed green curve for the case where vacuum grease was used; and the solid red curve for the case of indirect cooling.

method is shown as the dashed green curve in Figure 4.14.

Finally, an indirect cooling method is used. For each measurement, the whole waveguide structure is wrapped with aluminum foil to prevent LN_2 from seeping into the waveguide components and then placed into a LN_2 bath. A Lakeshore temperature sensor is attached to the coaxial-waveguide adapter. The whole calibration process took over two hours. This method of cooling is used for measuring the SRR samples. The phase of S_{21} of the LINE standard measurement from this method is shown as the solid red curve in Figure 4.14. Although the difference is small, the measurements with the poor calibrations and measurements (direct cooling with LN_2) show incorrect extracted values, e.g. μ_3 shown in Figure 4.15.

4.5 EXPERIMENTAL RESULTS

Arrays of the HTS SRRs are placed inside an X-band rectangular waveguide, with orientations I and II shown in Figures 4.16a and 4.16b, respectively. For orientation I, nine evenly spaced 4×1 SRR strips were axially inserted into the waveguide, totaling 36 SRRs. For the rest of the chapter, this will be referred to as the 4×1 strip array. A single 4×9 sample was used for the transverse orientation II, again with 36 SRRs. Note

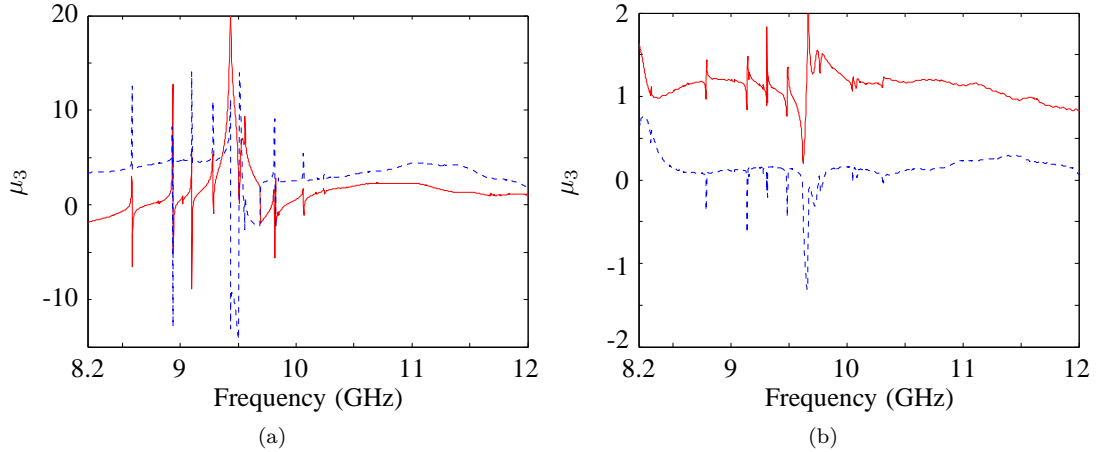


Figure 4.15: The effective relative permeability μ_3 extracted from poor calibrations and measurements, caused by liquid nitrogen seeping into the waveguide components. The solid red and dashed blue curves represent the real (') and imaginary (") parts, respectively. In (a), the waveguide parts with SRR were submerged directly into a bath of LN_2 . In (b), vacuum grease was applied to the seams of the waveguide connections.

that the conducting SRRs are alternately flipped in the vertical direction. This is done so that when image theory is applied along the waveguide walls, the arrays look infinitely periodic in the x and y directions. Also, as pointed out by Smith *et al.* [64], the symmetrical arrangement of the SRRs, as in our case, reduces the magnetoelectric coupling that is responsible for the bianisotropic behavior. For both cases, the dominant TE_{10} mode is excited in the waveguide, which has the electric field in the y direction (Figures 4.16c and 4.16d), or along material axis 2.

In order for these resonating elements to have effective properties, an effective length, L , has to be defined. Thus the propagation factor for a wave propagating through this effective material is given by

$$p = e^{-jk_{0z}nL}$$

where n is the effective refractive index and k_{0z} is the longitudinal wave number of an empty waveguide. Note that measurements of the two oriented samples give two different indices, n_{I} and n_{II} . Slightly different effective lengths were used, with the 4×9 sample being 2.5 mm and the 4×1 strip sample being 2.35 mm, to be consistent with the diced dimensions.

Using a ProtoMat S62 PCB milling machine, deep grooves were milled on a Rohacell 51 IG foam to be used as sample holders for the 4×1 SRR strips. The sample holders ensure equal separation between the samples and prevent them from moving during the measurements. The Rohacell foam has a room temperature relative

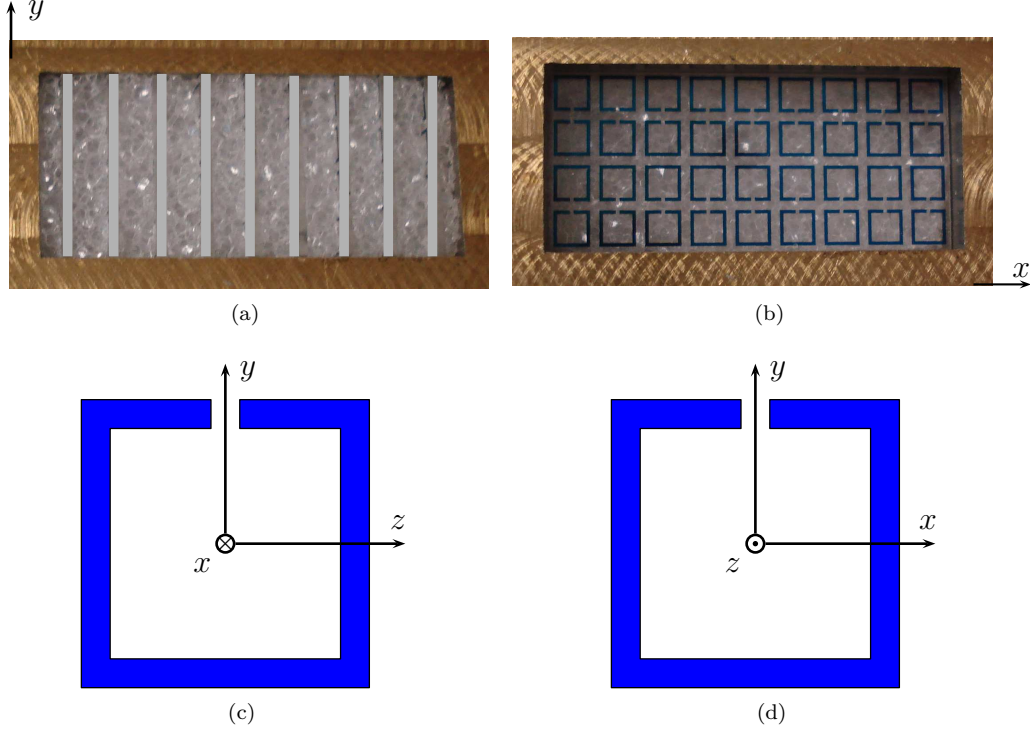
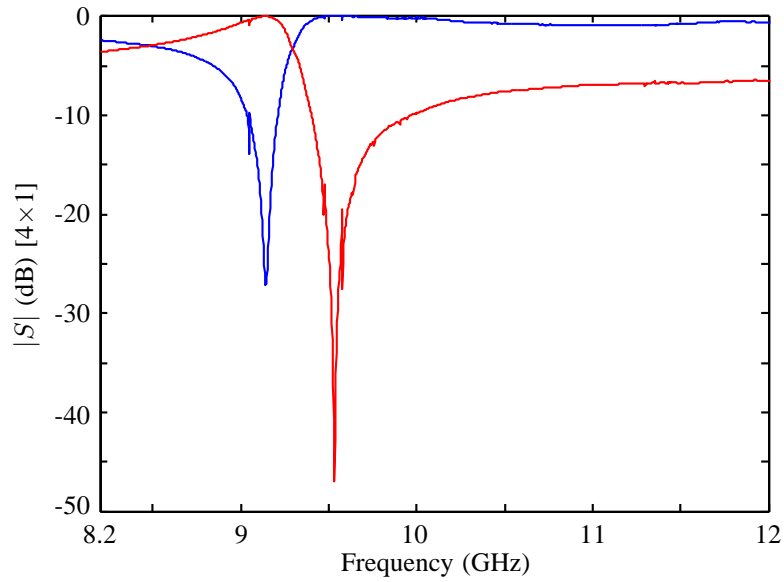


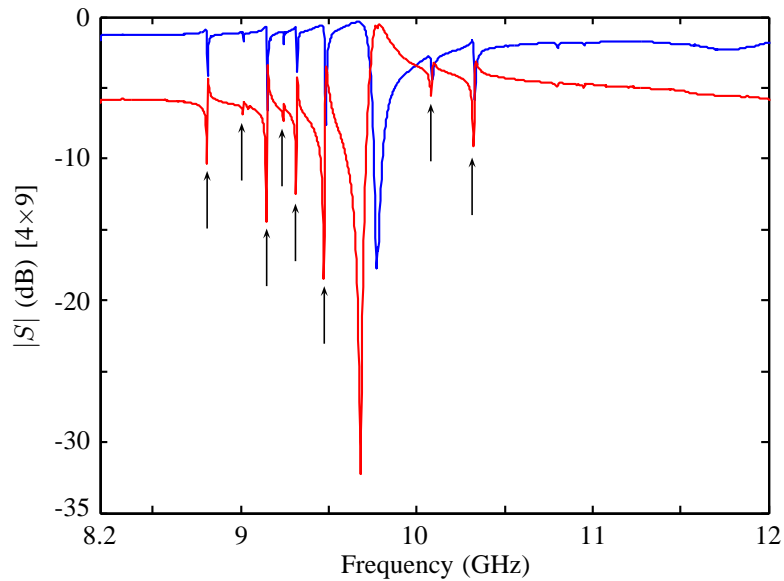
Figure 4.16: Photographs of diced 4×1 and 4×9 YBCO SRR arrays on MgO substrate aligned inside a WR-90 waveguide with orientations (a) I and (b) II, respectively, for measurements. The gray bars in (a) are included to clearly mark the locations of the 4×1 strips. The material axes corresponding to the Cartesian axes are shown for orientations (c) I and (d) II.

permittivity of 1.07 and a loss tangent of 0.0021 at 10GHz [65], which is very similar to the electromagnetic properties of air. Properties of the foam at 77 K are not available. The SRR samples with the foam (orientation I) and without the foam (orientation II) are then placed inside a WR-90 waveguide, shown in Figures 4.16a and 4.16b, respectively.

For each of the two measurements, the S parameters were deembedded to the material reference planes, and the transmission and reflection coefficient magnitudes are shown in Figure 4.17. The stop band about 9.5 GHz in Figure 4.17a suggests a region of negative μ_1 and positive ϵ_2 . Measurements of the 4×9 array, Figure 4.17b, show eight high- Q resonances in addition to the main resonance at ≈ 9.7 GHz. Their discussion is postponed to the next section. Using the S parameters from these two measurements, the three parameters, μ_1 , ϵ_2 , and μ_3 are calculated from the formulae discussed earlier, with the results shown in Figure 4.18. Near the resonances, Equations (4.17) and (4.18) give two different effective permittivities along material axis 2. However, away from the resonant locations, the two have similar values.



(a)



(b)

Figure 4.17: Measured reflection (S_{11} , blue curve) and transmission (S_{21} , red curve) coefficient magnitudes of (a) the nine 4×1 SRR strips and (b) 4×9 SRR array, respectively, placed inside the waveguide section with the whole structure cooled to ≈ 76 K. The markers in (b) indicate the locations of the sharp resonances.

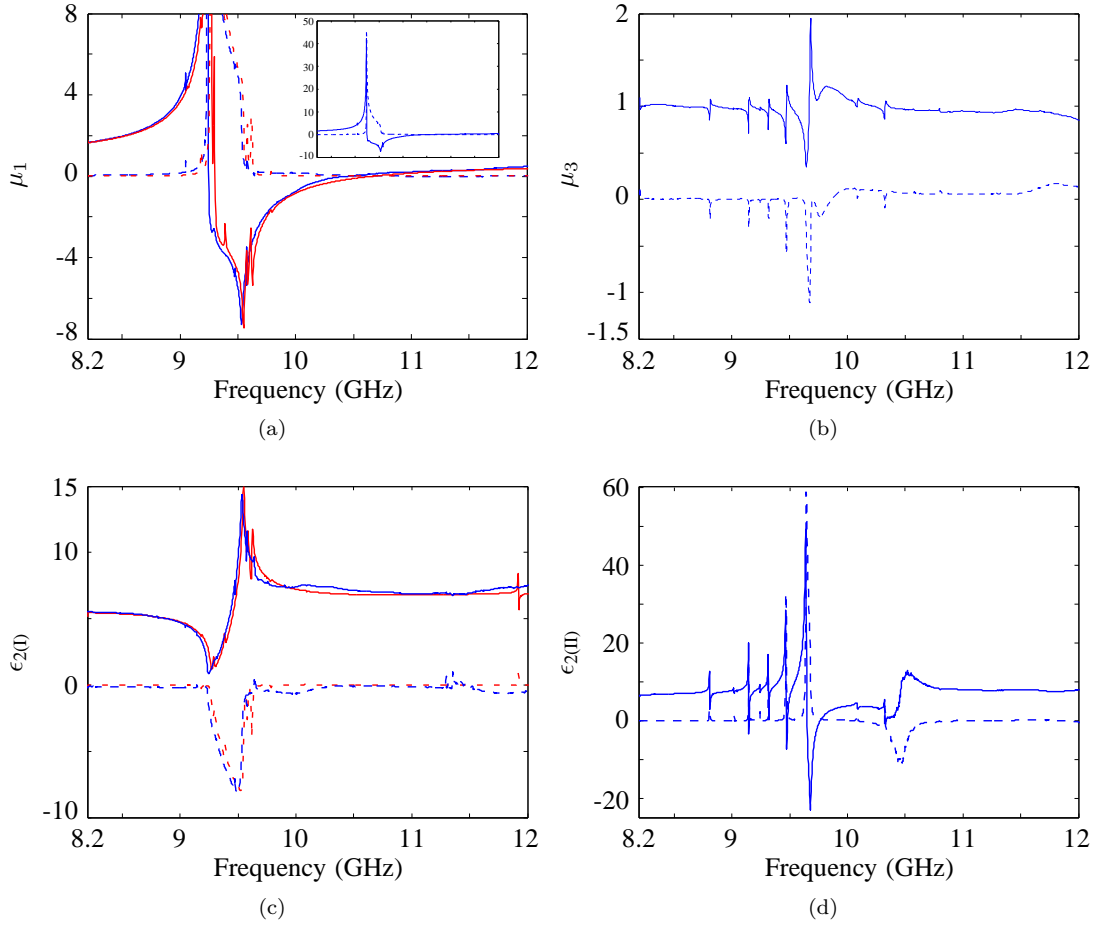


Figure 4.18: Effective parameters extracted from waveguide measurements of the two oriented samples, with (a) zoomed in μ_1 , (b) μ_3 , (c) $\epsilon_{2(I)}$, and (d) $\epsilon_{2(II)}$. The blue and red curves are measurements and waveguide simulations, respectively. The solid and dashed curves represent the real (') and imaginary (") parts, respectively. The inset plot in (a) shows the full μ_1 from the measurement.

The magnetic plasma frequency of this resonant structure is 10.45 GHz, $\mu'_1=0$ in Figure 4.18a. Just below this frequency, between 9.25 GHz and 10.45 GHz, the real part of the relative permeability μ'_1 is negative, which is consistent with previously published work on SRRs. Generally, the imaginary part μ''_1 , corresponding to loss, is large in this frequency band for room temperature normal conducting SRRs. The extracted value from the HTS SRR arrays however shows that at frequencies above the frequency where μ'_1 is at its minimum, μ''_1 quickly drops to near-zero. This is a property that is not observed in normal conducting SRRs on lossy substrate, as shown in the extracted μ_1 for the copper SRRs on a Rogers 3010 substrate, Figure 4.19. The Rogers 3010 substrate has a dielectric constant of 10.2 with an loss tangent of 0.0022 at 10 GHz. [60] The magnetic loss tangents ($\tan \delta_\mu = |\mu''/\mu'|$) for the Cu SRR array at $f(\mu'_{\min}) = 9.59$ GHz and $f(\mu'_{\min})+100$ MHz

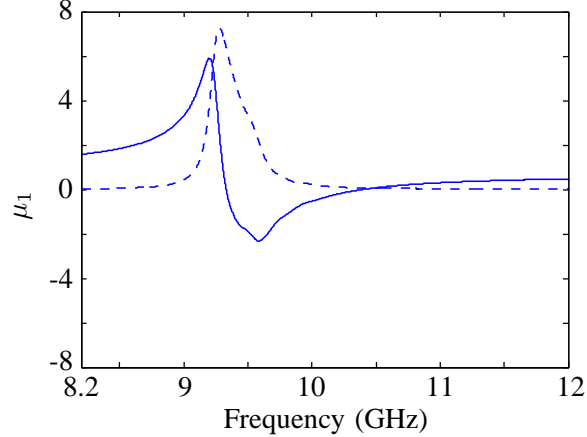
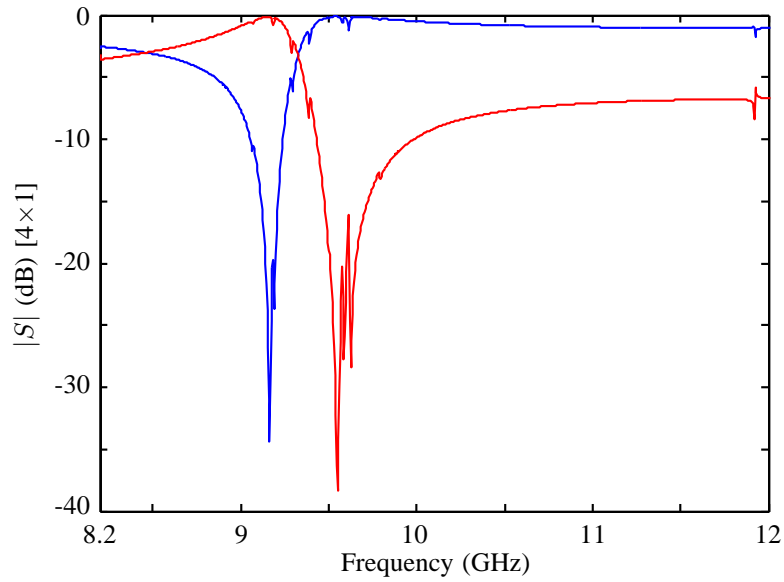


Figure 4.19: Effective permeability (μ_1) extracted from room temperature measurement of the copper SRR arrays on a Rogers 3010 substrate, plotted on the same scale as Figure 4.18a for comparison. The solid and dashed blue curves represent the real ($'$) and imaginary ($''$) parts, respectively. The same measurement and calibration approach was used as in the cryogenic case.

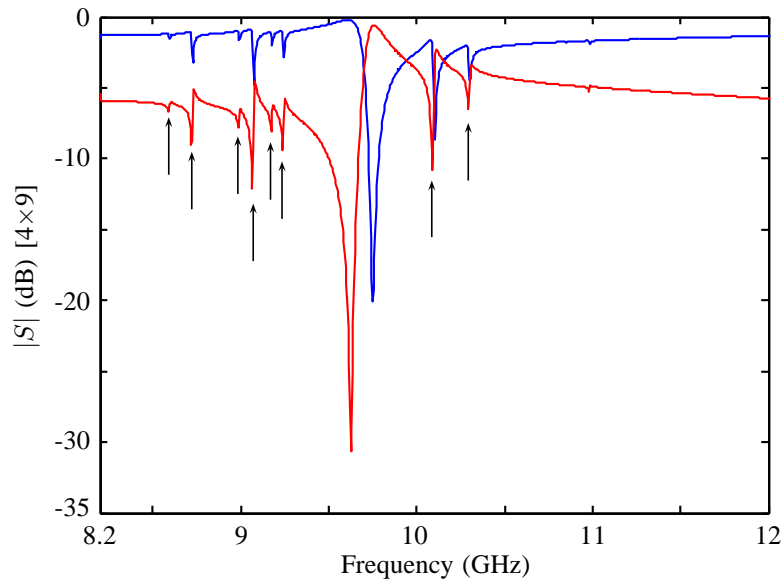
are 0.911 and 0.523, respectively, a 42% reduction. The $\tan \delta_\mu$ for the HTS SRR array at $f(\mu'_{\min}) = 9.53$ GHz and $f(\mu'_{\min}) + 100$ MHz are 0.324 and 0.068, respectively, a 79% reduction. In Figure 4.18c, we notice that ϵ'' is negative at frequencies just above where ϵ' is at a minimum. This is also seen in many published works on SRRs.

4.6 COMPARISON TO SIMULATIONS

For comparison, the 4×1 SRR strips and 4×9 SRR samples placed inside the waveguide were modeled in the Ansys HFSS full-wave FEM simulator. In the simulations, perfect electric conductor (PEC) was used for the waveguide walls, the relative permittivity of MgO was set to 9.7 with a $\tan \delta$ of 5×10^{-6} , and the electrical conductivity of YBCO was set to $\sigma = (R_{St})^{-1} = 2.847 \times 10^9$ S/m, calculated from the sheet resistance of YBCO from [59]. The simulated S parameters, Figure 4.20, from the orientation I and II models agree well with our low temperature measurements. The multiple sharp resonances above and below the main resonances are also present, as shown in Figure 4.20b. The calculated effective material parameters from the waveguide simulations are shown as solid and dashed red curves in Figure 4.21. For comparison with the measurements, the effective μ_1 and $\epsilon_{2(1)}$ from the waveguide simulation are also plotted together with the measured results in Figures 4.18a and 4.18c, showing a 54 MHz offset for $f(\mu'_1 = 0)$.



(a)



(b)

Figure 4.20: Reflection (S_{11} , blue curve) and transmission (S_{21} , red curve) coefficients of the (a) 4×1 and (b) 4×9 SRR array sample from full-wave waveguide simulations. The markers indicate the locations of the sharp Fano-like resonances.

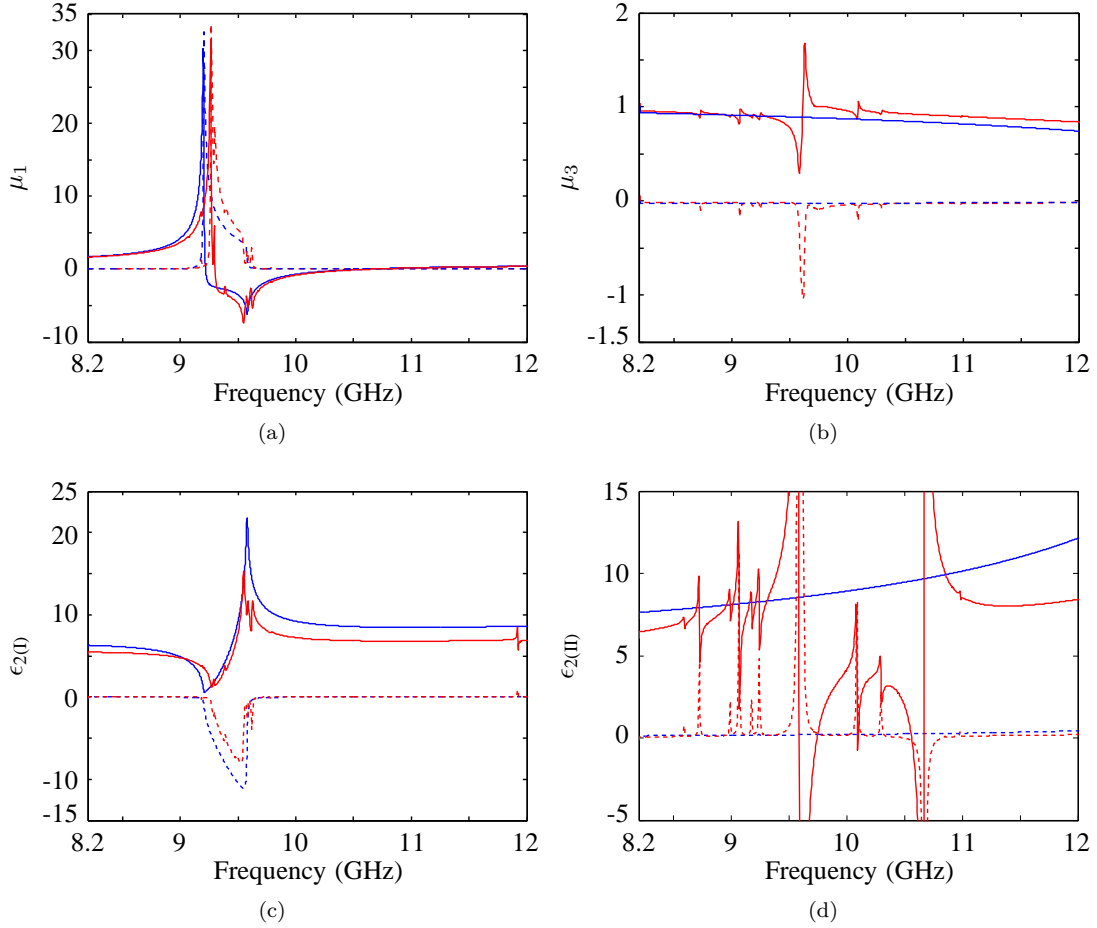


Figure 4.21: Effective parameters extracted from the free space and waveguide simulations of the two SRR arrays, with (a) μ_1 and (c) $\epsilon_{2(I)}$ from orientation I, and (b) μ_3 and (d) $\epsilon_{2(II)}$ from orientation II. The red and blue curves represent the waveguide and free space solutions, respectively. The solid and dashed curves are the real (') and imaginary (") parts, respectively.

The free space effective parameters of SRR arrays are of practical interest for applications such as metamaterial cloaks. [4, 5] Thus, free space models of the HTS SRR arrays were created in separate HFSS simulations and the effective parameters extracted for comparison and validation purposes. Electric and magnetic walls are assigned at the transverse boundaries to define the directions of the electric and magnetic fields (\mathbf{E} parallel to axis 2) and to emulate a uniform plane wave normal incident on the SRR samples, as shown in Figure 4.8. The details of the simulation setup are presented in Section 4.3.

A set of scattering parameters is obtained for each of the orientations, from which the effective relative constitutive parameters are retrieved using the free space extraction method discussed in [57, 61] and Appendix B. The model with which the SRR array is aligned with orientation I allows for the extraction

of μ_1 and $\epsilon_{2(\text{I})}$, whereas orientation II allows for $\epsilon_{2(\text{II})}$ and μ_3 extraction. These results are shown together with results from the waveguide simulations in Figure 4.21, as solid and dashed blue curves. There is a slight offset in frequency between the two simulations: $f(\mu'_{1,\text{min}})$ differ by 28 MHz and $f(\epsilon'_{2\text{I,max}})$ differ by 29 MHz. The offset is likely a result of imperfect meshing in the waveguide simulation, as further simulations suggest. The obvious disagreements from the two extraction techniques can be seen in the μ_3 and $\epsilon_{2(\text{II})}$ curves. As mentioned earlier, a reason for this is that the magnetic fields are present in both the transverse and longitudinal directions inside the waveguide, but not in the free space case. The anti-resonant behavior at 10.66 GHz is a result from dividing by a near-zero μ_1 in Equation (4.18).

4.7 DISCUSSION

In both the waveguide and cryogenic measurement (Figure 4.17b) and low loss simulation (Figure 4.20b) of the 4×9 sample, the S parameters show eight high- Q resonances in addition to the main resonance, which are not seen in the low loss free space simulation. Kumley *et al.* [66] pointed out that high- Q resonances (referred to as Fano resonances) can arise from the slight variations in the structural dimension in the element array. However, the SRRs in the simulation have the same dimensions, thus ruling out this possibility. A single Fano or “trapped-mode” resonance has also been reported in [67, 68] from free space measurements of asymmetrically-split-ring arrays. The sharp resonances from our measurement have Q -factors ($f_r/\Delta f_{3\text{dB}}$) as high as 1400, which is much higher than those observed in [67] for the asymmetrical SRR arrays also of YBCO thin films. In the case where the SRRs are made of copper on a Rogers 3010 substrate, room temperature measurements did not clearly reveal these high- Q features because the losses in the conductor and substrate damp them out.

In summary, arrays of 4×1 strips and 4×9 YBCO split-ring resonator arrays were independently measured inside a WR-90 rectangular X-band waveguide at liquid nitrogen temperature. From the two sets of recorded S parameters, the effective constitutive parameters are retrieved where the SRR array is assumed to have an effective length and take on a homogeneous medium described by diagonal permittivity and permeability tensors. The extracted results from the measurements agree well with those from the low loss waveguide and free-space full-wave simulations. The extracted effective permeability shows a negative μ' in the frequency

band between 9.25 and 10.45 GHz, with the imaginary part μ'' quickly dropping to near-zero close to the minimum of μ' , property not observed with room temperature normal conducting SRR arrays.

CHAPTER 5

RADOME MEASUREMENT

CONTENTS

5.1	Introduction	68
5.2	Room Temperature Measurement Setup	69
5.3	Radome Measurements and Simulations	73
5.4	SRR Optimization	77
5.5	Cryogenic Measurement Setup	89
5.6	Cryogenic Measurements	91

5.1 INTRODUCTION

In Chapter 1, the requirements for the radome were defined, two of which will be addressed in this chapter. The first is that a receiver antenna/probe located in the interior of the radome is isolated from an exterior transmitter and the second is that the presence of the radome should not greatly disturb the communication path between the transmitter and its intended receiver. The testing environment chosen for this research work is a parallel plate waveguide (PPW), since it is semi-confined, which allows for cooling of the radome that is placed inside. In addition, the vertical dimension of the radome is reduced to the height of the PPW.

In this chapter, the performance of the metamaterial radomes constructed of both copper and YBCO SRR

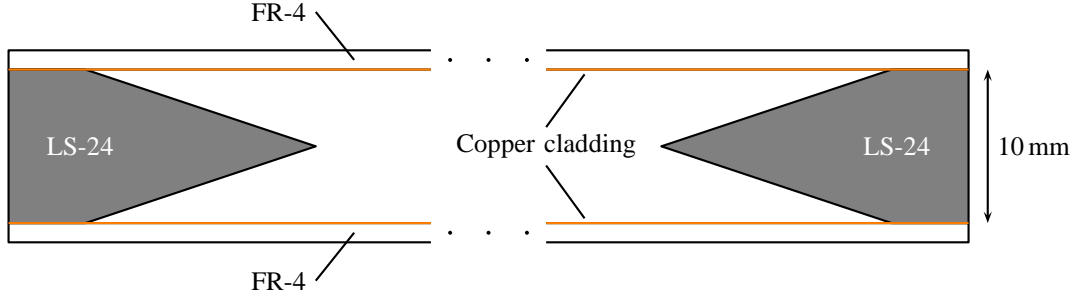


Figure 5.1: Cross section sketch of the parallel plate waveguide for characterizing the metamaterial radome. The FR-4 copper cladding thickness is $35\ \mu\text{m}$, respectively. LS-24 absorber wedges were placed along the boundaries of the parallel plate waveguide to minimize reflection and provide a constant spacing between the two plates.

arrays is characterized at room and cryogenic temperatures. We begin by discussing the room temperature measurement setup, which consists of a parallel plate waveguide with a transmitter probe to excite a wave in the waveguide. A receiver probe is placed at the center and behind the radome to measure the received power relative to that with no radome present. Next, the performance of the radome is defined. The room temperature measurements of a copper SRR radome are compared to the full-wave simulations to ensure the two results agree. An optimization process in the simulation is employed to find the optimal SRR dimensions for the superconducting radome. Due to computing resources, only a three layer radome is optimized. The cryogenic measurement setup for the HTS radome characterization is then discussed. Finally, the measurements of the HTS radome are presented.

5.2 ROOM TEMPERATURE MEASUREMENT SETUP

The measurement setup was chosen to be a parallel plate waveguide that has the 10 mm height of the cylindrical radome. A sketch of the cross section cut of the waveguide is shown in Figure 5.1. The waveguide is constructed of two single-sided copper cladding FR-4 substrates. Emerson and Cuming LS-24 non-magnetic absorber wedges were placed at the edges to reduce reflection from the finite extend of the waveguide. The absorbers also help to maintain a 10 mm separation between the FR-4 sheets. Two $50\ \Omega$ coaxial probes were used; one acts as a transmitter to excite an EM wave inside the waveguide and one as a receiver. Each probe has a 0.28 mm diameter center conductor extending 6 mm into the waveguide.

In the HFSS simulations, the LS-24 absorber is modeled as a dispersive, homogeneous, isotropic material

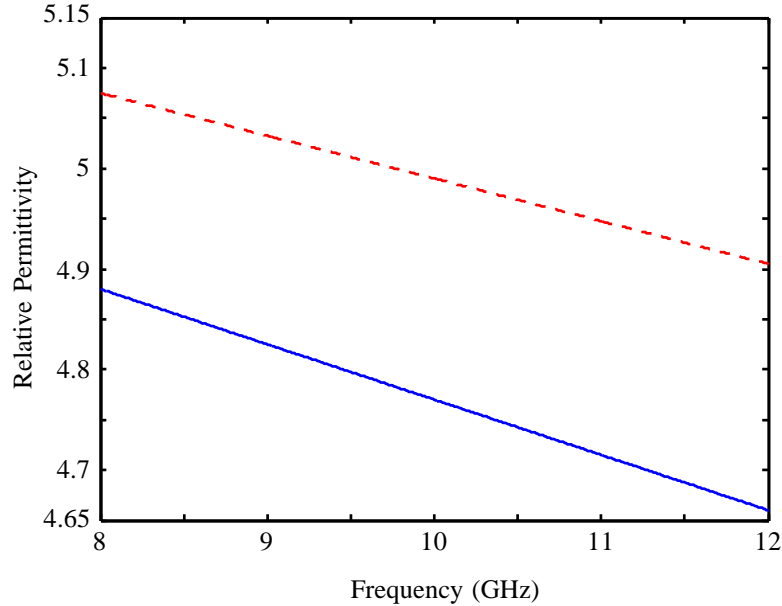


Figure 5.2: Complex relative permittivity versus frequency of a material modeled in HFSS of the LS-24 absorber. The solid blue and dashed red curves are the real (') and imaginary (") parts, respectively.

with the complex relative permittivity values shown in Figure 5.2, extracted from the Emerson and Cuming LS-24 datasheet [69]. The shape of the absorber greatly affects the reflection at the boundaries of the parallel plate waveguide. Four different absorber settings on a $400 \times 400 \text{ mm}^2$ PPW were studied in the simulations to demonstrate the importance of the absorber geometry:

- (1) No absorber;
- (2) Flat (untapered) absorber;
- (3) Horizontal taper absorber wedges; and
- (4) Vertical taper absorber wedges.

Figure 5.3 shows the orientations for the horizontally and vertically tapered absorber wedges. The flat absorber is modeled as a rectangular block of height 10 mm and extends 40 mm into the waveguide on each side. For each case, two coaxial probes, placed 200 mm apart, were inserted into the empty PPW and the transmission coefficient was recorded. The results in Figure 5.4 show that the vertical tapered absorber wedges have the lowest reflection from the waveguide edges. Note that the case with the horizontally tapered wedges, used in the metamaterial cloak in Schurig's paper [4], has standing wave features that are not seen in the vertically

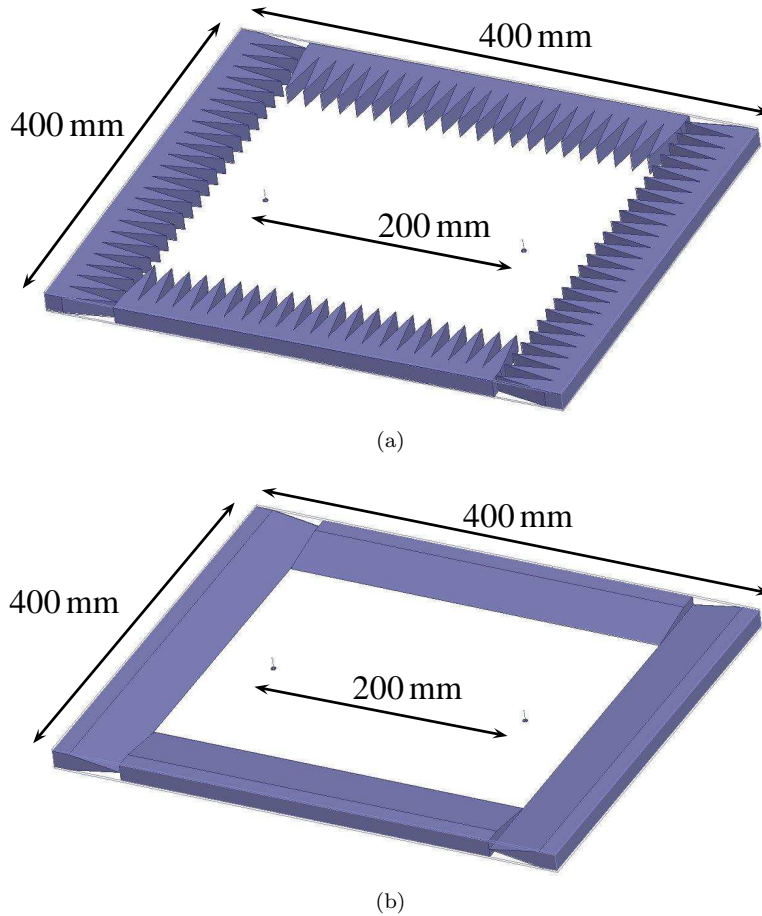


Figure 5.3: The shapes and orientations for the (a) horizontally tapered absorber and (b) vertically tapered absorber. The size of the parallel plate waveguide is $400 \times 400 \text{ mm}^2$. The height of the waveguide is 10 mm.

tapered case. In the simulations, a PPW that has vertically tapered LS-24 wedges was compared to one which has perfectly matched layers (PML) assigned at the edge boundaries. The simulated $|S_{21}|$ of the two cases are plotted (on the same scale as Figure 5.4) together in Figure 5.5, blue solid curve for PML and red solid curve for vertically tapered wedge. In the frequency band of interest, they are within 1 dB of each other.

The empty PPW with vertically tapered absorbers was also measured. A coaxial Line-Reflect-Line (LRL) calibration was performed to the end of the coaxial connections, just before the probes, as sketched in Figure 5.6. “Line 1” and “Line 2” standards are male-to-male coaxial connectors, 21.8 mm and 26.9 mm long, respectively. The “Reflect” standard is a zero-length coaxial short. As in the simulations, the two coaxial probes are spaced 200 mm apart. The measured $|S_{21}|$, Figure 5.7, agrees with the simulated results in Figure 5.4d.

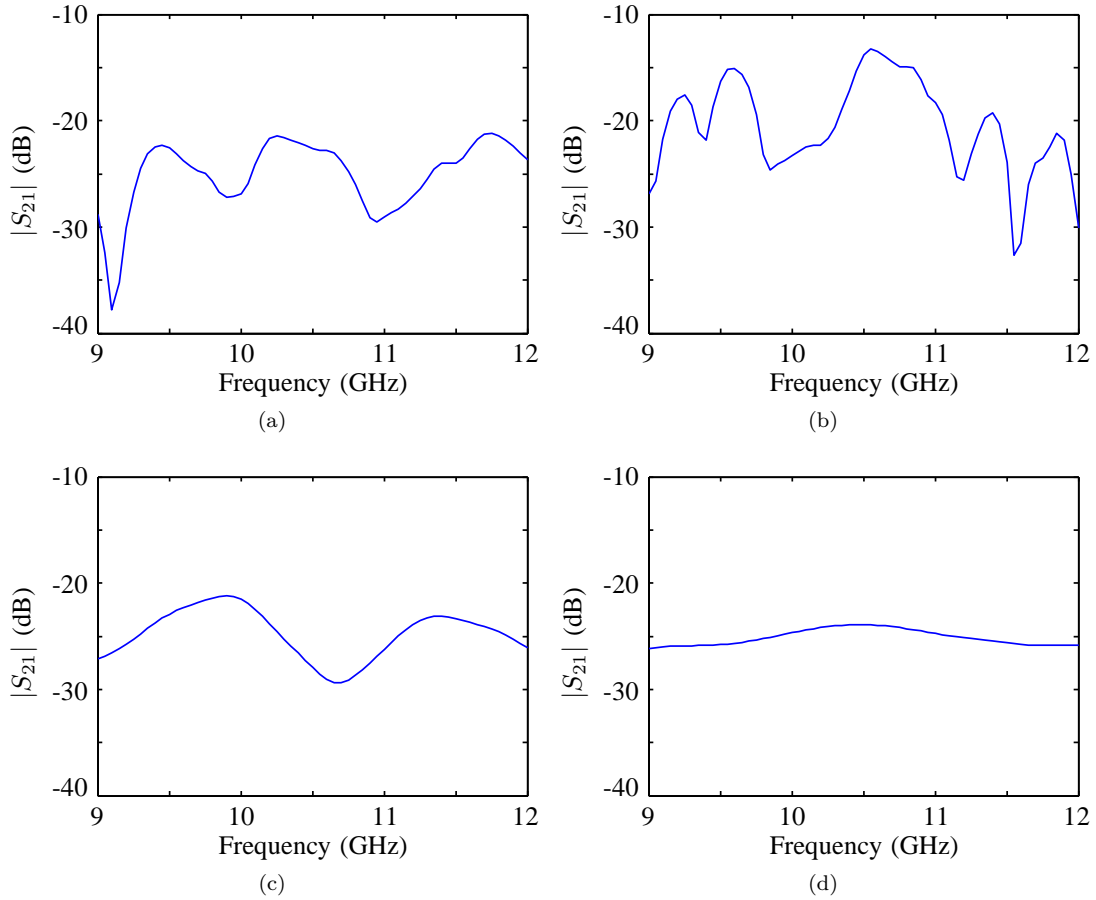


Figure 5.4: Simulated S_{21} for an empty PPW with different absorber shapes and orientations. The two coaxial probes spaced 200 mm apart, for (a) no absorber, (b) flat absorber, (c) horizontal taper absorber, and (d) vertical taper absorber.

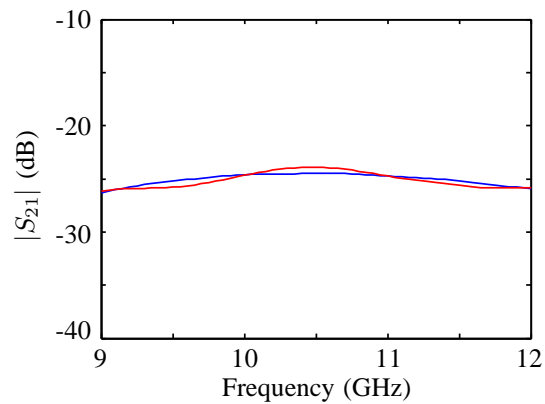


Figure 5.5: Simulated S_{21} results of an empty PPW where the waveguide boundaries are terminated by perfectly matched layers (blue curve) and vertically tapered absorber wedges (red curve). The two curves are within 1 dB in the frequency band.

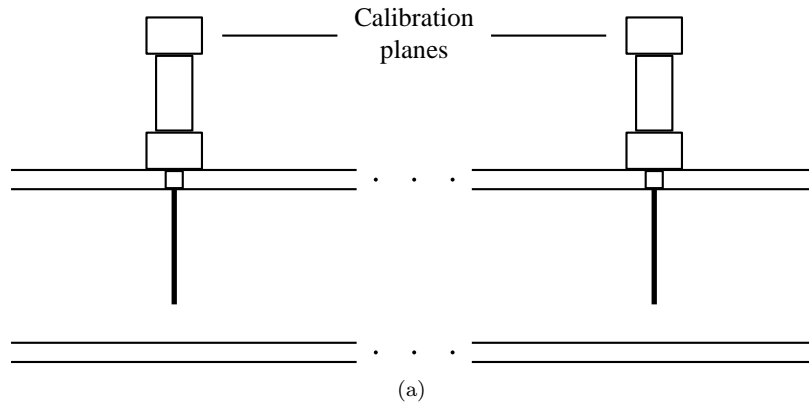


Figure 5.6: (a) Sketch of the coaxial probes inserted into the parallel plate waveguide, showing the Line-Reflect-Line calibration planes. (b) A photograph of the coaxial probe used in the measurements.

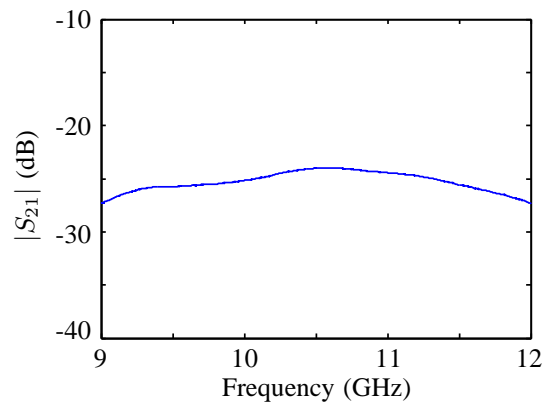


Figure 5.7: Measurement of an empty $300 \times 240 \text{ mm}^2$ PPW, described in Figure 5.1, with the two probes distanced 153 mm apart.

5.3 RADOME MEASUREMENTS AND SIMULATIONS

A one-layer radome was constructed with copper SRR arrays from Section 4.3, where all the elements in the radome have the same dimensions. These structures are measured and simulated in the parallel-plate setup from above. The room temperature measurements are used to validate the full-wave simulations. Then the dimensions for the HTS SRR radome can be optimized in the simulations to predict the cryogenic

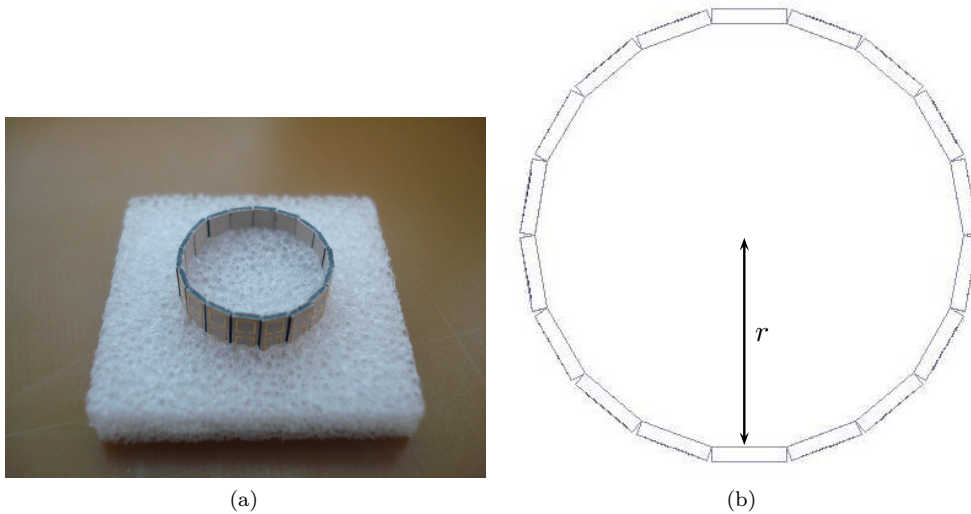


Figure 5.8: (a) Photograph of the single layer radome made of 18 copper SRR arrays. (b) The radius corresponding to Equation (5.1). The radius r for this radome is 7.29 mm

measurement results.

The one-layer radome is constructed from 4×1 SRR strips placed adjacent to each other to form a cylindrical structure, as shown in Figure 5.8. The dimensions of the copper SRRs are given in Figure 4.5. The width of each strip is approximately 2.57 mm. To ensure that the 4×1 strips can be placed without gaps in between, the distance of the strips from the center, Figure 5.8b, is chosen to be

$$r = \frac{w}{2 \tan(180/n)} \quad (5.1)$$

where n is the number of 4×1 SRR arrays and w is the strip width. For the one-layer case, $n=18$ and $r=7.29$ mm. This radome was constructed and centered inside a 300×230 mm² PPW for the measurement. Figure 5.9 shows the relative placements of the coaxial probes during a measurement. For structural support and ensuring that the 4×1 strips are situated at the correct radius, a sample holder was made by milling deep grooves into a Rohacell foam. The finished structure is shown in Figure 5.8. The properties of Rohacell foam were discussed in Chapter 4. Two coaxial probes were inserted into the PPW for measuring the S_{21} . The first probe (port 1) was placed 83 mm from the center, while the second probe was placed at the center of the radome and 70 mm from center for characterizing the isolation and shadowing (defined below), respectively. Figure 5.10 shows the measured S_{21} at the center with and without the presence of the radome, shown as the solid blue and dashed red curves, respectively. By subtracting the S_{21} (in dB) from the empty waveguide

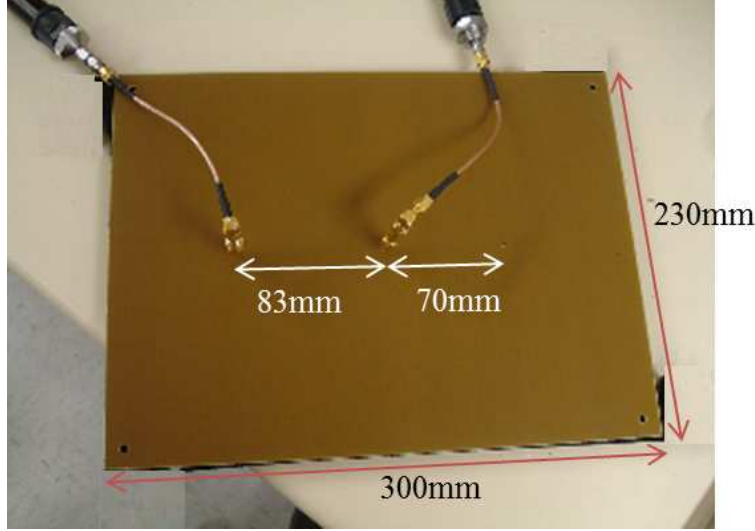


Figure 5.9: A photograph showing the relative placements of the coaxial probes during a measurement. This 300x230 mm² parallel plate waveguide size is convenient for initial testings and validations with the simulations.

measurement, the isolation is determined:

$$\text{Isolation(dB)} = S_{21,\text{empty}}(\text{dB}) - S_{21,\text{radome}}(\text{dB}) \quad (\text{for probe location inside the radome}) \quad (5.2)$$

Figure 5.10 shows that at 11 GHz, the isolation is 4.3 dB. Next, while leaving the first probe at 83 mm from center, the second probe is now placed 70 mm behind the radome. The S_{21} is shown in Figure 5.11. Similarly to isolation, the shadowing is defined as

$$\text{Shadowing(dB)} = S_{21,\text{empty}}(\text{dB}) - S_{21,\text{radome}}(\text{dB}) \quad (\text{for probe location outside the radome}) \quad (5.3)$$

Figure 5.11 shows that at 11 GHz, the shadowing is 0.55 dB.

Next a three layer radome is studied in the 300x240 mm² PPW, in both the simulations and measurements. The radii of the inner layer (layer 1), middle layer (2) and outer layer (3) are 12.226 mm, 14.688 mm and 17.147 mm, respectively, shown in Figure 5.12. Layers 1, 2, and 3 have 30, 36, and 42 of the 4×1 SRR strips, respectively, with every strip having the same SRR dimensions. The measured and simulated S_{21} are shown in Figures 5.13 and 5.14. Again we see agreement between the measurements and simulations. Note that the SRR dimensions have not been optimized for isolation and shadowing. What is of most interest is that measurements agree with simulations. Although the respective S_{21} curves are shifted in frequency, the features in both the simulation and measurement results are the same. In the simulations, the isolation and shadowing

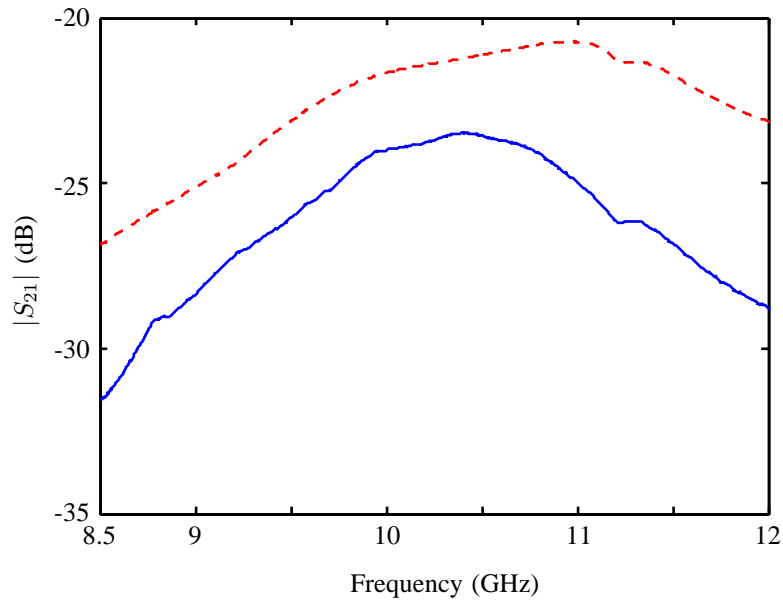


Figure 5.10: Measured transmission coefficient with the receiver probe placed at the center of the radome from Figure 5.8. The measurement setup is shown in Figure 5.9. The solid blue and dashed red curves are measurements with and without the radome, respectively.

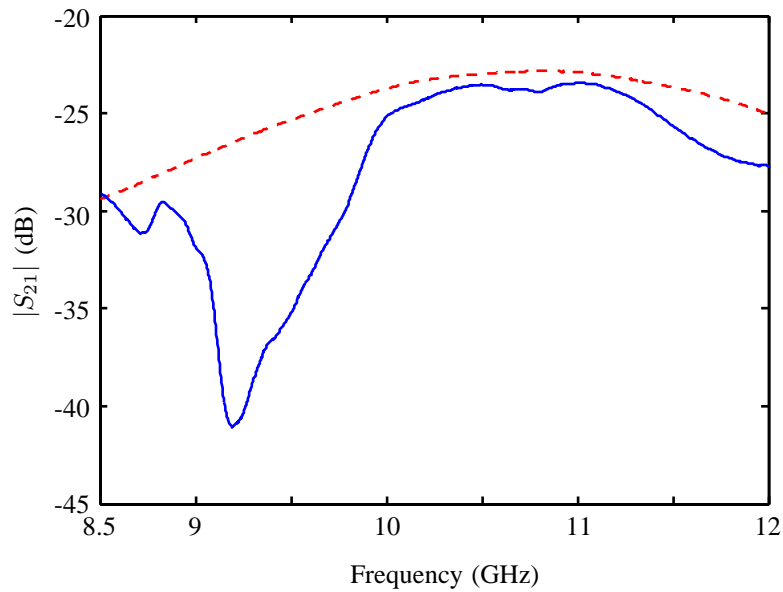


Figure 5.11: Measured transmission coefficient with the receiver probe placed 70 mm behind the radome from Figure 5.8. The measurement setup is shown in Figure 5.9. The solid blue and dashed red curves are measurements with and without the radome, respectively.



Figure 5.12: Three layer radome with uniform SRR dimensions in all the layers.

at 10.9 GHz are 5.3 dB and 3.4 dB, respectively. In the measurements, they are 6.1 dB and 3.9 dB, respectively, at 11.35 GHz.

The three layer radome was also measured in a $600 \times 600 \text{ mm}^2$ PPW with the results shown in Figure 5.15. Although the measurements show standing waves, due to calibration errors, the general shapes of the curve agree with the results from the studies inside a $300 \times 240 \text{ mm}^2$ PPW. At 11.35 GHz, the isolation and shadowing are 5.3 dB and 2.63 dB, respectively.

5.4 SRR OPTIMIZATION

The next step in designing the metamaterial radome is optimizing the SRR dimensions for each layer of the three layer case. The goals of optimization are maximizing the isolation and minimizing the shadowing, while maintaining the 2.5 mm by 2.5 mm size for the SRR elements. In the previous sections, we have demonstrated the ability to match the measurements to the simulations for the three layer copper SRR radome. Likewise in Chapter 4, the measurements and simulations of the HTS SRR arrays inside an X-band waveguide agree to within 54 MHz. Thus, we are confident that results from the simulations of a three layer HTS radome will agree with the measurements. For each of the layer, only the leg and gap dimensions of the SRR elements are varied, Figure 5.16.

For the optimization process, a transmitter probe (port 1) is fixed at 83 mm from the center of the radome.

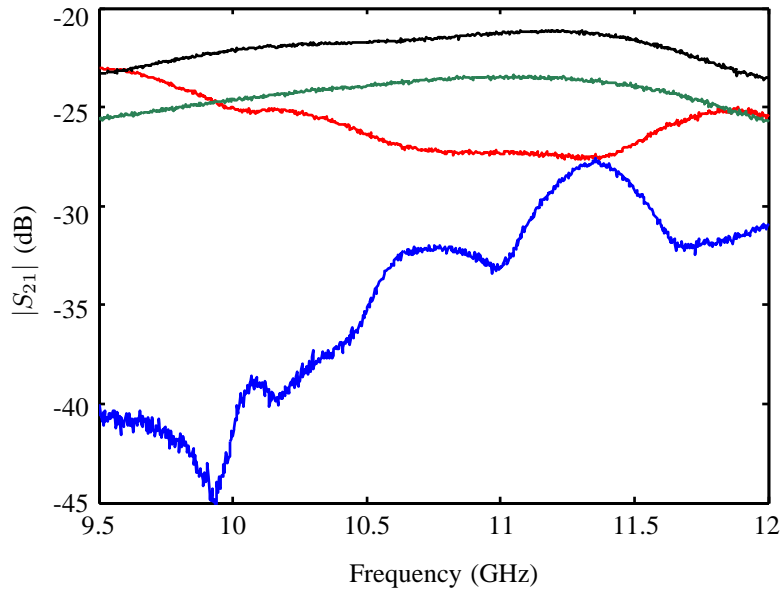


Figure 5.13: Measured transmission coefficient with the receiver probe placed at the center (red curve) and 70 mm behind the three layer radome (blue curve) from Figure 5.12. The measurement setup is shown in Figure 5.9. The black and green curves are the respective measurements of an empty $300 \times 240 \text{ mm}^2$ PPW.

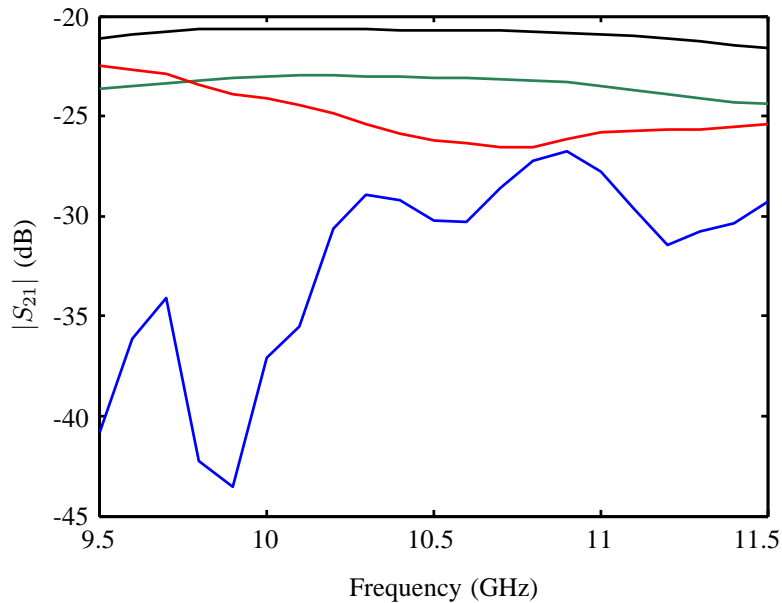


Figure 5.14: Simulated transmission coefficient with the receiver probe placed at the center (red curve) and 70 mm behind the three layer radome (blue curve) from Figure 5.12. The measurement setup is shown in Figure 5.9. The black and green curves are the respective simulation of an empty $300 \times 240 \text{ mm}^2$ PPW.

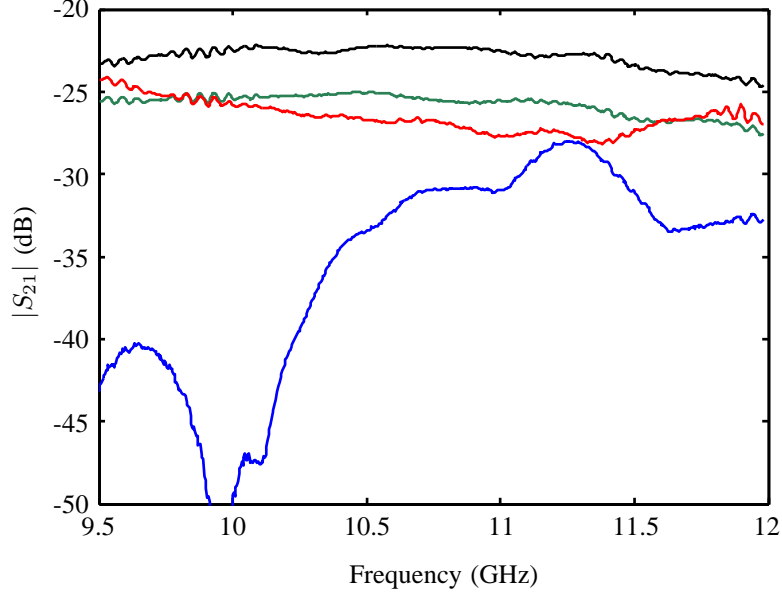


Figure 5.15: Measured transmission coefficient with the receiver probe placed at the center (red curve) and 100 mm behind the three layer radome (blue curve) from Figure 5.12. The measurement setup is similar to that in Figure 5.9. The black and green curves are the respective measurements of an empty $600 \times 600 \text{ mm}^2$ PPW.

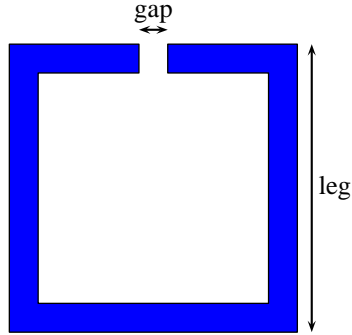


Figure 5.16: Each layer of the radome is made of SRR structures like the one shown here. Different layer have different SRR dimensions. In the optimization, the leg and gap of the SRR for each layer are optimized in the simulation.

Two receiver probes are placed at the center (port 2) and 70 mm (port 3) behind the radome, as shown in Figure 5.17. The SRR leg and gap dimensions of the three layers were simultaneously varied in HFSS, with the goal of maximizing the difference in S_{21} (in dB) and minimizing the difference in S_{31} (in dB) relative to the respective empty PPW values (black and green traces in Figure 5.14). Optimization was performed on both the copper and YBCO SRRs. The optimized SRR dimensions for the copper SRR radome and YBCO SRR radome are summarized in Table 5.1. A frequency sweep of S_{21} and S_{31} were also performed. Figure 5.18 shows the S_{21} and S_{31} for the case where the optimized copper SRR radome is simulated inside

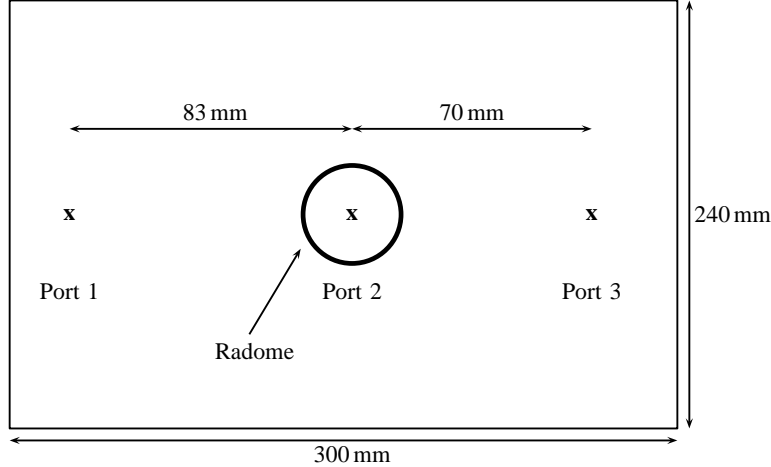


Figure 5.17: The relative positions (top view) of the probes and radome inside a 10 mm tall parallel plate waveguide for the optimization process. The goal is maximizing the difference in S_{21} and minimizing the difference in S_{31} with respect to the empty waveguide simulations.

Layer	Copper		YBCO	
	Leg	Gap	Leg	Gap
1	2.1	0.59	2.08	0.35
2	1.8	0.58	2	0.71
3	1.75	0.15	2	0.15

Table 5.1: Optimized copper and YBCO SRR dimensions for the radomes. The unit for dimension is mm.

the $300 \times 240 \text{ mm}^2$ PPW. The empty PPW S-parameters sweep are also shown as reference. At 10.8 GHz, the isolation and shadowing are 6 dB and 1.8 dB, respectively. This radome was also simulated inside a $400 \times 400 \text{ mm}^2$ PPW, where port 1 is 100 mm from port 2 and 200 mm from port 3. The frequency sweep of S_{21} and S_{31} are shown in Figure 5.19. At 10.8 GHz (the optimal frequency), the isolation and shadowing are 6.6 dB and 2.45 dB, respectively.

The HTS radome with the optimal YBCO SRR dimensions is also simulated in a $400 \times 400 \text{ mm}^2$ PPW. Port 1 is 100 mm from the radome center (port 2) and 200 mm from port 3. Figure 5.20 shows the frequency sweep of S_{21} and S_{31} . At 10.8 GHz, the isolation is 5.88 dB and the shadowing is 0.7 dB. This structure is fabricated and measured. The measurement results are discussed in Section 5.6.

Next we studied the delivered power along the path between the excitation and receiver ports, with the goal to show that the power delivered to the radome interior is reduced relative to the empty PPW case and that outside the radome, the delivered power is not greatly disturbed. The setup for this study is shown in Figure 5.21. A series of $2.5 \times 10 \text{ mm}^2$ rectangles were drawn between the transmitter and receiver ports. Only

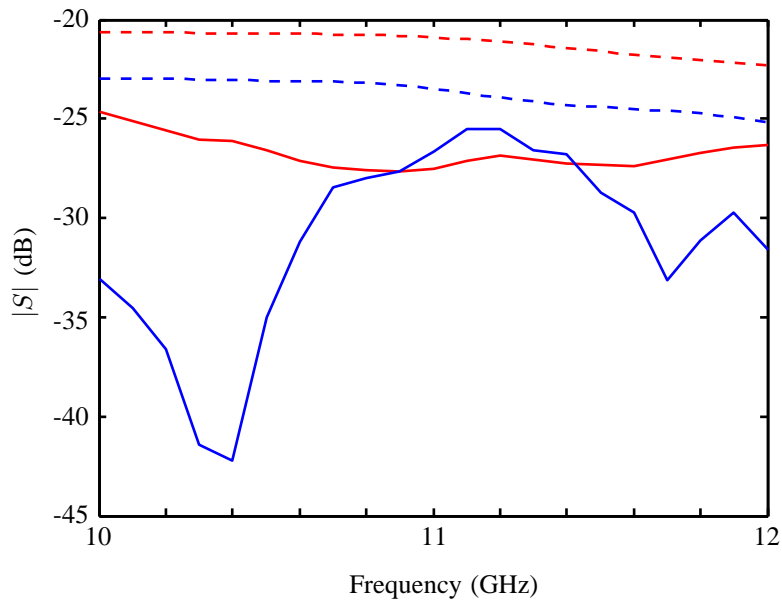


Figure 5.18: Simulated results of the optimized copper SRR radome placed inside a $300 \times 240 \text{ mm}^2$ PPW. The SRR dimensions are given in the Copper columns of Table 5.1. The dashed red and blue curves are the S_{21} and S_{31} for the empty PPW simulation, respectively. The solid red and blue curves are the S_{21} and S_{31} for the empty radome simulation, respectively.

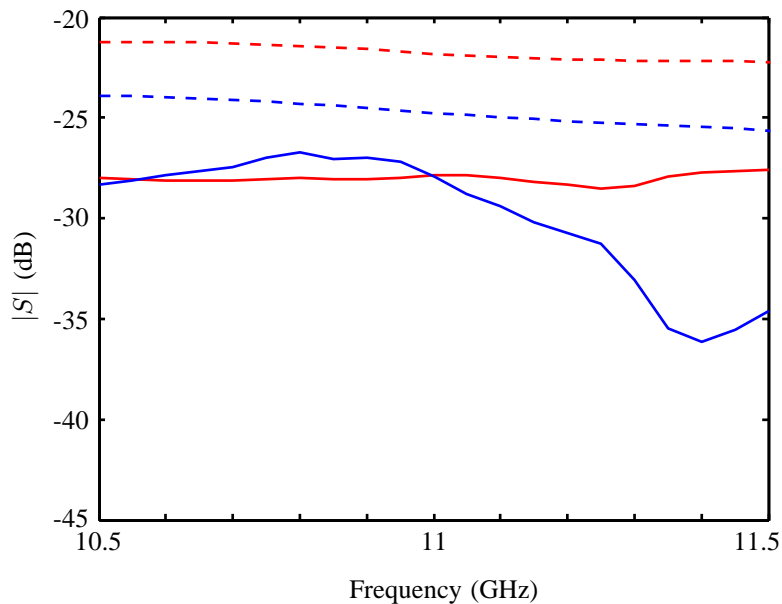


Figure 5.19: Simulated results of the optimized copper SRR radome placed inside a $400 \times 400 \text{ mm}^2$ PPW. The SRR dimensions are given in the Copper columns of Table 5.1. The dashed red and blue curves are the S_{21} and S_{31} for the empty PPW simulation, respectively. The solid red and blue curves are the S_{21} and S_{31} for the empty radome simulation, respectively.

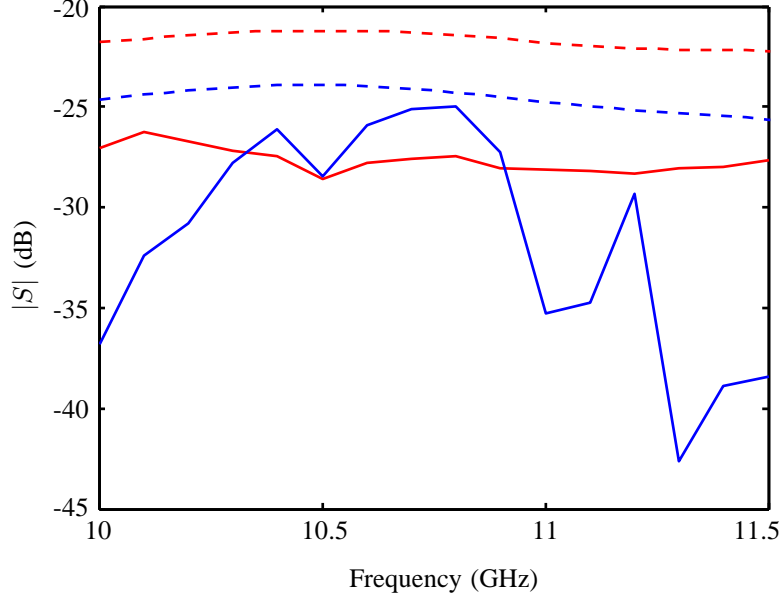


Figure 5.20: Simulated results of the optimized YBCO SRR radome placed inside a $400 \times 400 \text{ mm}^2$ PPW. The SRR dimensions are given in the YBCO column of Table 5.1. The dashed red and blue curves are the S_{21} and S_{31} for the empty PPW simulation, respectively. The solid red and blue curves are the S_{21} and S_{31} for the empty radome simulation, respectively.

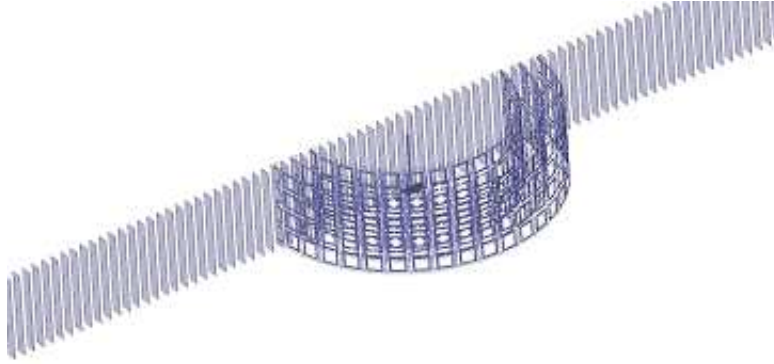


Figure 5.21: The setup for calculating the delivered power in the path between the exciting and receiving probes. The power density is integrated over each rectangle to determine the time-averaged power.

half the structure is shown because symmetry boundary was applied to reduce the computing time. The power across each rectangle is given by

$$P = \int_A \mathbf{S} \cdot d\mathbf{A} \quad (5.4)$$

where \mathbf{S} is the Poynting vector and $d\mathbf{A}$ is the differential area of each rectangle with the direction normal to the surface.

Figures 5.22 to 5.24 show the transmitted power for the copper SRR radome at 10.8 GHz, 10.9 GHz, and 11 GHz, respectively, at points between the ports. Port 1 is located at the positive $x = 100$ mm (outside of the plotted region). Port 2 is at $x = 0$ mm (radome center). Port 3 is at $x = -100$ mm. The empty PPW case, solid blue curve in the figures, is included for reference. The shaded bars indicate the location of the radome. The result in which the radome is replaced by a copper shell of radius 11.3 mm, Figure 5.25, is included to show the benefit of using the SRR radome. We see that the SRR radome provides >8 dB isolation at $x = 0$ mm and a loss of ≈ 3 dB at port 3 relative to the empty case. The copper shell provides excellent isolation, but is ≈ 9 dB down at port 3.

Figures 5.26 to 5.28 show the power sweep for the YBCO SRR radome at 10.8 GHz, 10.9 GHz, and 11 GHz, respectively. The YBCO radome provides >8 dB isolation at $x = 0$ mm and a shadowing of ≈ 2 dB at 10.8 GHz. At 10.9 GHz, the shadowing is ≈ 0 dB and at 11 GHz, the shadowing is -1 dB. In Figure Figure 5.29, the transmitted power for the empty PPW, copper SRR radome, and YBCO SRR radome at 11 GHz is plotted together to show the difference in performance. These results show improvement over the copper SRR radome.

A qualitative study of the power distribution inside the 400×400 mm² PPW is also presented for the following cases:

- Empty PPW at 11 GHz (Figure 5.30a)
- Copper cylinder in PPW at 11 GHz (Figure 5.30b)
- Copper SRR radome at 11 GHz (Figure 5.30c)
- YBCO SRR radome at 11 GHz (Figure 5.30d)

A symmetry boundary is applied to each simulation to reduce the computing time. Thus in each of the figures, only half of the structures is shown. What is plotted in each figure is the power density at each location in the parallel plate waveguide. In Figure 5.30b, there is a great reduction of power distribution in the region behind the copper cylinder. In Figure 5.30c, we see an improvement to the distribution of power behind the copper SRR radome. However, regions of low power also appear away from the direct line of sight. In Figure 5.30d, the power distribution behind the YBCO SRR radome is almost identical to the empty PPW

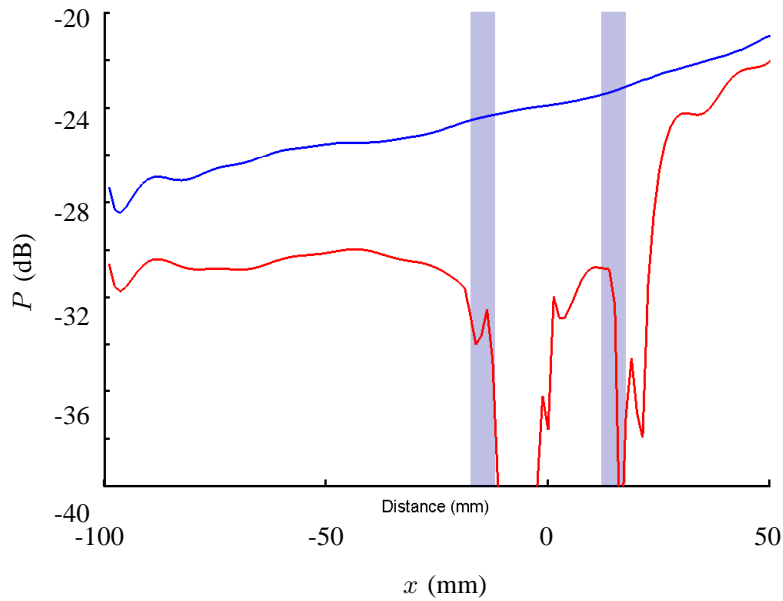


Figure 5.22: The transmitted power at 10.8 GHz (red curve) along the line of sight from the transmitter ($x = 100$ mm) to the receiver ($x = -100$ mm) with the copper SRR radome centered at $x = 0$ mm. The blue curve is the case of an empty PPW characterization. The bar shows the radome cross section.

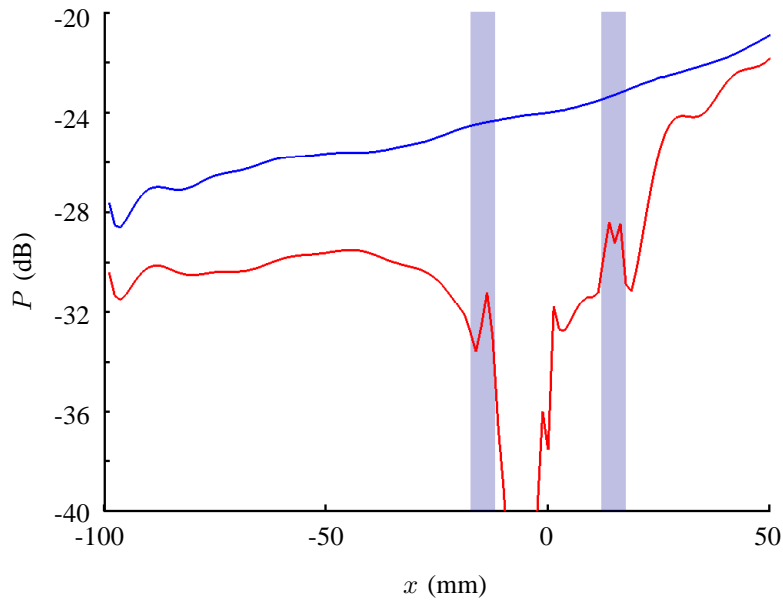


Figure 5.23: The transmitted power at 10.9 GHz (red curve) along the line of sight from the transmitter ($x = 100$ mm) to the receiver ($x = -100$ mm) with the copper SRR radome centered at $x = 0$ mm. The blue curve is the case of an empty PPW characterization. The bar shows the radome cross section.

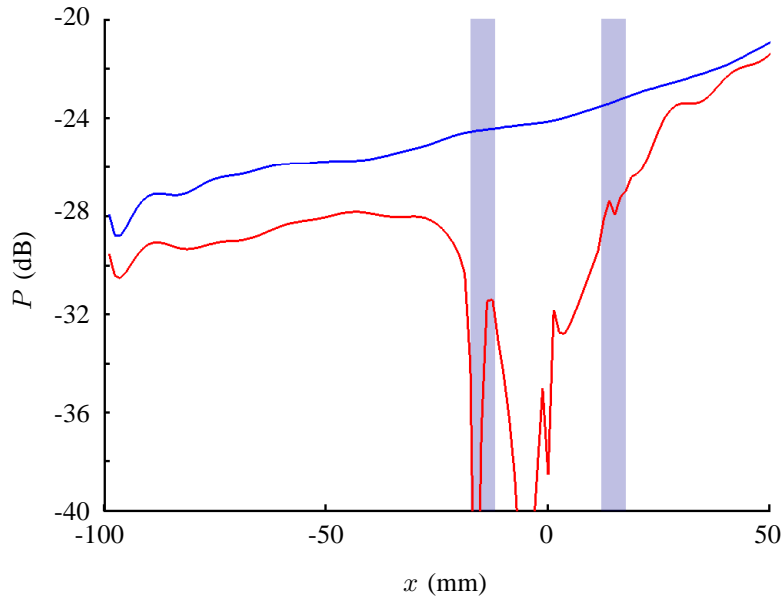


Figure 5.24: The transmitted power at 11 GHz (red curve) along the line of sight from the transmitter ($x = 100$ mm) to the receiver ($x = -100$ mm) with the copper SRR radome centered at $x = 0$ mm. The blue curve is the case of an empty PPW characterization. The bar shows the radome cross section.

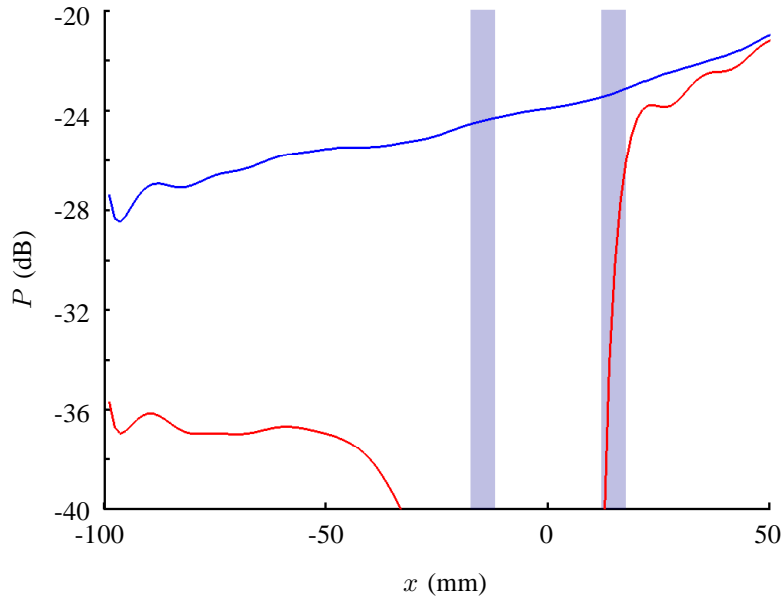


Figure 5.25: The transmitted power at 10.8 GHz (red curve) along the line of sight from the transmitter ($x = 100$ mm) to the receiver ($x = -100$ mm) with the copper cylindrical shell centered at $x = 0$ mm. The blue curve is the case of an empty PPW characterization.

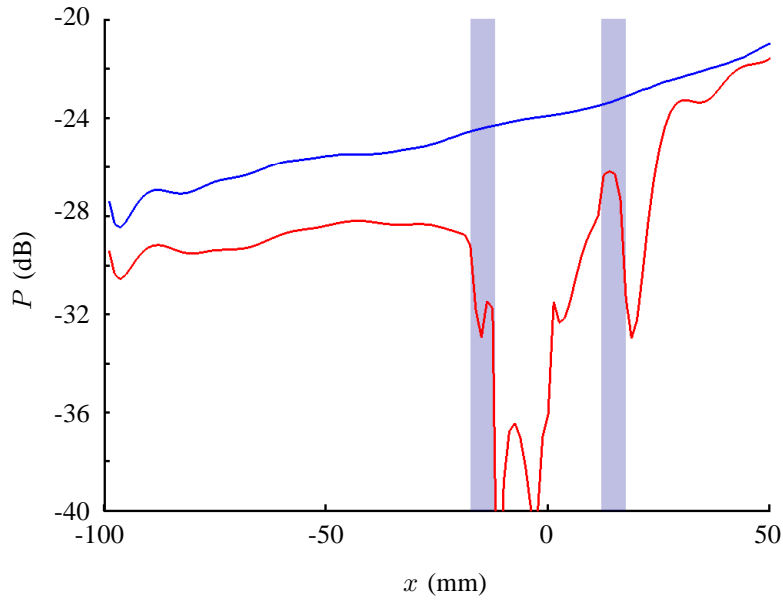


Figure 5.26: The transmitted power at 10.8 GHz (red curve) along the line of sight from the transmitter ($x = 100$ mm) to the receiver ($x = -100$ mm) with the HTS SRR radome centered at $x = 0$ mm. The blue curve is the case of an empty PPW characterization. The bar shows the radome cross section.

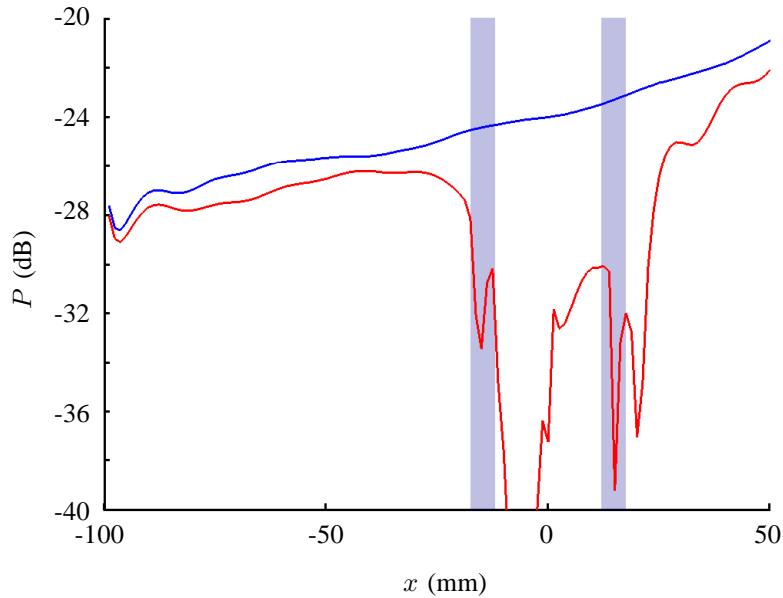


Figure 5.27: The transmitted power at 10.9 GHz (red curve) along the line of sight from the transmitter ($x = 100$ mm) to the receiver ($x = -100$ mm) with the HTS SRR radome centered at $x = 0$ mm. The blue curve is the case of an empty PPW characterization. The bar shows the radome cross section.

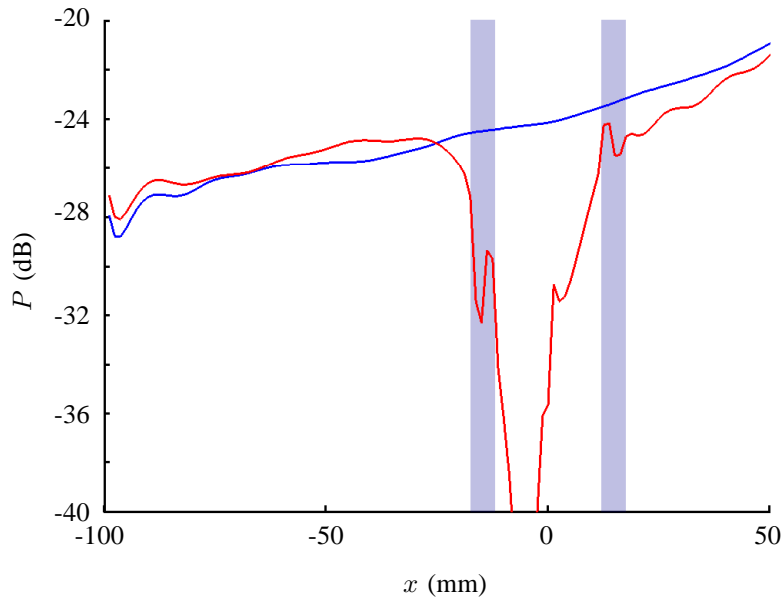


Figure 5.28: The transmitted power at 11 GHz (red curve) along the line of sight from the transmitter ($x = 100$ mm) to the receiver ($x = -100$ mm) with the HTS SRR radome centered at $x = 0$ mm. The blue curve is the case of an empty PPW characterization. The bar shows the radome cross section.

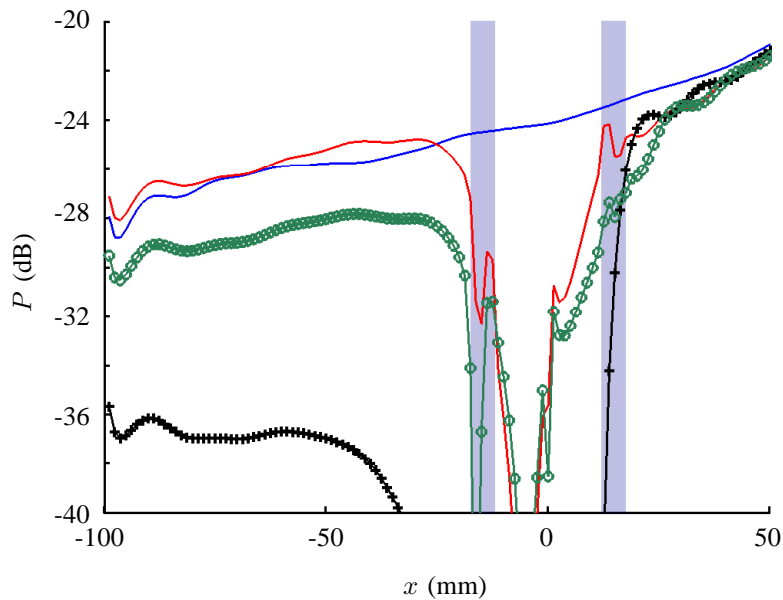


Figure 5.29: A comparison in performance between the copper and YBCO SRR radome at 11 GHz. The YBCO radome has ≈ 2 dB better in regards to the reduction of power versus the copper SRR radome.

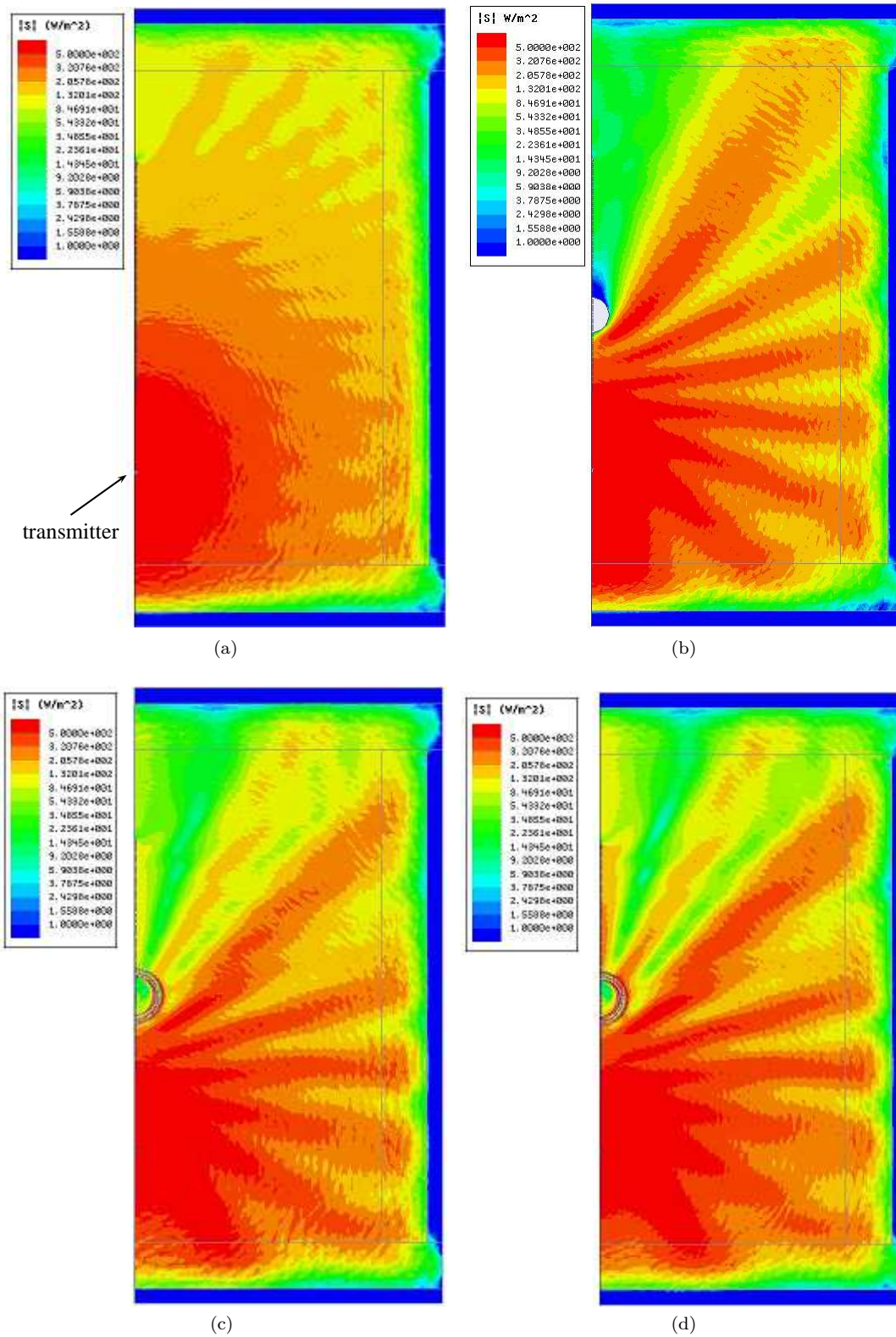


Figure 5.30: Magnitude of the Poynting vector in the parallel plate waveguide for (a) an empty PPW, at 11 GHz (b) a copper cylindrical shell at 10.8 GHz, (c) a copper SRR radome at 11 GHz, and (d) a YBCO SRR radome at 11 GHz. The color scale shows the magnitude level between $1 W/m^2$ (blue) to $500 W/m^2$ (red).

case. Again, regions of low power (nulls) are also present. These are also seen in the measured field plots of the metamaterials cloaks presented by Schurig *et al.* [4] and Kante *et al.* [5].

5.5 CRYOGENIC MEASUREMENT SETUP

The parallel plate waveguide setup discussed in Section 5.2 is also used for measuring the radome constructed of YBCO SRR arrays. The measurement environment needs to be cooled down to below the T_C of YBCO (≈ 88 K). For the PPW to be cooled and thermally insulated from the warmer surrounding, it is enclosed inside a stainless steel box, in which the interior is cooled by a SunPower CryoTel GT cryocooler and liquid nitrogen.

Figure 5.31 shows the cross-section sketch of the cryogenic setup along with dimensions of the various pieces. The stainless steel box provides structural stability and helps maintain the internal temperature. At the base of the box is an orifice of 47.625 mm diameter to which a NW50 flange is welded. This allows the cryocooler to be tightly attached with only the cold tip protruding into the box. As the name suggests, the cold tip is the part that gets cooled to cryogenic temperature. A 70×70 mm² of thickness 6 mm block of copper fits firmly on the cold tip. A Lakeshore temperature sensor is attached to the copper block, with the temperature being fed back to the cryocooler controller for power regulation. Not shown in the figure is a fan that cools the cryocooler.

The PPW is again formed by two single sided copper cladding FR4. Two copper plates could have been used instead. However, the heat conduction of the copper would prevent a localization of the cold temperature at the center of the PPW, where the HTS radome resides. A 70×70 mm² hole is cut at the center of the bottom FR-4 sheet, to allow the copper block to fit tightly flushed into the hole. Copper tape is lined along the sides of the square hole to ensure electrical conductivity between the copper cladding and the copper block. Thus, the holed FR-4 board together with the square copper block form a contiguous conducting plate. A thick block of Rohacell IG-71 foam is placed underneath the FR-4 sheet for structural support and used also as a thermal insulator to the base of the steel box. At low temperature, the thin sheet of FR-4 does not remain flat. Therefore it is securely adhered to the supporting foam. 10 mm height LS-24 absorbers separate the two sheets of FR-4 to form the parallel plate waveguide. The absorber helps reduce the reflection

CRYOCOOLER SETUP FOR HIGH- T_C RADOME MEASUREMENTS

By: Frank Tang, Horst Rogalla, Zoya Popović
Version: 3

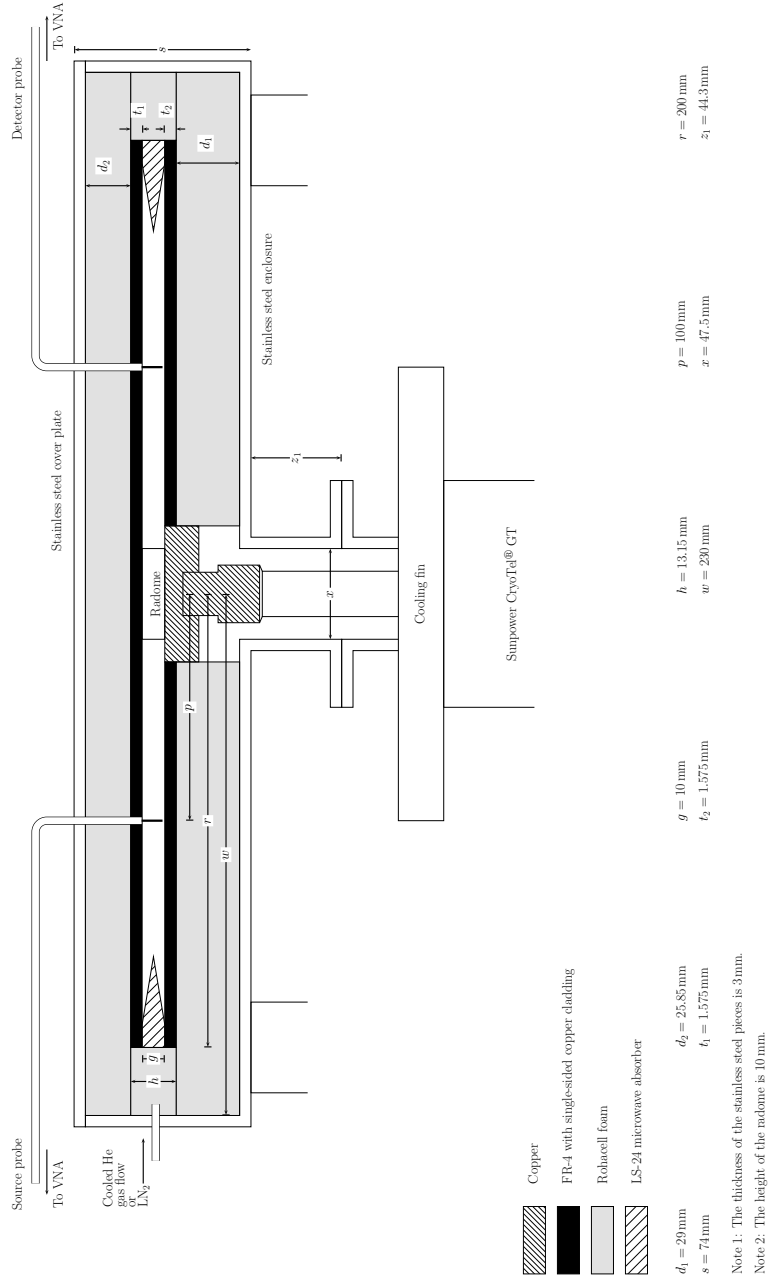


Figure 5.31: Cross section sketch of the cryogenic measurement setup. The parallel plate is enclosed inside a steel box and is cooled by a SunPower Cryotel GT cryocooler from the base of the box.

from the finite size PPW and also maintain a constant distance between the top and bottom FR-4 sheet. Another thick Rohacell foam block on the top maintains the flatness of the top FR-4 sheet and doubles as a thermal insulator. Three holes were drilled on the steel lid, top layer foam, and FR-4 sheet for the coaxial probes to be inserted into the parallel plate waveguide. The probes are connected to a VNA for measuring the transmission coefficients.

The final measurement setup is shown in Figure 5.32. For structural stability, the steel box sits firmly on a 1 inch thick slab of wood, which is bolted on two steel rails. The rail is bolted to the two cabinets. Figure 5.32b shows the setup without the top FR-4 and foam sheets. It turns out that the cryocooler in the current setup could not cool the radome to sub- T_C of YBCO. This is mainly due to the poor thermal insulation in the setup. Therefore, grooves were cut into the foam around the PPW and filled with liquid nitrogen to reduce the heat load to the cryocooler. This helped brought the whole setup to 77 K.

5.6 CRYOGENIC MEASUREMENTS

Next, the fabricated three-layer YBCO SRR radome is measured in the cryogenic setup environment. The SRR dimensions are from the optimization and shown in Table 5.1 under the YBCO columns. The inner, middle, and outer layers have 30, 36, and 42 SRR array elements, each $2.5 \times 10 \text{ mm}^2$ and consists of four 700 nm thick YBCO SRRs on a $500 \mu\text{m}$ thick MgO. Figure 5.33 shows a photograph of the HTS radome. For structural support, a sample holder was made from milling deep grooves into a Rohacell foam. First the empty parallel plate waveguide is characterized at room and cold temperature. A Line-Reflect-Line calibration is performed at room temperature to the coaxial probes, as discussed in Section 5.2. The comparison is shown in Figure 5.34. The values of the cold PPW is slightly higher than the room temperature case.

The radome was then placed at the center of the PPW for measurement. It was first measured at room temperature, with results shown in Figure 5.35. As expected, no interesting feature appeared. Next, the whole test setup, along with the radome, is cooled with the cryocooler and the LN_2 is poured into the foam grooves. Since the cryocooler utilizes a piston pump for heat rejection, a fair amount of vibration was experienced even with the additional structural stability support discussed in Section 5.5. The vibration is seen in the measurements as very rapid fluctuations in the S -parameters. Prior to recording the measurements, the

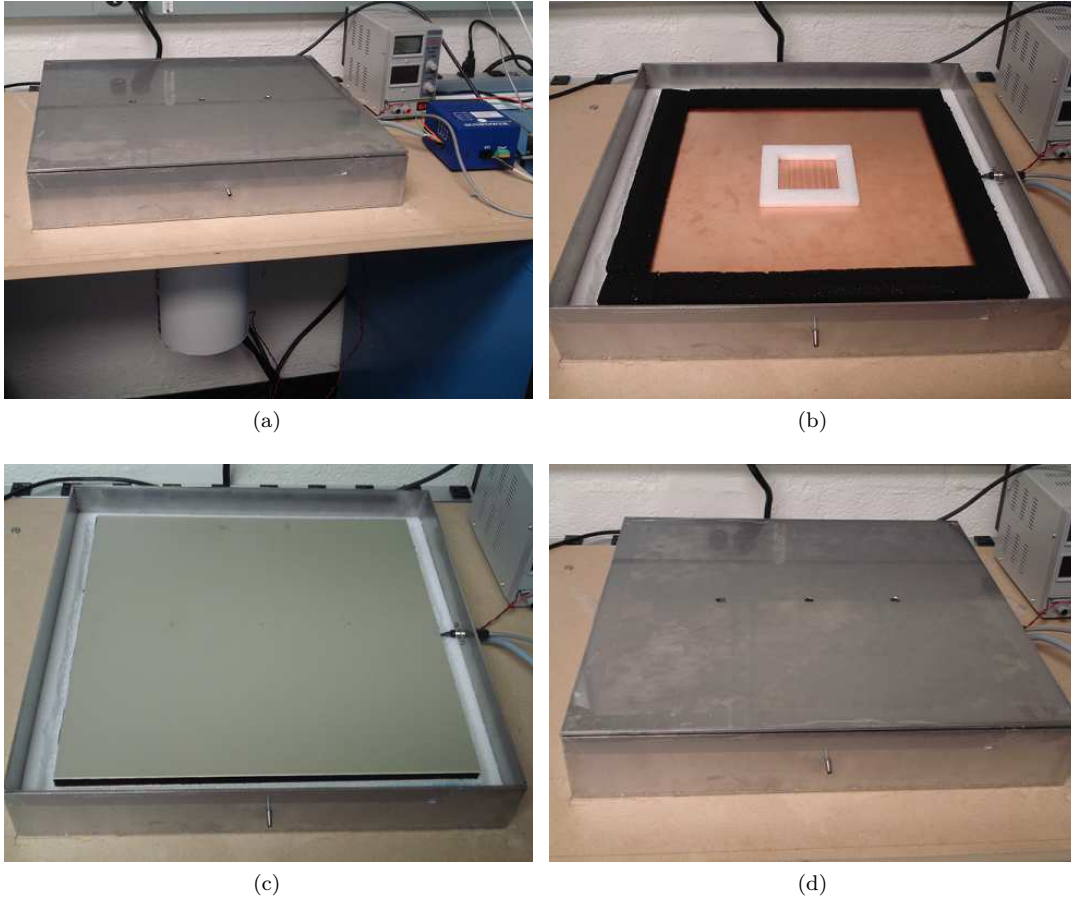


Figure 5.32: Cryogenic setup photographs of (a) the full setup, (b) the setup without the top FR-4 sheet, (c) the setup with the full PPW, and (d) the setup with the enclosing stainless steel lid.

cryocooler was shut off and the cold temperature is maintained by the heat capacitance and liquid nitrogen in the enclosed steel box. However, the cryocooler temperature was allowed to reach 77 K prior to shut down. Without the cryocooler running, the temperature reading of the setup is lost.

A series of isolation and shadowing measurements were taken at sub- T_C , shown in Figures 5.36 and 5.37, respectively. The optimal frequency of isolation shifts in Figure 5.36. This is an effect due to the temperature variation, as discussed in Section 3.4. The optimal frequency in the neighborhood of 11 GHz for reduction stays constant at ≈ 11.12 GHz. From these measurements, the optimal set is shown in Figures 5.38 and 5.39. The zoomed-in plots for the optimal set are shown in Figure 5.40. At 11.12 GHz, the isolation is ≈ 10.5 dB and the shadowing is ≈ 1.9 dB. The measurements show better isolation than both the copper and YBCO SRR radomes in the simulations. The measured shadowing is lower than the simulated YBCO SRR radome,

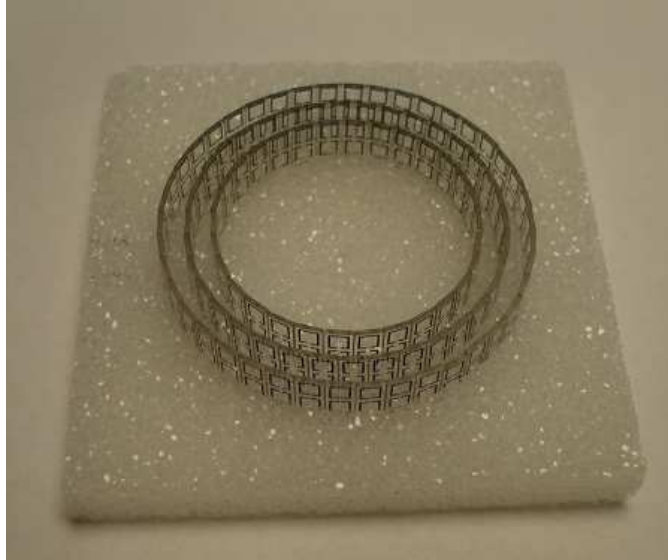


Figure 5.33: The fabricated three layer YBCO SRR on MgO radome with the optimized SRR dimensions.

but greater than the simulated copper SRR radome. The results in Figures 5.36 and 5.37 suggests that the frequency band for low shadowing is very restrictive, whereas the frequency band for high isolation is tunable. Thus, one would want to operate at the frequency with the lowest shadowing, provided that we are still in the isolation bandwidth. This work demonstrates the feasibility of fabricating a structure that provides good isolation between two antennas and low disturbance of the transmitted fields.

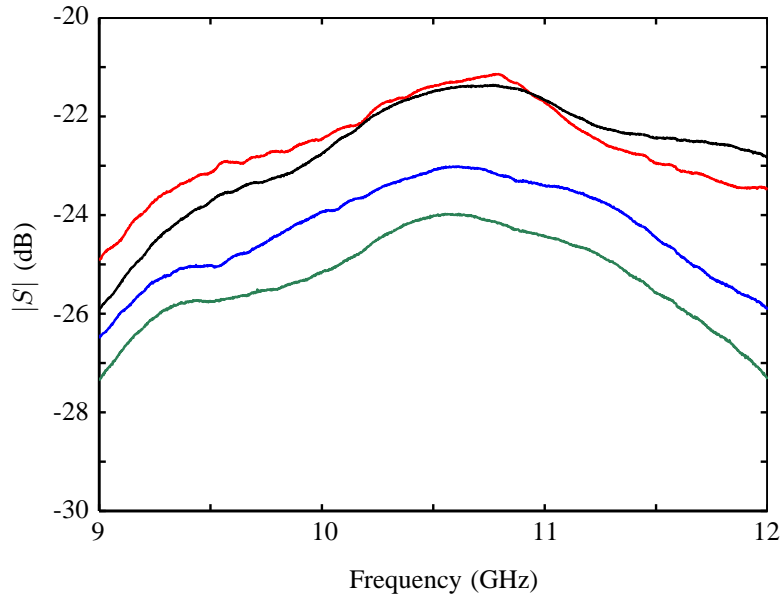


Figure 5.34: Room and cold temperature measurements of a $400 \times 400 \text{ mm}^2$ parallel plate waveguide without the radome. The black and green curves are the room temperature measurements with the transmitter and receiver probes spaced 100 mm and 200 mm apart, respectively. The red and blue curves are the corresponding cold measurements.

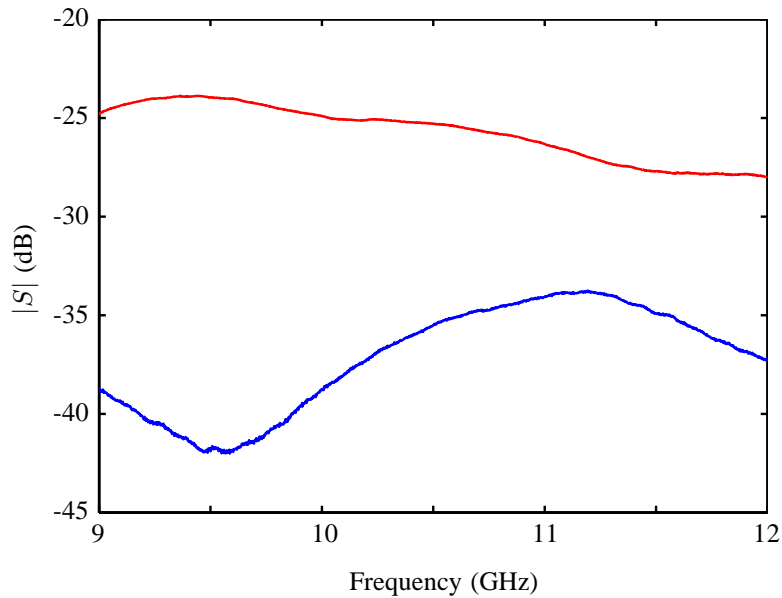


Figure 5.35: Room temperature transmission measurements of the YBCO SRR radome. The red and blue curves are the cases when the receiver probe is placed at the center of and 100 mm behind the radome, respectively.

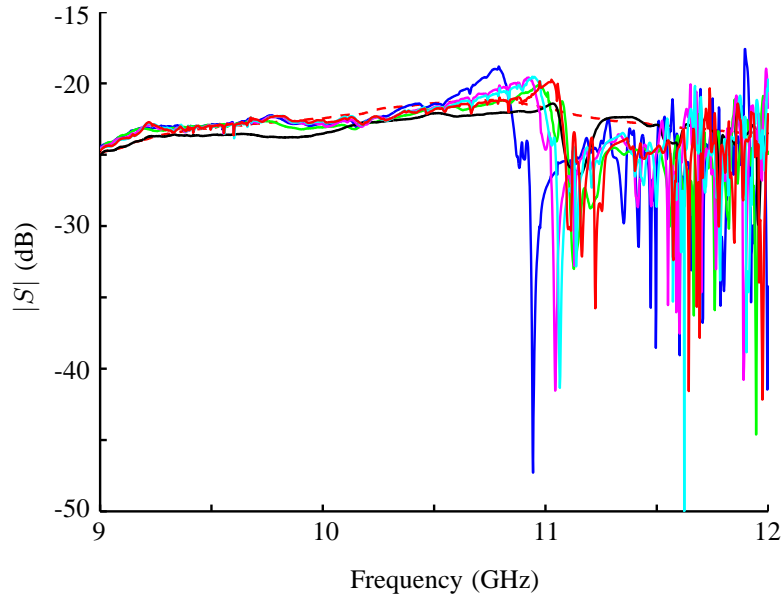


Figure 5.36: Cold temperature measurements of the YBCO SRR radome for isolation (receiver probe placed at the radome center). The dashed red curve shows the empty PPW measurement.

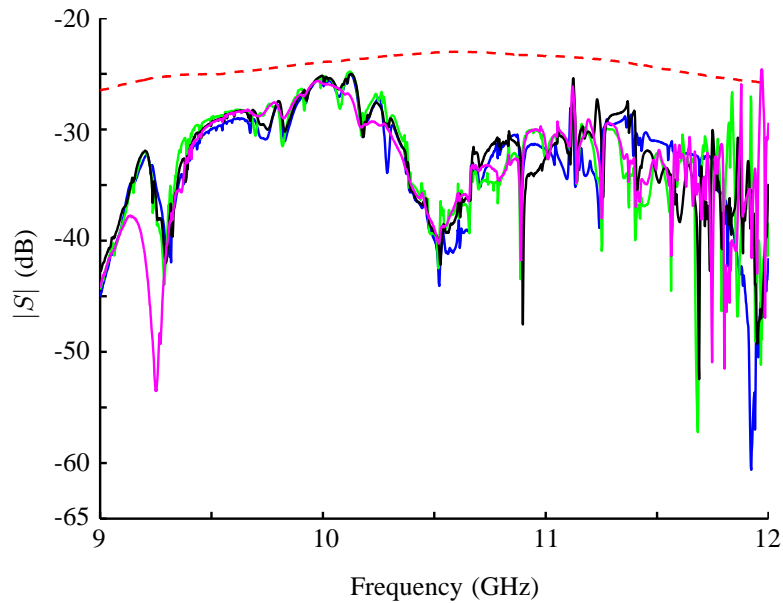


Figure 5.37: Cold temperature measurements of the YBCO SRR radome for shadowing (receiver probe placed 100 mm behind the radome). The dashed red curve shows the empty PPW measurement.

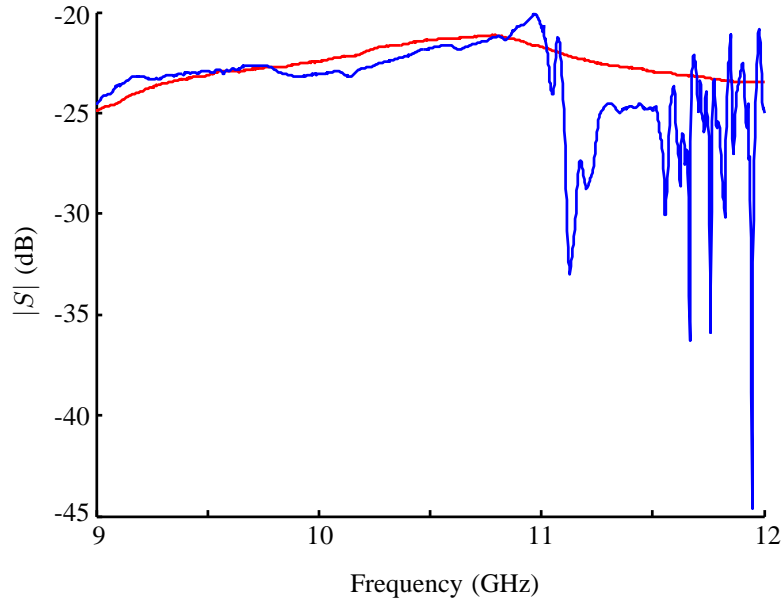


Figure 5.38: Cold temperature measurements of the YBCO SRR radome for isolation (receiver probe placed at the radome center). The dashed red curve shows the empty PPW measurement.

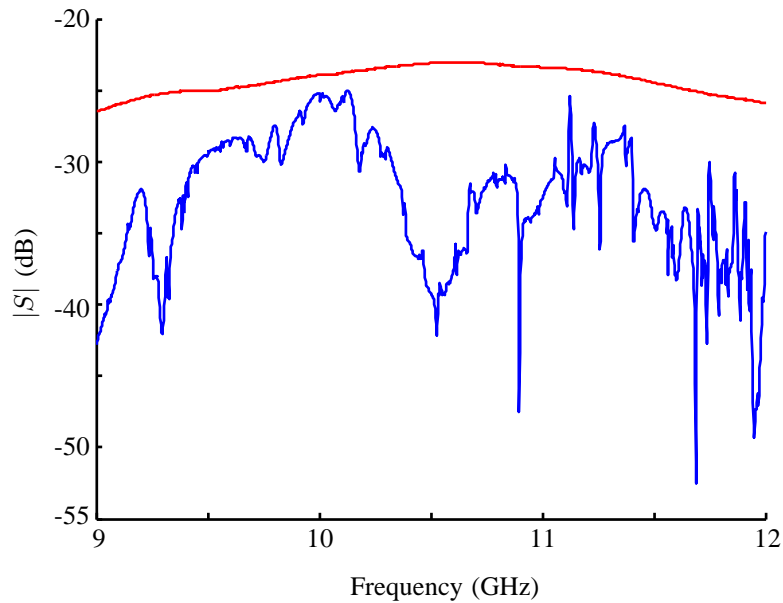
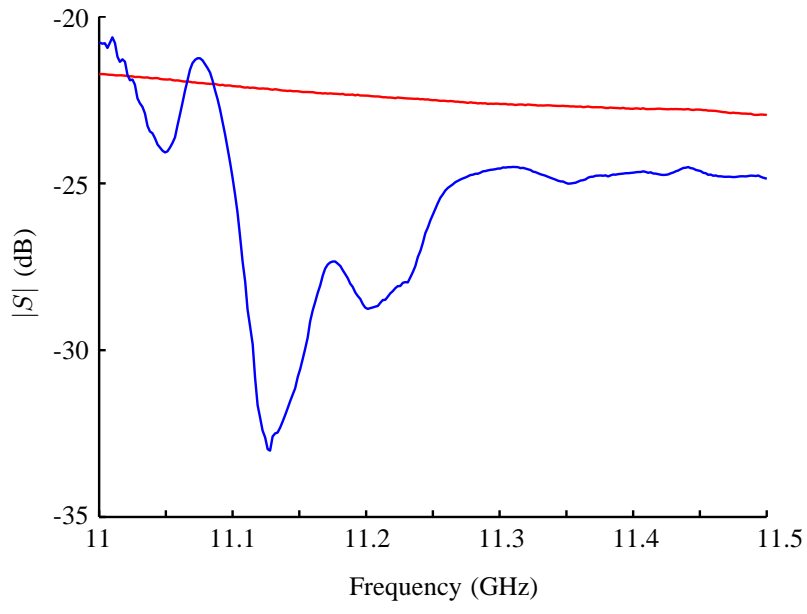
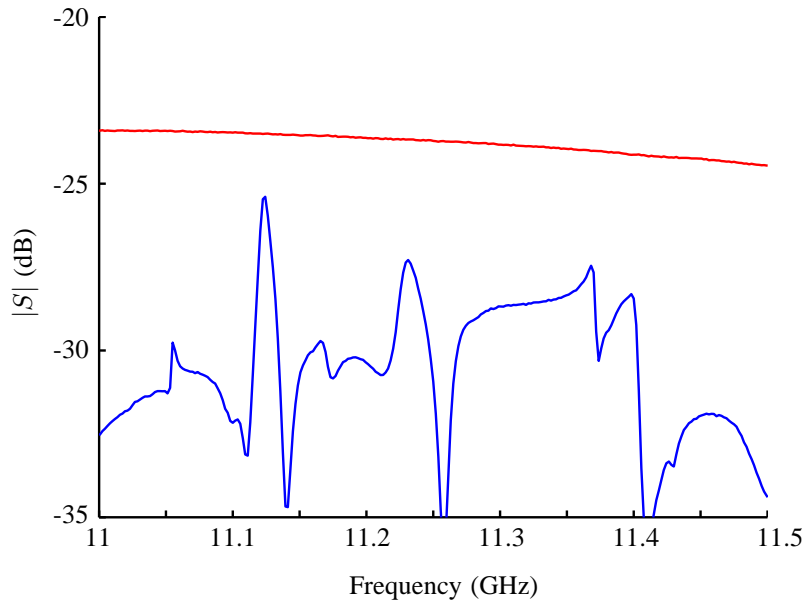


Figure 5.39: Cold temperature measurements of the YBCO SRR radome for shadowing (receiver probe placed 100 mm behind the radome). The dashed red curve shows the empty PPW measurement.



(a)



(b)

Figure 5.40: Cold temperature measurements of the YBCO SRR radome for characterizing the (a) isolation and (b) shadowing. The red and blue curves are for the empty and radome cases.

CHAPTER 6

CONCLUSIONS AND FUTURE WORK

CONTENTS

6.1	Summary and Contributions	98
6.2	Future Work	101
6.2.1	Unusual high Q -factor Resonances	101
6.2.2	Antenna Measurements	102
6.2.3	Radome and Metamaterial Geometries	103

6.1 SUMMARY AND CONTRIBUTIONS

This thesis presents the design, analysis, and characterization of a three layer cryogenic microwave metamaterial radome that provides isolation between a receiver probe/antenna and a transmitter probe/antenna. The goal of the design is to, in addition, not disturb the power transmitted to a secondary receiver behind the radome. The structure is constructed by arranging 4×1 YBCO split-ring resonator arrays in a circular pattern, as shown in Figure 5.33. The distinct steps of the presented research include:

- Theoretical analysis of the radome electromagnetic properties;
- Design of high-temperature superconducting metamaterials;

- Characterization of the HTS split-ring resonators in a cryogenic environment;
- Optimization of the SRRs for improved performance of the metamaterial radome;
- Designing the cryogenic measurement setup for characterizing the radome; and
- Fabrication of the HTS radome and quantify the isolation and distortion performance of the radome.

In Chapter 2, a derivation of the spatial dependent permeability and permittivity tensors for a cylindrical metamaterial radome in the cylindrical coordinates is presented. Because the environment for characterizing the radome is a parallel plate waveguide, the only relevant parameters are μ_r , μ_ϕ , and ϵ_z . A realizable set of parameters that has only one spatial varying term μ_r is also derived. However, this set results in a non-zero reflection coefficient. The research contribution described in this chapter is the derivation of constitutive parameters for a cylindrical cloak using coordinate transformation and the form invariance of Faraday's law. This generalizes the approach, which in the past was done using Ampere's law [17].

Chapter 3 investigates the resonant response of high-temperature superconducting split-ring resonators made of YBCO thin films deposited on single-crystal MgO substrates. The ring structures are measured inside a WR-90 X-band rectangular waveguide over a wide temperature range from 40 K to 90.5 K. An array of seven YBCO SRRs is simulated and measured inside the waveguide at 77 K, showing a stop band between 7.25 and 9 GHz.. Portions of this work were presented at the 2012 ASC [41] and published in [42]. The specific contributions in this chapter include:

- The implementation and demonstration of a cryogenic measurement setup with precise temperature control for studying the SRR resonances from room temperature down to 40 K.
- The measurements of the quality factor of HTS SRRs. The Q -factor was shown to saturate at >5000 at low temperature. In addition, a peak of ≈ 42000 was observed in a narrow temperature centered at 87 K and the result is repeatable.
- The calculation of kinetic inductance, absolute London penetration depth, and T_C of YBCO from measured temperature dependent resonant frequency of a single SRR.

- The identification of negative effective relative permittivity due to electric resonances from measured and simulated data of HTS SRRs.

Chapter 4 presents a derivation of the waveguide extraction formulae for calculating the relative permittivity and permeability diagonal tensors from the measured and simulated scattering parameters. For validation, a set of copper on Rogers 3010 substrate SRR arrays are measured inside a WR-90 waveguide and the extracted results compared with those extracted from full-wave free space simulations. A set of YBCO SRRs on MgO substrates was fabricated and characterized in the waveguide at 77 K. The contributions in this chapter are as follows:

- Extracted effective relative permeability and permittivity of YBCO SRR arrays, showing a negative real permeability μ' between 9.25 and 10.45 GHz. Generally, the imaginary part μ'' , corresponding to loss, is large in this frequency band for room temperature normal conducting SRRs. The extracted value from the HTS SRR array however shows that at frequencies above the frequency where μ' is minimum, μ'' quickly drops to near-zero, a property that is not observed in the normal conducting SRRs.
- The observation of additional high Q -factor resonances in the cryogenic measurements, accompanying the main resonances, that are not observed in normal conducting SRRs because the losses in the conductor and substrate damp them out.

Chapter 5 presents a cryogenic measurement setup for characterizing the performance of a metamaterial radome constructed of YBCO SRR arrays. The SRR dimensions are varied in simulations to maximize the isolation between a receiver probe placed at the center of the radome and transmitter probe 100 mm away, while at the same time minimizing the communication path loss between two probes 200 mm apart separated by the radome. The specific contributions in this chapter are:

- Development of a parallel plate waveguide setup to quantitatively characterize the performance of metamaterial radomes. The measurements of the bare setup and radomes, made of SRR arrays, agree with their respective HFSS simulation.
- Implementation of a cryogenic measurement setup for cooling a parallel plate waveguide to ≈ 77 K and thus cooling the structure to be measured inside the waveguide.

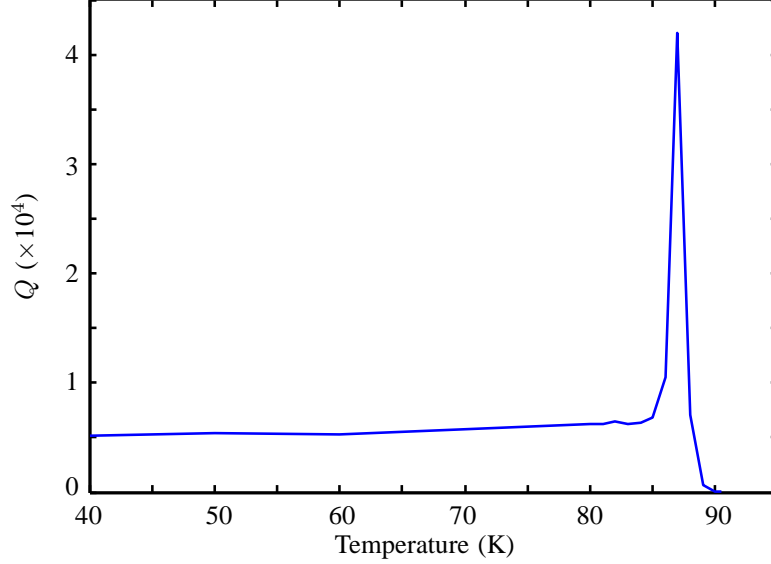


Figure 6.1: Quality factor versus temperature (K) for the measured HTS SRR inside a WR-90 waveguide. It peaks around 42000 at 87 K and saturates around 5200.

- Final demonstration of concept with measurement of a cylindrical radome with YBCO SRRs.

6.2 FUTURE WORK

6.2.1 UNUSUAL HIGH Q -FACTOR RESONANCES

In Section 3.3, the measured Q -factor of a YBCO split-ring resonator inside a WR-90 waveguide was shown to saturate at ≈ 5200 at low temperature. Our measurements have also shown that in a narrow temperature range around 87 K, the Q -factor has values ≈ 42000 , Figure 6.1. This sample was measured at different times and each time the calculated Q -factor has an unusual peak at ≈ 87 K. Thus, we conclude that this peak is not due to measurement errors.

In Section 4.5, we observed eight additional sharp resonances in addition to the main resonance for the 4×9 YBCO SRR array waveguide measurement, Figure 6.2. These sharp resonances were also seen in the low-loss simulations of this SRR array. However, they were not noticeable in the waveguide measurement of the copper sample because the losses in the conductor and substrate damped out the resonances.

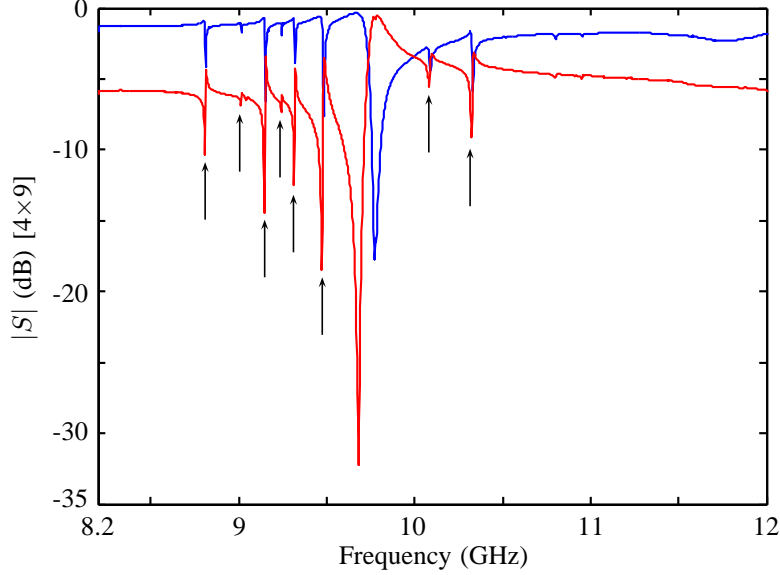


Figure 6.2: Measured reflection (S_{11} , blue curve) and transmission (S_{21} , red curve) coefficient magnitudes of the 4×9 SRR array, respectively, placed inside the waveguide section with the whole structure cooled to ≈ 76 K. The markers in (b) indicate the locations of the sharp resonances.

6.2.2 ANTENNA MEASUREMENTS

As pointed out in Chapter 1, an advantage of designing the metamaterial radome to have a cylindrical geometry is that it can be opened on the end to allow an interior antenna to be isolated from nearby transmitters in the azimuthal directions, while maintain a communication path in the perpendicular direction, as shown in the cross-section sketch in Figure 6.3. In the figure, the two monopole antennas will be able to communicate with each other without disturbing the communication between the two patch antennas, and vice versa.

Such a system would mean the radome would not be placed inside a parallel plate waveguide, but sitting on a ground plane. There are two obvious challenges for this design. First, the HTS radome would have to be cooled to a temperature below the T_C of the superconductor in a semi-opened environment. As we have seen in Chapter 5, it is already a challenge cooling the radome inside an well thermally insulated enclosure. A second challenge is ensuring diffraction resulting from a finite height of the radome does not greatly alter the characteristic of the radome. One can design a radome with more elements in the vertical direction.

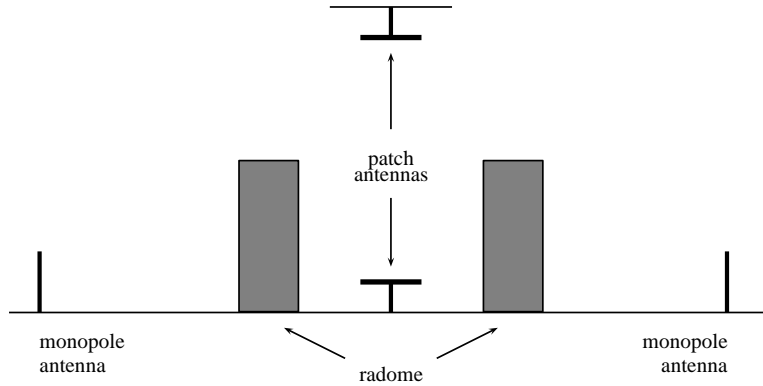


Figure 6.3: An open-top radome measurement setup for characterizing the performance of the radome for communication applications. The pair of monopole antennas and patch antennas can ideally communicate with their respective party without interference from the other pair.

6.2.3 RADOME AND METAMATERIAL GEOMETRIES

In this thesis, a cylindrical radome constructed of split-ring resonator elements was presented. One reason for the cylindrical geometry is that the realizable radome material has only a single radially varying component, $\mu_r(r)$, of near-zero values. The split-ring resonator structures have been studied extensively in the literature and the effective relative permeability has near-zero values above the magnetic plasma frequency. Thus, an obvious choice for realizing the metamaterial radome is constructing it with SRR arrays.

It is reasonable to ask whether other radome geometry, e.g. spherical or cubical, might improve the isolation and shadowing. The geometry can vary with application. A second item of interest is to study whether constructing the radome with other metamaterial structures can improve the overall performance.

APPENDIX A

FREQUENCY RESPONSE OF DOUBLE-SIDED SRR ARRAYS TO FABRICATION TOLERANCES

CONTENTS

A.1	Introduction	104
A.2	Measurements and Simulations	106
A.3	Tolerance Studies	107
A.4	Conclusion	113

A.1 INTRODUCTION

Many of the characteristic properties of metamaterials, e.g. negative effective permeability, occur at and close to the resonances of the constituent scatterers. However, for resonant structures, imperfections due to the fabrication process can greatly affect the performance. This chapter presents a study of the impact these imperfections have on the frequency response of double-sided split-ring resonator (DSRR) arrays.



Figure A.1: A DSRR array inside a WR-90 waveguide section.

The DSRR arrays are designed to be resonant at X-band and are measured inside a WR-90 rectangular waveguide, as shown in Figure A.1. The sensitivity of the frequency response to several typical fabrication and measurement errors is investigated. The dominant effect is identified and demonstrated both experimentally and in the simulations. Results from this work can be applied to other work on resonant circuits. The following imperfections are studied in detail:

- tilt of sample when placed inside the waveguide
- imperfect overlap of the two SRRs on the two sides of the substrate
- air gaps along the waveguide walls, varying line width of the copper strips
- varying substrate thickness
- permittivity inhomogeneity in the substrate
- and grooves in the substrate adjacent to the metal traces.

Simulated result of the DSRR array of nominal design dimensions is compared with those from measurements, which show that relatively minor errors and fabrication tolerances, which are sometimes overlooked, can have a large effect on the resonant frequency.

Wang *et al.* [70] in 2009 showed that broadband planar left-handed metamaterials can be achieved by using pairs of SRRs. We adapted this design, utilizing its symmetry, into our DSRRs and tolerance studies. The relevant dimensions of each unit cell are labeled and shown in Figure A.2. Each DSRR is made up of $35\ \mu\text{m}$ (1 oz.) thick copper rings on the two opposite sides of a $h=762\ \mu\text{m}$ thick slab of Rogers 4350B substrate, which has a nominal relative permittivity $\epsilon_r=3.66$, [71] Figure A.3. Five 2x4 arrays of DSRRs, referred to

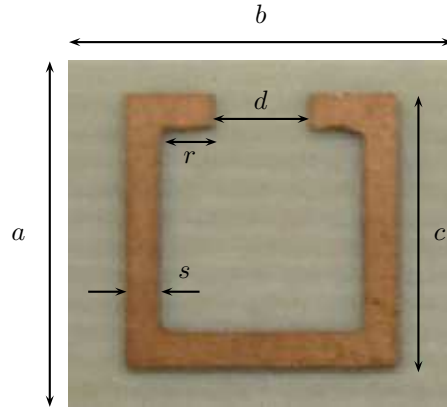


Figure A.2: Photo of unit cell with labeled dimensions.

as DSRR1–DSRR5, each consisting of eight unit cells with the vertical periodicity of 5.08 mm and lateral periodicity of 5.715 mm, were fabricated. This was done to allow an integer number of the DSRRs to fit inside a standard WR-90 waveguide. Each DSRR array was fabricated with a LPKF ProtoMat S62 printed circuit board (PCB) milling machine that is only capable of milling one side at a time. In order to assure that a ring on one side overlaps the corresponding ring on the opposite side, alignment holes were drilled, which were used as reference points when milling the opposite side.

A.2 MEASUREMENTS AND SIMULATIONS

The DSRR structure placed inside a WR-90 waveguide was simulated in Ansys HFSS™ (HFSS), a FEM solver, with the simulated reflection (S_{11}) and transmission (S_{21}) coefficient magnitudes shown as solid blue curves in Figure A.4. The Agilent E8364B programmable network analyzer (PNA) was calibrated from 8.2–12.4 GHz using the WR-90 Maury Microwave waveguide Short-Short-Load-Thru (SSLT) calibration standards. The five DSRR arrays were then measured separately. Figure A.5 shows the measured $|S_{21}|$ for each of the five arrays, showing a 380 MHz variation which can only be attributed to variations in fabrication. The S -parameters for DSRR1 is also plotted together with the simulation in Figure A.4. Rather surprisingly, we observed a 580 MHz, or 6.3%, upward shift in resonance frequency of the transmission coefficient relative to the simulation. This discrepancy is not expected and can be due to either simulation, measurement, or fabrication errors. HFSS, being a FEM solver, is well suited for closed structures and our experience is that

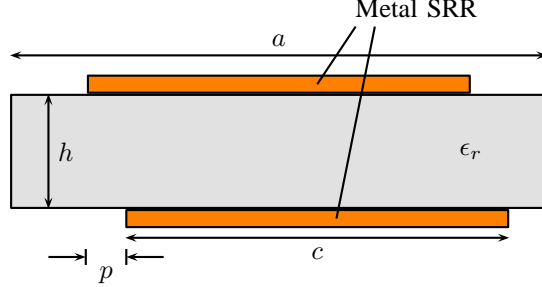


Figure A.3: Side view of a unit cell (not drawn to scale).

we can trust the simulation. The excitation for the simulation were waveports and the meshing was varied to check for convergence.

A.3 TOLERANCE STUDIES

The two practical sources of errors can be divided into measurement errors (calibration and misalignment) and fabrication errors. To rule out calibration errors, two separate calibration methods were employed: a standard TRL method using standard waveguide parts in the lab and a SSLT method using Maury X7005S calibration standards. Measurements of the sample after each calibration show the S_{21} nearly overlapping, and thus ruling out calibration errors. Another measurement error is a possible tilt of the structure inside the waveguide. With a large tilt of 10° introduced in the measurement of the DSRR4 sample, there is a slight shift (0.4%) in the resonance. However, it does not explain the major shift in the main resonance.

Several obvious fabrication errors include: (1) Imperfectly overlapping rings, described by p in Figure A.3; (2) An air gap along the waveguide walls; (3) Varying line width of the copper strip; (4) Varying substrate thickness; and (5) Permittivity inhomogeneity of the substrate sheet. For the fabrication techniques used in this work, typical deviations were taken into account to simulate their effects on the resonance frequency, as summarized in Table A.1. The following conclusions can be made:

- Misalignment between the front and back side split-rings, described by the overlap p , does not cause significant shift in the resonant frequency.
- Air gaps along the top and bottom wall has a dominating effect over the gaps along the side walls a TE_{10} wave mode excitation since the electric fields go to zero on the side walls. When an air gap as

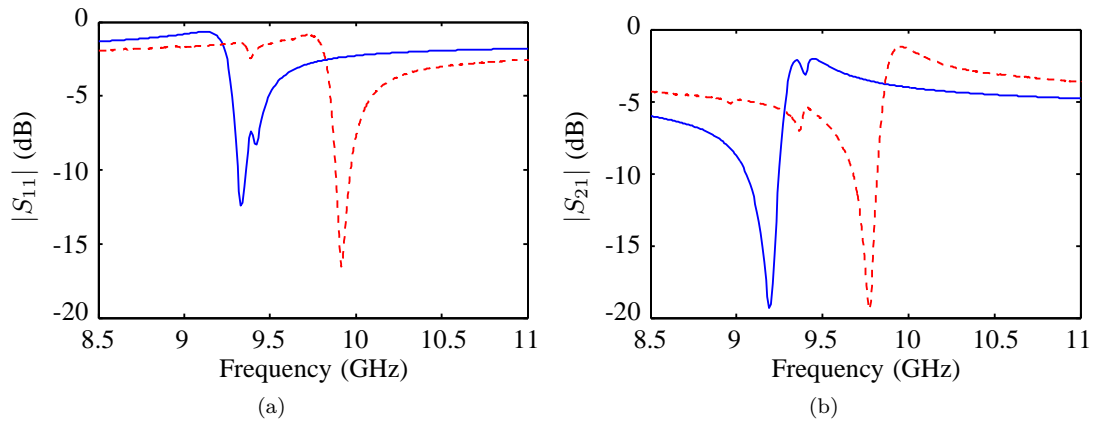


Figure A.4: Simulated and measured reflection (a) and transmission (b) coefficient magnitudes of the DSRR1 array inside the waveguide. The solid blue and dashed red curves are from the simulations and measurements, respectively.

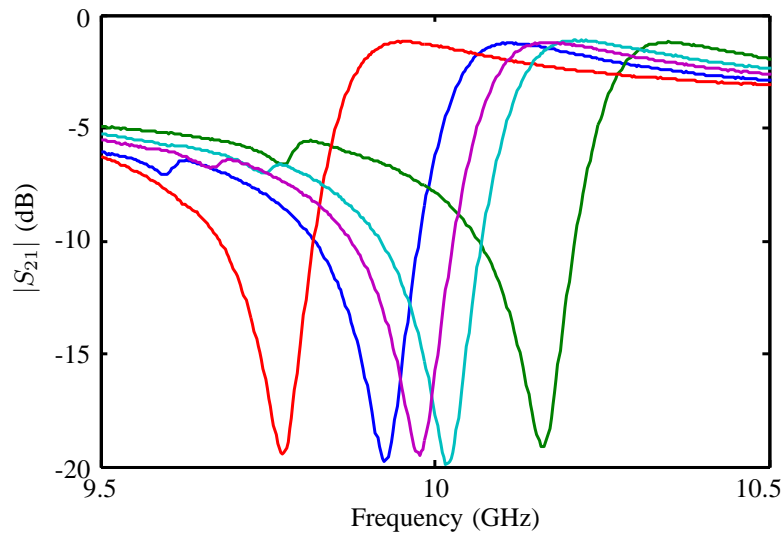


Figure A.5: Measured transmission coefficients for DSRR1–DSRR5 (with minima ordered left to right).

Table A.1: Fabrication imperfections and their effects on the resonant frequency. (V—vertical offset, H—horizontal offset)

Parameters	Value	f_r (GHz)	% Shift
Overlap Offset p (μm)	40 (V)	9.22	+0.33
	80 (V)	9.14	-0.54
	50 (H)	9.18	-0.11
	100 (H)	9.07	-1.31
Line Width s (mm)	0.45	9.2	+0.11
	0.55	9.09	-1.09
Substrate Thickness h (μm)	750	9.19	0
	780	9.14	-0.54
Relative Permittivity ϵ_r	3.5	9.2	+0.11
	3.8	9.06	-1.41

large as $150\ \mu\text{m}$ was introduced in simulation, the resonance frequency shifted by only 0.65%.

- The 0.5-mm line width can vary if the milling bit is dulled after extended use. A $50\ \mu\text{m}$ increase in width shifts the resonance upward by 0.11%, while a $50\ \mu\text{m}$ decrease shifts it downward by 1.1%.
- For a large sheet of substrate, there will likely be areas where the sheet is thinner or thicker than the manufacturer’s specified value. Thus, the thickness of the substrate was varied by $+18\ \mu\text{m}$ and $-12\ \mu\text{m}$ in the simulations. The tabulated results in Table A.1 show the resonance was effected by at most 0.5%.
- The permittivity has been shown to vary across a substrate sheet, e.g. [72], [73]. The nominal permittivity value for the Rogers 4350B substrate used was given by the manufacturer datasheet as 3.66. In the simulations, this value was varied between 3.5 and 3.8, and resulted in a shift of the resonance by as much as 1.41%. Table A.1 summarizes the effects of this deviation.

For further verification, a test structure of microstrip lines was milled on the same sheet of substrate used for the DSRR array, Figure A.6. By measuring the phase difference of two lines, the relative permittivity were extracted, [74] with an average value of 3.65.

$$\epsilon_{\text{eff}} = \left(\frac{c\Delta\phi}{2\pi f(\Delta l_p)} \right)^2 \quad (\text{A.1})$$

where c is the speed of light in vacuum, $\Delta\phi$ is phase difference of the two lines, and Δl_p is the physical length difference of the two lines. The quasistatic relative dielectric constant can then be solved using

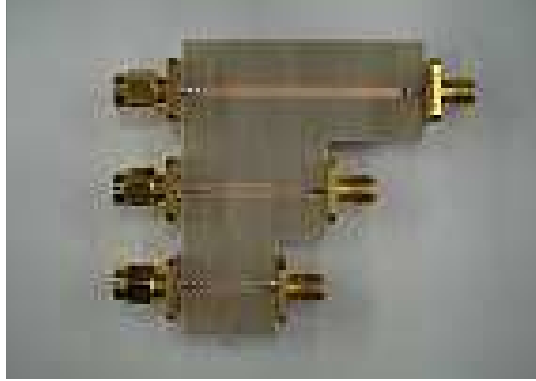


Figure A.6: Microstrip lines for measuring the relative permittivity of the substrate.

the formula

$$\epsilon_{\text{eff}} = \frac{\epsilon_r + 1}{2} + \frac{\epsilon_r - 1}{2} \frac{1}{\sqrt{1 + 12h/w}} \quad (\text{A.2})$$

In summary, none of the obvious fabrication or measurement errors account for more than 1.41% of the resonance shift in the worst case, indicating that there is some discrepancy that we have not yet taken into account. A closer examination of the fabricated DSRR structure shows the milling job left grooves in the substrate adjacent to the metal trace, as shown in Figure A.7. There has been some previous work [75–77] reporting a change in effective permittivity of planar transmission lines when grooves are present on the substrate. However, the work presented in these papers is on guided wave (microstrip) structures and very different in nature from the work discussed in our paper. It is not possible to carry over conclusions directly from a guided wave structure to a free-space structure; one involves a change in phase velocity, while the other is effectively a change in the resonant lumped element shunt loading of a waveguide. Nevertheless, we examined a section of the SRR through a microscope, and observed grooves, as shown in Figure A.7. The grooves around the copper ring edges have a width approximately equal to the width of the milling bit ($254 \mu\text{m}$) and a depth approximately three times the thickness of the copper ($3 \times 35 \mu\text{m}$). We expected that these minor imperfections might play some role in altering the reflection and transmission responses of the DSRR array, but as shown below, they turned out to be the main factor in the shifting of the resonances. A nice PCB fabrication guideline by Trescases [78] discusses the procedure for adjusting the proper depth of the milling bit, thus reducing the depth of the grooves.

In the simulation, the nominal design was modified to include a groove width of $254 \mu\text{m}$ and a depth of

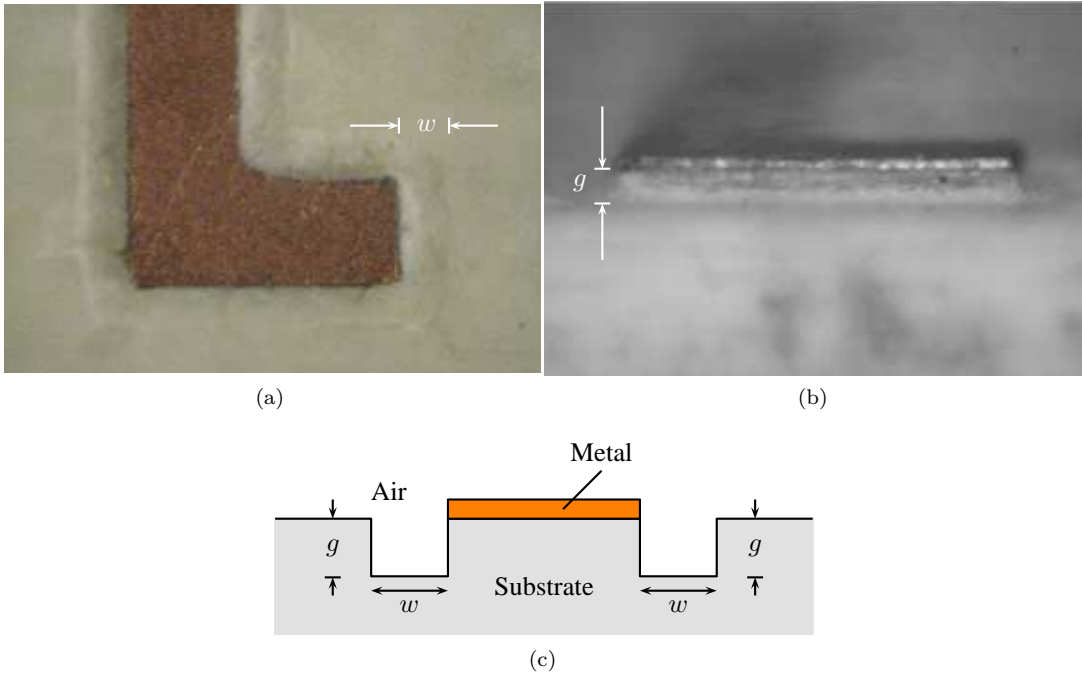


Figure A.7: Microscope photographs showing the width ($w \approx 254 \mu\text{m}$) and depth ($g \approx 105 \mu\text{m}$) of a groove from the top (a) and side (b). The sketch in (c) shows a cross-section with relevant dimensions (not to scale).

$107 \mu\text{m}$ gives the best agreement with the experimental results. The new scattering parameter are compared to the measurement in Figure A.8, showing the two curves overlap closely. We can therefore conclude that the 6.3% shift of the resonance frequency is caused primarily by the presence of the grooves.

We further studied the frequency responses resulting from varying the groove width and depth, with the results summarized in Table A.2. The values chosen are comparable to the size of milling bits commonly available. The results show that increasing either the width or the depth of grooves shifts the resonant frequency to higher values.

To show that the impact of the grooves is not only seen in the DSRR arrays, a single-sided SRR structure with the same dimensions as those of the DSRRs was also studied through simulations. We expect the grooves in this structure to shift the resonance higher in frequency. First the structure without the grooves is simulated, with the results shown as solid blue lines in Figure A.9. Next, grooves with width $w=254 \mu\text{m}$ and depth $g=107 \mu\text{m}$ were added adjacent to the copper traces, with the results shown as the dashed red lines in Figure A.9. The new simulation shows 6.2% and 6.1% upward shifts in the reflection and transmission resonant frequency, respectively. From the results, we can make a stronger case that the effect of the grooves

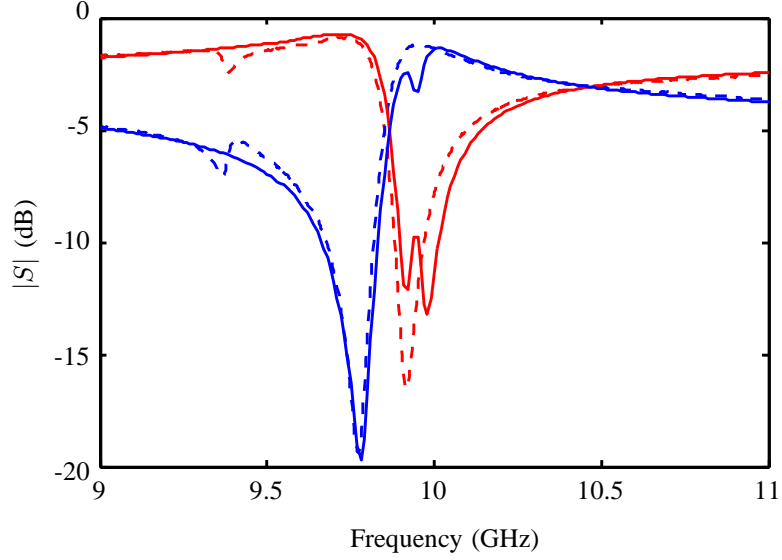


Figure A.8: The measured transmission (dashed blue) and reflection (dashed red) coefficients shown together with the simulation (solid lines) for DSRR1, which includes identical grooves on both sides with a groove width $w=254\ \mu\text{m}$ and depth $g=107\ \mu\text{m}$. The ring dimensions are as specified in section A.1 with $a=5.08\ \text{mm}$, $b=5.715\ \text{mm}$, $c=4\ \text{mm}$, $d=1.4\ \text{mm}$, $r=0.8\ \text{mm}$, $s=0.5\ \text{mm}$.

Table A.2: Resonant frequencies with varied groove dimensions

Depth g (μm)	Width w (μm)	f_r (GHz)
50.8	127	9.48
50.8	254	9.54
76.2	127	9.58
76.2	254	9.66
107.0	254	9.78

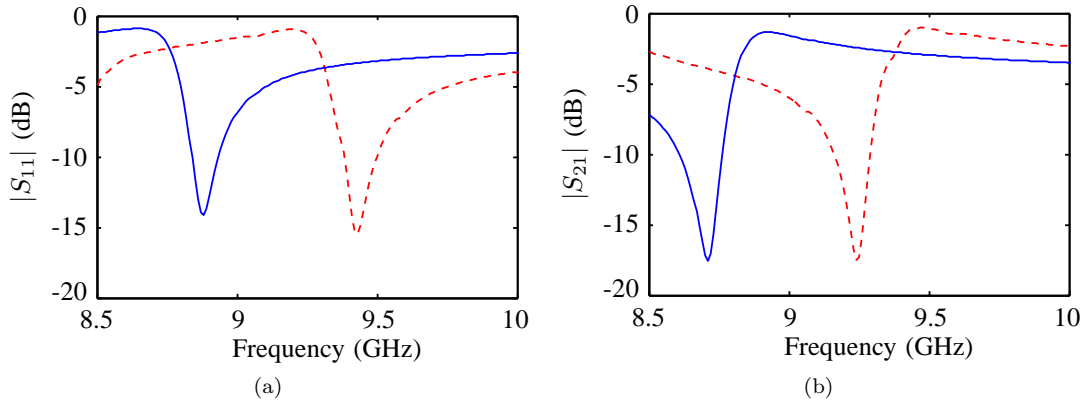


Figure A.9: Simulated reflection (a) and transmission (b) coefficient magnitudes of a single-sided SRR array with (dashed red) and without (solid blue) the grooves adjacent to the copper traces inside the waveguide.

is not confined only to the DSRR design, but can be seen in other resonant circuits.

A.4 CONCLUSION

We have discovered that grooves in the dielectric substrate caused by a milling procedure can result in large changes in the resonant frequency of a planar array of DSRRs. Although some previous researchers have found small effects of grooves in the substrate surface, our work demonstrated that resonances can be dramatically altered by this seemingly minor deviation from the design. This illustrates the importance of very precise modeling whenever such resonant behavior is present.

APPENDIX B

EFFECTIVE PARAMETER

EXTRACTION FROM

S-PARAMETERS

CONTENTS

B.1	Extraction Method For Isotropic, Homogeneous Materials	114
-----	--	-----

B.1 EXTRACTION METHOD FOR ISOTROPIC, HOMOGENEOUS MATERIALS

This section presents the retrieval of the effective relative permittivity and permeability from the reflection and transmission coefficients. The resulting equations were original presented by Nicholson and Ross [61]. The procedure begins with a homogeneous slab of isotropic material, of length d , being modeled as a section of a transmission line with the characteristic impedance Z_1 , as shown in Figure B.1, sandwiched between two transmission lines of infinite extend with characteristic impedance of Z_0 .

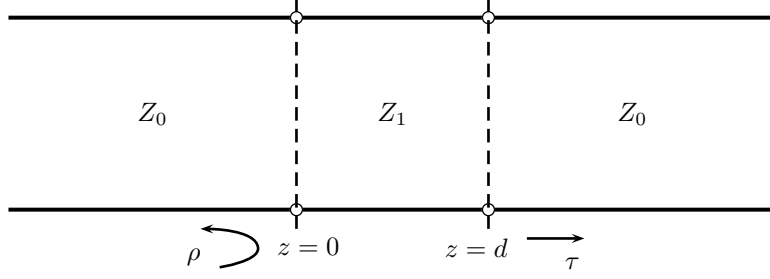


Figure B.1: Transmission line model of an isotropic, homogeneous slab of dielectric.

The reflection coefficient, ρ or S_{11} , is therefore

$$\begin{aligned}
 S_{11} = \rho &= \frac{Z_{\text{in}} - Z_0}{Z_{\text{in}} + Z_0} \\
 &= \frac{(1 - e^{-j2k_0nd})\Gamma}{1 - \Gamma^2 e^{-j2k_0nd}}
 \end{aligned} \tag{B.1}$$

where n is the effective refractive index and Γ is the reflection coefficient at the boundary if the slab extends infinitely to the right

$$\Gamma = \frac{Z_1 - Z_0}{Z_1 + Z_0} \tag{B.2}$$

Using the ABCD matrix equations discussed in [79], the total voltages of the line at distance $z = d$ and distance $z = 0$ are related by

$$\begin{aligned}
 \frac{V(d)}{V(0)} &= \frac{V(d)}{A(0, d)V(d) + B(0, d)I(d)} \\
 &= \frac{Z_0}{Z_0 \cos \beta d + jZ_1 \sin \beta d}
 \end{aligned} \tag{B.3}$$

The transmission coefficient, τ or S_{21} , can then be found by using this voltage relationship and ρ found earlier.

$$\begin{aligned}
S_{21} = \tau &= \frac{V(d)}{V_o^+} \\
&= \frac{V(d)}{V(0)}(1 + \rho) \\
&= \frac{Z_0}{Z_0 \cos \beta d + j Z_1 \sin \beta d} \left[\frac{2Z_1 Z_0 \cos \beta d + j 2Z_1^2 \sin \beta d}{2Z_0 Z_1 \cos \beta d + j(Z_1^2 + Z_0^2) \sin \beta d} \right] \\
&= \frac{2Z_1 Z_0}{2Z_0 Z_1 \cos \beta d + j(Z_1^2 + Z_0^2) \sin \beta d} \\
&= \frac{4Z_1 Z_0}{(Z_1^2 + Z_0^2 + 2Z_1 Z_0)e^{j\beta d} - (Z_1^2 + Z_0^2 - 2Z_1 Z_0)e^{-j\beta d}} \\
&= \frac{4Z_1 Z_0}{(Z_1 + Z_0)^2} \frac{e^{-j\beta d}}{1 - \Gamma^2 e^{-j2\beta d}} \\
&= \frac{(1 - \Gamma^2)e^{-j\beta d}}{1 - \Gamma^2 e^{-j2\beta d}} \\
&= \frac{(1 - \Gamma^2)e^{-jk_0 n d}}{1 - \Gamma^2 e^{-j2k_0 n d}} \tag{B.4}
\end{aligned}$$

In the above expression, V_o^+ represents the forward incident wave at the first boundary. Equation (B.4) can also be derived using the ‘‘Multiple Reflection’’ technique presented in Pozar’s *Microwave Engineering* [80].

The scattering coefficients S_{11} and S_{21} can be inverted to give

$$\Gamma = \frac{S_{11}^2 + 1 - S_{21}^2}{2S_{11}} \pm \sqrt{\left(\frac{S_{11}^2 + 1 - S_{21}^2}{2S_{11}}\right)^2 - 1} \tag{B.5}$$

$$P \equiv e^{-jk_0 n d} = \frac{S_{21} + S_{11} - \Gamma}{1 - (S_{21} + S_{11})\Gamma} \tag{B.6}$$

The sign in Equation (B.5) is chosen such that $|\Gamma| \leq 1$. The slab’s normalized wave impedance (η_r), index of refraction (n), complex relative permittivity (ϵ_r), and complex relative permeability (μ_r) are obtained by

$$\eta_r = \sqrt{\frac{\mu_r}{\epsilon_r}} = \left(\frac{1 + \Gamma}{1 - \Gamma}\right) \tag{B.7}$$

$$n = \sqrt{\mu_r \epsilon_r} = \frac{1}{k_0 d} \left(\text{Im} \left[\ln \frac{1}{P} \right] + 2\pi m \right) - \frac{j}{k_0 d} \text{Re} \left[\ln \frac{1}{P} \right] \tag{B.8}$$

$$\epsilon_r = \frac{n}{\eta_r} \tag{B.9}$$

$$\mu_r = \eta_r n \tag{B.10}$$

where k_0 is the vacuum wave number and m is an integer constant. The real part of the refractive index has an ambiguity of $2\pi m$ that generally cannot be easily resolved. Alternatively, the normalized wave impedance can be found to be

$$\eta_r = \pm \sqrt{\frac{S_{21}^2 - (S_{11} + 1)^2}{S_{21}^2 - (S_{11} - 1)^2}} \quad (\text{B.11})$$

where the sign is chosen such that $\text{real}(\eta_r) \geq 0$.

APPENDIX C

COORDINATE TRANSFORMATION

BACKGROUND

CONTENTS

C.1	Coordinate Transformation Background Mathematics	118
-----	--	-----

C.1 COORDINATE TRANSFORMATION BACKGROUND MATHEMATICS

In this section, the relevant mathematical definitions and formulae are presented to assist the constitutive parameter transformations discussion in Chapter 2. Let us first introduce the concept of an original and a transformed space, where each space can be expressed in a Cartesian coordinate system and a curvilinear coordinate system. The concept of the two spaces are adapted from the discussion of physical and virtual spaces presented in Zhang's doctoral thesis [17] and by Ward. [15] The transformed and original space coordinates are represented by the prime and non-prime notation, respectively, and are related by

$$\mathbf{r}' = \mathbf{r}'(\mathbf{r}) \tag{C.1}$$

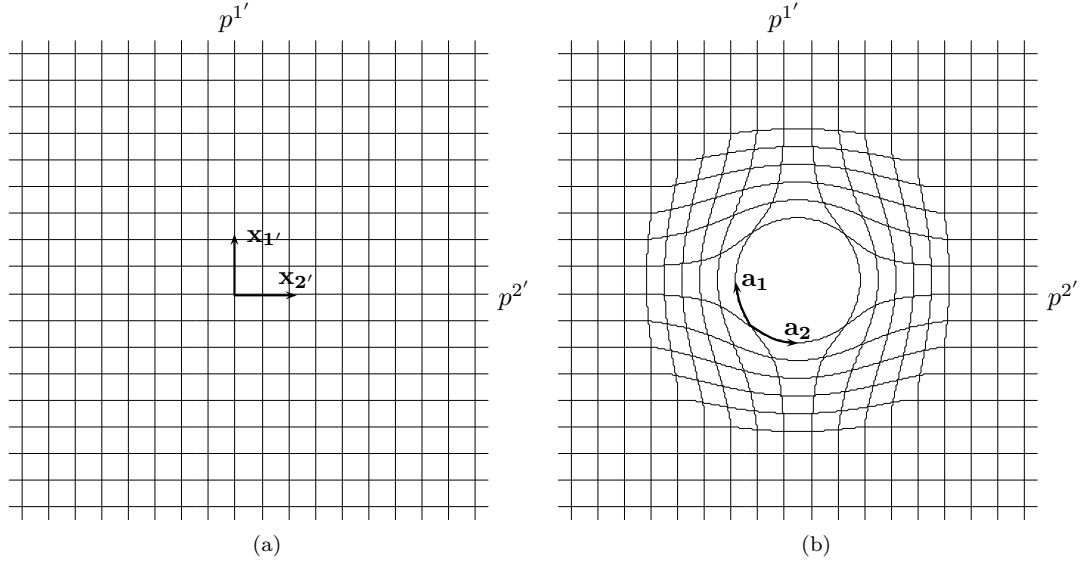


Figure C.1: (a) Transformed Cartesian (b) Original curvilinear

where $\mathbf{r}' = p^{i'} \mathbf{x}_{i'}$ and $\mathbf{r} = p^i \mathbf{x}_i$ are the position vectors in the coordinate system. Equation (C.1) states that variables in the transformed space can be expressed in terms of those in the original space and vice versa. The superscript and subscript of the same index seen together indicates a summation over all indices, written with the Einstein summation notation. For example,

$$S = a^1 x_1 + a^2 x_2 + a^3 x_3 = \sum_{i=1}^3 a^i x_i = a^i x_i \quad (\text{C.2})$$

Now allow the Cartesian coordinates in the transformed space and the curvilinear coordinates in the original space to be defined as shown in Figure C.1. From Equation (C.1), variables of the original space, \mathbf{r} , can be written as functions of those in the transformed space, $p^{i'}$, and vice versa. Thus, variables of the original space curvilinear coordinates can be written as functions of $p^{i'}$. Then the set of basis vectors of the curvilinear space is given as

$$\mathbf{a}_i = \frac{\partial \mathbf{r}}{\partial p^{i'}} \quad (\text{C.3})$$

These basis vectors need not have unit length, nor be orthogonal.

The Cartesian coordinates basis vectors, \mathbf{x}_i , of the original space can be expressed in terms of the basis vectors in the curvilinear coordinates by using the chain rule

$$\mathbf{x}_i = \frac{\partial \mathbf{r}}{\partial p^i} = \frac{\partial \mathbf{r}}{\partial p^{j'}} \frac{\partial p^{j'}}{\partial p^i} = \frac{\partial p^{j'}}{\partial p^i} \mathbf{a}_j = \Lambda_i^{j'} \mathbf{a}_j \quad (\text{C.4})$$

where the Jacobian matrix and its inverse are written as

$$\mathbf{\Lambda} = \left(\Lambda_i^{j'} \right) = \left(\frac{\partial p^{j'}}{\partial p^i} \right) \quad (\text{C.5})$$

$$\mathbf{\Lambda}^{-1} = \left(\Lambda_{j'}^i \right) = \left(\frac{\partial p^i}{\partial p^{j'}} \right) \quad (\text{C.6})$$

with the paratheses $()$ denoting a matrix. Transformation from the Cartesian system to the curvilinear system is thus

$$\mathbf{a}_i = \frac{\partial p^j}{\partial p^{i'}} \mathbf{x}_j = \Lambda_{i'}^j \mathbf{x}_j \quad (\text{C.7})$$

The differential change of the position vector, $d\mathbf{r}$, is given by

$$d\mathbf{r} = \frac{\partial \mathbf{r}}{\partial p^{i'}} dp^{i'} = \mathbf{a}_i dp^{i'} \quad (\text{C.8})$$

The definition of $d\mathbf{r}$ does not change with coordinate system and can be written in the Cartesian coordinates as

$$d\mathbf{r} = \mathbf{x}_i dp^i = \Lambda_i^{j'} \mathbf{a}_j dp^{i'} = \mathbf{a}_j \Lambda_i^{j'} dp^i \quad (\text{C.9})$$

which together with equation (C.8) give us the relationship

$$dp^{i'} = \Lambda_j^{i'} dp^j \quad (\text{C.10})$$

Quantities of the transformed and original spaces are now connected by the transformations described in (C.7) and (C.10). Components that transform as those of (C.7) and (C.10) are referred to as covariant and contravariant components, respectively. By convention, we use subscript and superscript indices to distinguish between the two. Quantities that obey these transformation rules are known as tensors. A detailed discussion on tensor is well presented in Synge and Schild [46] and Dalarsson and Dalarsson [47].

One final quantity that needs to be introduced is the metric tensor. The differential length, ds , is related to the differential position vector by

$$(ds)^2 = d\mathbf{r} \cdot d\mathbf{r} = \mathbf{a}_i \cdot \mathbf{a}_j dp^{i'} dp^{j'} = \mathbf{a}^i \cdot \mathbf{a}^j dp_i dp_j \quad (\text{C.11})$$

$$= g_{ij} dp^{i'} dp^{j'} = g^{ij} dp_i dp_j \quad (\text{C.12})$$

where g_{ij} and g^{ij} are the components of the metric tensors for the original curvilinear system. They are functions that define how distance is measured. For orthogonal coordinate systems, the metric tensors have only diagonal components and is related to the scale factor, \mathbf{h} , as

$$h_i = \sqrt{g_{ii}} \tag{C.13}$$

As an example, the cylindrical coordinate system, which is orthogonal, has a scale factor $\mathbf{h} = [1, r, 1]$, so that the value $(ds)^2$ is

$$\begin{aligned} (ds)^2 &= h_1^2 dp_1^2 + h_2^2 dp_2^2 + h_3^2 dp_3^2 \\ &= dr^2 + r^2 d\phi^2 + dz^2 \end{aligned}$$

APPENDIX D

MATLAB CODE (SPACE TRANSFORMATIONS)

CONTENTS

D.1 Matlab Code (Space Transformations) 122

D.1 MATLAB CODE (SPACE TRANSFORMATIONS)

This section contains matlab code for generating Figure 2.2.

```
1 % Frank Trang
2 %
3 % polar_cloak.m
4 %
5 % cart to polar to cart plot
6 %
7 % coordinate transformation
8
9 clear all
10 r1 = .254;
11 r2 = .762;
12
13 x = -.762*1.5:0.001:.762*1.5;
14 y = x;
15
16 Xx = zeros(18, length(x), 1);
17 Yx = zeros(18, length(y), 1);
18 Xy = Xx;
19 Yy = Yx;
20 xones = ones( length(x), 1 );
21 yones = ones( length(y), 1 );
22 xm = -.762*1.5+.0635;
23 ym = -.762*1.5+.0635;
24
```

```

25
26 for m=1:18
27     Xx(m, :, :) = xm*xones;
28     [thx, rhx] = cart2pol(Xx(m, :, :), y);
29     rhxx = (r2-r1)*rhx/r2 + r1;
30
31     Yy(m, :, :) = ym*yones;
32     [thy, rhy] = cart2pol(x, Yy(m, :, :));
33     rhyy = (r2-r1)*rhy/r2 + r1;
34
35     for n=1:length(rhxx)
36         if rhxx(n) > r2
37             rhxx(n) = rhx(n);
38         end
39         if rhyy(n) > r2
40             rhyy(n) = rhy(n);
41         end
42     end
43     [Xx(m, :, :), Yx(m, :, :)] = pol2cart( thx, rhxx );
44     [Xy(m, :, :), Yy(m, :, :)] = pol2cart( thy, rhyy );
45     xm = xm + .127;
46     ym = ym + .127;
47 end
48
49 figure
50 hold on
51 for m=1:18
52     plot(Xx(m, :, :), Yx(m, :, :), 'black', 'LineWidth', 2)
53     plot(Xy(m, :, :), Yy(m, :, :), 'black', 'LineWidth', 2);
54 end
55
56 t = 0:.001:2*pi;
57 plot(.762*sin(t)+0,.762*cos(t)+0, 'black', 'LineWidth', 2);
58 plot(.254*sin(t)+0,.254*cos(t)+0, 'black', 'LineWidth', 2);
59
60 axis equal
61 axis([-1.2 1.2 -1.2 1.2])
62 axis off
63 hold on
64
65
66
67
68 % For plotting non-transformed space
69
70 x = -.762*1.5:0.001:.762*1.5;
71 y = x;
72
73 Xx = zeros(18, length(x), 1);
74 Yx = zeros(18, length(y), 1);
75 Xy = Xx;
76 Yy = Yx;
77 xones = ones( length(x), 1 );
78 yones = ones( length(y), 1 );
79 xm = -.762*1.5+.0635;
80 ym = -.762*1.5+.0635;
81
82 for m=1:18
83     Xx(m, :, :) = xm*xones;
84     Yy(m, :, :) = ym*yones;
85     xm = xm + .127;
86     ym = ym + .127;
87 end
88
89 figure
90 hold on
91 for m=1:18
92     plot(Xx(m, :, :), y, 'black', 'LineWidth', 2)
93     plot(x, Yy(m, :, :), 'black', 'LineWidth', 2);
94 end
95
96 plot(.762*sin(t)+0,.762*cos(t)+0, 'black', 'LineWidth', 2);
97
98 axis equal
99 axis([-1.2 1.2 -1.2 1.2])
100 axis off
101 hold on

```


ACRONYMS AND ABBREVIATIONS

CeO₂ cerium oxide

DSRR double-sided split-ring resonator

FEM finite element method

HFSS Ansys HFSSTM

HTS high-temperature superconductor

J_C critical current density

LBCO lanthanum barium copper oxide

LN₂ liquid nitrogen

MgO magnesium oxide

MUT material under test

PCB printed circuit board

PEC perfect electric conductor

PNA programmable network analyzer

PPW parallel plate waveguide

R_S surface resistance

SRR split-ring resonator

SSLT Short-Short-Load-Thru

T_C critical temperature

TRL Thru-Reflect-Line

YBCO yttrium barium copper oxide

BIBLIOGRAPHY

- [1] S. A. Cummer, B.-I. Popa, D. Schurig, D. R. Smith, and J. Pendry, “Full-wave simulations of electromagnetic cloaking structures,” *Physical Review E*, vol. 74, p. 036621, Sep. 2006. [2](#), [5](#), [7](#), [11](#), [29](#)
- [2] J. B. Pendry, D. Schurig, and D. R. Smith, “Controlling electromagnetic fields,” *Science*, vol. 312, no. 5781, pp. 1780–1782, 2006. [2](#), [5](#)
- [3] B. Kanté, A. de Lustrac, J.-M. Lourtioz, and S. N. Burokur, “Infrared cloaking based on the electric response of split ring resonators,” *Opt. Express*, vol. 16, pp. 9191–9198, Jun 2008. [2](#), [5](#)
- [4] D. Schurig, J. J. Mock, B. J. Justice, S. A. Cummer, J. B. Pendry, A. F. Starr, and D. R. Smith, “Metamaterial electromagnetic cloak at microwave frequencies,” *Science*, vol. 314, pp. 977–980, 2006. [2](#), [5](#), [7](#), [11](#), [29](#), [44](#), [65](#), [70](#), [89](#)
- [5] B. Kanté, D. Germain, and A. de Lustrac, “Experimental demonstration of a nonmagnetic metamaterial cloak at microwave frequencies,” *Phys. Rev. B*, vol. 80, p. 201104, Nov 2009. [2](#), [44](#), [65](#), [89](#)
- [6] G. Breed, “Basic principles of electrically small antennas,” *High Frequency Electronics*, vol. 6, p. 50, February 2007. [4](#)
- [7] C. A. Balanis, *Antenna Theory: Analysis and Design*. John Wiley & Sons, 3 ed., 2005. [4](#)
- [8] W. G. Lyons, D. R. Arsenault, A. C. Anderson, T. G. Sollner, P. G. Murphy, M. M. Seaver, R. R. Boisvert, R. L. Slattery, , and R. W. Ralson, “High- t_c superconductive wideband compressive receivers,” *The Lincoln Laboratory Journal*, vol. 9, no. 1, p. 33, 1996. [4](#)
- [9] H. Chaloupka, N. Klein, M. Peiniger, H. Piel, A. Pischke, and G. Splitt, “Miniaturized high-temperature superconductor microstrip patch antenna,” *Microwave Theory and Techniques, IEEE Transactions on*, vol. 39, pp. 1513 –1521, sep 1991. [4](#)

- [10] G. B. Walker and C. R. Haden, "Superconducting antennas," *Journal of Applied Physics*, vol. 40, no. 5, pp. 2035–2039, 1969. 4
- [11] J. James, M. White, D. Steel, J. Carney, and M. Gledhill, "System considerations of a superconducting loop antenna," in *Electrically Small Antennas, IEE Colloquium on*, pp. 7/1–7/4, 1990. 4
- [12] J. G. Bednorz and K. A. Müller, "Possible high T_c superconductivity in the Ba-La-Cu-O system," *Zeitschrift für Physik B Condensed Matter*, vol. 64, pp. 189–193, 1986. 10.1007/BF01303701. 4
- [13] M. K. Wu, J. R. Ashburn, C. J. Torng, P. H. Hor, R. L. Meng, L. Gao, Z. J. Huang, Y. Q. Wang, and C. W. Chu, "Superconductivity at 93 K in a new mixed-phase Y-Ba-Cu-O compound system at ambient pressure," *Physical Review Letters*, vol. 58, pp. 908–910, Mar. 1987. 4
- [14] "Sunpower inc.." <http://www.sunpowerinc.com>. 4
- [15] A. J. Ward and J. B. Pendry, "Refraction and geometry in maxwell's equations," *Journal of Modern Optics*, vol. 43, no. 4, pp. 773–793, 1996. 5, 17, 118
- [16] D. Schurig, J. B. Pendry, and D. R. Smith, "Calculation of material properties and ray tracing in transformation media," *Opt. Express*, vol. 14, pp. 9794–9804, Oct 2006. 5, 17
- [17] P. Zhang, *Theory of transformation optics and invisibility cloak design*. PhD thesis, KTH Royal Institute of Technology, 2011. 5, 17, 99, 118
- [18] S. A. Ramakrishna and T. M. Grzegorzczuk, *Physics and Applications of Negative Refractive Index Materials*. CRC Press, 1st ed., 2008. 8
- [19] D. R. Smith, D. C. Vier, T. Koschny, and C. M. Soukoulis, "Electromagnetic parameter retrieval from inhomogeneous metamaterials," *Physical Review E*, vol. 71, p. 036617, Mar. 2005. 8, 11, 29, 43
- [20] J. B. Pendry, A. J. Holden, W. J. Stewart, and I. Youngs, "Extremely low frequency plasmons in metallic mesostructures," *Phys. Rev. Lett.*, vol. 76, pp. 4773–4776, Jun 1996. 8, 9, 10
- [21] T. Tsutaoka, T. Nakamura, and K. Hatakeyama, "Magnetic field effect on the complex permeability spectra in a $\text{Ni}_0.8\text{Zn}_{0.2}$ ferrite," *Journal of Applied Physics*, vol. 82, no. 6, 1997. 8
- [22] C. Sabah and H. G. Roskos, "Numerical and experimental investigation of fishnet-based metamaterial in a x-band waveguide," *Journal of Physics D: Applied Physics*, vol. 44, no. 25, p. 255101, 2011. 8, 9

- [23] E. Lheurette, G. Houzet, J. Carbonell, F. Zhang, O. Vanbesien, and D. Lippens, “Omega-type balanced composite negative refractive index materials,” *Antennas and Propagation, IEEE Transactions on*, vol. 56, no. 11, pp. 3462–3469, 2008. [8](#), [9](#)
- [24] H. Chen, L. Ran, J. Huangfu, X. Zhang, K. Chen, T. M. Grzegorzcyk, and J. Au Kong, “Left-handed materials composed of only s-shaped resonators,” *Phys. Rev. E*, vol. 70, p. 057605, Nov 2004. [8](#), [9](#)
- [25] J. Pendry, A. Holden, D. Robbins, and W. Stewart, “Magnetism from conductors and enhanced nonlinear phenomena,” *IEEE Trans. Micr. Theory Tech.*, vol. 47, pp. 2075–2084, 1999. [9](#), [10](#), [29](#)
- [26] U. Hasar and J. Barroso, “Permeability measurement of metamaterials with split-ring-resonators using free-space calibration-independent methods,” *J. Infrared, Millimeter, and Terahertz Waves*, vol. 33, no. 2, pp. 218–227, 2012. [8](#), [43](#)
- [27] X. Chen, T. M. Grzegorzcyk, B.-I. Wu, J. Pacheco, and J. A. Kong, “Robust method to retrieve the constitutive effective parameters of metamaterials,” *Physical Review E*, vol. 70, p. 016608, Jul. 2004. [8](#), [11](#), [29](#), [43](#)
- [28] D. R. Smith, S. Schultz, P. Markoš, and C. M. Soukoulis, “Determination of effective permittivity and permeability of metamaterials from reflection and transmission coefficients,” *Phys. Rev. B*, vol. 65, p. 195104, Apr 2002. [8](#), [43](#)
- [29] Z. Szabo, G.-H. Park, R. Hedge, and E.-P. Li, “A unique extraction of metamaterial parameters based on kramers-kronig relationship,” *IEEE Trans. Micr. Theory Tech.*, vol. 58, no. 10, pp. 2646–2653, 2010. [8](#), [43](#)
- [30] X. Chen, T. M. Grzegorzcyk, and J. A. Kong, “Optimization approach to the retrieval of the constitutive parameters of slab of general bianisotropic medium,” *Prog. in Electr. Res.*, vol. 60, pp. 1–18, 2006. [8](#), [43](#)
- [31] H. Chen, J. Zhang, Y. Bai, Y. Luo, L. Ran, Q. Jiang, and J. A. Kong, “Experimental retrieval of the effective parameters of metamaterials based on a waveguide method,” *Opt. Express*, vol. 14, pp. 12944–12949, Dec 2006. [8](#), [43](#), [45](#)
- [32] R. A. Shelby, D. R. Smith, and S. Schultz, “Experimental verification of a negative index of refraction,” *Science*, vol. 292, pp. 77–79, 2001. [11](#), [12](#), [29](#), [44](#)
- [33] L. Ran, J. Huangfu, H. Chen, X. Zhang, K. Cheng, T. M. Grzegorzcyk, and J. A. Kong, “Experimental study on several left-handed metamaterials,” *Progress in Electromagnetics Research*, vol. 51, pp. 249–279, 2005. [11](#), [29](#)

- [34] M. Gil, J. Bonache, and F. Martín, “Metamaterial filters: A review,” *Metamaterials*, vol. 2, no. 4, pp. 186–197, 2008. [11](#), [29](#)
- [35] S. Linden, C. Enkrich, M. Wegener, J. Zhou, T. Koschny, and C. M. Soukoulis, “Magnetic response of metamaterials at 100 terahertz,” *Science*, vol. 306, no. 5700, pp. 1351–1353, 2004. [11](#), [31](#), [40](#)
- [36] T. Koschny, M. Kafesaki, E. N. Economou, and C. M. Soukoulis, “Effective medium theory of left-handed materials,” *Physical Review Letters*, vol. 93, p. 107402, Sep. 2004. [11](#), [31](#), [40](#)
- [37] M. Ricci, N. Orloff, and S. M. Anlage, “Superconducting metamaterials,” *Applied Physics Letters*, vol. 87, no. 3, p. 034102, 2005. [11](#), [44](#)
- [38] M. C. Ricci and S. M. Anlage, “Single superconducting split-ring resonator electrodynamics,” *Applied Physics Letters*, vol. 88, no. 26, p. 264102, 2006. [11](#), [44](#)
- [39] M. Ricci, H. Xu, R. Prozorov, A. Zhuravel, A. Ustinov, and S. Anlage, “Tunability of superconducting metamaterials,” *IEEE Transactions on Applied Superconductivity*, vol. 17, pp. 918–921, Jun. 2007. [11](#), [44](#)
- [40] H.-T. Chen, H. Yang, R. Singh, J. F. O’Hara, A. K. Azad, S. A. Trugman, Q. X. Jia, and A. J. Taylor, “Tuning the resonance in high-temperature superconducting terahertz metamaterials,” *Physical Review Letters*, vol. 105, p. 247402, Dec. 2010. [11](#), [44](#)
- [41] F. Trang, H. Rogalla, and Z. Popović, “Resonant response of high temperature superconducting split-ring resonators,” in *2012 Applied Superconductivity Conference*. [13](#), [15](#), [99](#)
- [42] F. Trang, H. Rogalla, and Z. Popović, “Resonant response of high-temperature superconducting split-ring resonators,” *IEEE Trans. Appl. Superc.*, vol. 23, no. 3, pp. 1300405–1300405, 2013. [13](#), [15](#), [44](#), [99](#)
- [43] F. Trang, H. Rogalla, and Z. Popović, “Effective constitutive parameters of high-temperature superconducting split-ring resonator arrays.” Under review since 12/2013. [15](#)
- [44] F. Trang, E. F. Kuester, H. Rogalla, and Z. Popović, “Sensitivity of double-sided split-ring resonator arrays to fabrication tolerances,” *arXiv e-prints*, Jul. 2012. [15](#)
- [45] F. Trang, E. F. Kuester, H. Rogalla, and Z. Popović, “Fabrication sensitivity of double-sided split-ring resonator arrays,” in *2012 USNC-URSI*. [15](#)
- [46] J. L. Synge and A. Schild, *Tensor Calculus*. Dover Publications, Inc., 1978. [17](#), [120](#)

- [47] M. Dalarsson and N. Dalarsson, *Tensors, Relativity, and Cosmology*. Elsevier, Inc., 2005. 17, 120
- [48] J. Pendry, A. Holden, D. Robbins, and W. Stewart, “Magnetism from conductors and enhanced nonlinear phenomena,” *IEEE Transactions on Microwave Theory and Techniques*, vol. 47, pp. 2075–2084, 1999.
- [49] Rogers Corporation, “TMM thermoset microwave materials.” <http://www.rogerscorp.com>. 36
- [50] C. Saha and J. Y. Siddiqui, “A comparative analysis for split ring resonators of different geometrical shapes,” in *2011 IEEE Applied Electromagnetics Conference (AEMC)*, pp. 1–4, Dec. 2011. 37
- [51] T. K. Ishii, *Handbook of Microwave Technology*, vol. 1. Academic Press, 1995. 37
- [52] T. Van Duzer and C. W. Turner, *Principles of Superconductive Devices and Circuits*. Elsevier, 1981. 38
- [53] W. Henkels and C. Kircher, “Penetration depth measurements on type II superconducting films,” *IEEE Transactions on Magnetics*, vol. 13, pp. 63–66, Jan. 1977. 38
- [54] S. D. Brorson, R. Buhleier, J. O. White, I. E. Trofimov, H.-U. Habermeier, and J. Kuhl, “Kinetic inductance and penetration depth of thin superconducting films measured by THz-pulse spectroscopy,” *Physical Review B*, vol. 49, pp. 6185–6187, Mar. 1994. 38, 39
- [55] L.-B. Shi, Y.-F. Wang, Y.-Y. Ke, G.-H. Zhang, S. Luo, X.-Q. Zhang, C.-G. Li, H. Li, and Y.-S. He, “A study on the microwave responses of YBCO and TBCCO thin films by coplanar resonator technique,” *Chinese Physics*, pp. 3036–3041, Oct. 2007. 38, 39
- [56] G. Vardulakis, S. Withington, D. J. Goldie, and D. M. Glowacka, “Superconducting kinetic inductance detectors for astrophysics,” *Measurement Science and Technology*, vol. 19, no. 1, p. 015509, 2008. 39
- [57] W. Weir, “Automatic measurement of complex dielectric constant and permeability at microwave frequencies,” *Proceedings of the IEEE*, vol. 62, pp. 33–36, Jan. 1974. 40, 53, 65
- [58] D. R. Smith, P. Rye, D. C. Vier, A. F. Starr, J. J. Mock, and T. Perram, “Design and measurement of anisotropic metamaterials that exhibit negative refraction,” *IEICE Trans. Electronics*, vol. E87-C, pp. 359–370, Mar. 2004. 44
- [59] Theva, “Technical datasheet, film coating.” http://www.theva.com/user/eesy.de/theva.biz/dwn/Datasheet_Coatings.pdf. 44, 63

- [60] Rogers Corporation, “RO3000 series circuit materials.” <http://www.rogerscorp.com>. 50, 62
- [61] A. M. Nicolson and G. F. Ross, “Measurement of the intrinsic properties of materials by time-domain techniques,” *IEEE Trans. Instr. Meas.*, vol. 19, no. 4, pp. 377–382, 1970. 53, 65, 114
- [62] J. Mazierska, D. Ledenyov, M. V. Jacob, and J. Krupka, “Precise microwave characterization of MgO substrates for HTS circuits with superconducting post dielectric resonator,” *Superconductor Science and Technology*, vol. 18, no. 1, p. 18, 2005. 54
- [63] M. W. Hosking, B. A. Tonkin, Y. G. Proykova, A. Hewitt, N. M. Alford, and T. W. Button, “The dielectric constant of liquid nitrogen over the frequency range 0.5 to 10.4 GHz,” *Superc. Science Techn.*, vol. 6, no. 7, pp. 549–552, 1993. 56
- [64] D. R. Smith, J. Gollub, J. J. Mock, W. J. Padilla, and D. Schurig, “Calculation and measurement of bianisotropy in a split ring resonator metamaterial,” *J. Appl. Phys.*, vol. 100, no. 2, p. 024507, 2006. 59
- [65] Evonik Industries, “Rohacell dielectric properties.” <http://www.rohacell.com/product/rohacell/en/products-services/rohacell-ig-ig-f/pages/default.aspx>. 60
- [66] K. Kumley and E. F. Kuester, “Effect of scatterer size variations on the reflection and transmission properties of a metafilm,” in *2012 USNC-URSI*. 66
- [67] V. Fedotov, A. Tsiatmas, J. H. Shi, R. Buckingham, P. de Groot, Y. Chen, S. Wang, and N. Zheludev, “Temperature control of fano resonances and transmission in superconducting metamaterials,” *Opt. Express*, vol. 18, pp. 9015–9019, Apr 2010. 66
- [68] V. A. Fedotov, M. Rose, S. L. Prosvirnin, N. Papasimakis, and N. I. Zheludev, “Sharp trapped-mode resonances in planar metamaterials with a broken structural symmetry,” *Phys. Rev. Lett.*, vol. 99, p. 147401, Oct 2007. 66
- [69] Emerson and Cuming, “Eccosorb ls.” <http://www.eccosorb.com/Collateral/Documents/English-US/ElectricalParameters/lspareparameters.pdf>. 70
- [70] J. Wang, S. Qu, Z. Xu, J. Zhang, H. Ma, Y. Yang, and C. Gu, “Broadband planar left-handed metamaterials using split-ring resonator pairs,” *Photonics and Nanostructures - Fundamentals and Applications*, vol. 7, no. 2, pp. 108–113, 2009. 105
- [71] Rogers Corporation, “RO4000 series circuit materials.” <http://www.rogerscorp.com>. 105

- [72] H. B. Bhimnathwala, M. S. Wang, S. Bothra, K. W. Kristal, and J. M. Borrego, "A microwave system for high accuracy high spatial resolution dielectric constant uniformity measurement," in *20th European Microwave Conference*, vol. 1, pp. 495–500, Sept. 1990. 109
- [73] M. Wang, S. Bothra, J. Borrego, and K. Kristal, "High spatial resolution dielectric constant uniformity measurements using microstrip resonant probes," in *IEEE MTT-S Intern. Micr. Symp.*, vol. 3, pp. 1121–1124, May 1990. 109
- [74] N. Das, S. Voda, and D. Pozar, "Two methods for the measurement of substrate dielectric constant," *IEEE Trans. Micr. Theory Tech.*, vol. 35, pp. 636–642, 1987. 109
- [75] M. Moradian and M. Tayarani, "Spurious-response suppression in microstrip parallel-coupled bandpass filters by grooved substrates," *IEEE Trans. Micr. Theory Tech.*, vol. 56, pp. 1707–1713, 2008. 110
- [76] A. R. Djordjević, D. I. Olćan, and A. G. Zajić, "Modeling and design of milled microwave printed circuit boards," *Micr. Opt. Technol. Lett.*, vol. 53, pp. 264–270, 2011. 110
- [77] M. Gatchev, S. Kamenopolsky, V. Bojanov, and P. Dankov, "Influence of the milling depth on the microstrip parameters in milled PCB-plates for microwave applications," in *14th Intern. Conf. on Micr., Radar and Wireless Comm. (MIKON-2002)*, vol. 2, pp. 476–479, 2002. 110
- [78] O. Trescases, "Guide to designing and fabricating printed circuit boards," tech. rep., University of Toronto, ECE, Jan. 2006. 110
- [79] E. F. Kuester and D. C. Chang, *Theory of Waveguides and Transmission Lines*. Unpublished, 1st ed., 2011. 115
- [80] D. M. Pozar, *Microwave Engineering*. John Wiley & Sons, Inc, 2nd ed., 1998. 116